Light in strongly scattering semiconductors

diffuse transport and Anderson localization

Cover: Sponge on the rocks, by Jaime Gómez Rivas.
Printer's: PrintPartners Ipskamp, Enschede.
ISBN: 90-5776-082-7

Light in strongly scattering semiconductors

diffuse transport and Anderson localization

ACADEMISCH PROEFSCHRIFT

ter verkrijging van de graad van doctor
aan de Universiteit van Amsterdam,
op gezag van de Rector Magnificus
prof. mr. P.F. van der Heijden
ten overstaan van een door het college voor promoties
ingestelde commissie, in het openbaar te verdedigen
in de Aula der Universiteit
op dinsdag 16 april 2002, te 14:00 uur

door

Jaime Gómez Rivas

geboren te Madrid, Spanje

Promotiecommissie:

Promotor	Prof. Dr. A. Lagendijk
Co-promotor	Dr. R. Sprik
Overige leden	Prof. Dr. A.Z. Genack
	Dr. T. Gregorkiewicz
	Dr. T.W. Hijmans
	Prof. Dr. J.J. Kelly
	Prof. Dr. L.D. Noordam
	Prof. Dr. A. Polman

Faculteit der Natuurwetenschappen, Wiskunde en Informatica

The work described in this thesis has been partially supported by the European Commission through Grant No. ERBFM-BICT971921 of the TMR program.

It was carried out at the
Van der Waals-Zeeman Instituut, Valckenierstraat 65,
1018 XE Amsterdam, The Netherlands,
where a limited number of copies of this thesis is available.

A mis padres

Contents

1

Introduction

This thesis describes an experimental study of the propagation of light in disordered scattering media. In an intensive search for Anderson localization of light in 3D systems, strongly-scattering samples of high refractive index semiconductors have been studied. In this chapter a general introduction to light localization is given, starting from the basis of single and multiple scattering (sections 1.1 and 1.2). Weak localization and interference in random media are explained in section 1.3. In section 1.4 a simple picture of localization and the role of the dimensionality are given. A summary of the history of localization can be found in section 1.5. The reasons why it is difficult to localize light are discussed in section 1.6. A short summary of the chapters of this thesis is given in section 1.7.

1.1 Single scattering

The propagation of light in a homogeneous material is simple: light propagates in straight trajectories. Eventually, optical absorption may occur and the light intensity decays exponentially as the wave travels in the medium. If the wave encounters an inhomogeneity it is scattered, which means that its direction of propagation changes. An inhomogeneity or scatterer can be an atom with polarizability φ, or a particle of refractive index n, or a density fluctuation in a liquid or gas. The scattering cross section of the scatterer σ_s is defined as the amount of light removed from the incident beam by scattering.

Depending on the size of the scatterer r relative to the wavelength λ_o, the scattering can be classified in three different types: Rayleigh scattering, Mie scattering, and geometrical-optics scattering.

Rayleigh scattering is the scattering by particles much smaller than the optical wavelength, like for instance atoms and molecules. In this regime the scattering is

very inefficient and the cross section is given by [3]

$$\sigma_s = \frac{8}{3}\pi\varphi^2 k_o^4 , \tag{1.1}$$

where φ is the polarizability and the wave vector in vacuum is given by $k_o = 2\pi/\lambda_o$.

If the size of the scatterer is of the order of the wavelength σ_s is maximal. This regime is known as Mie scattering. The determination of the Mie cross section is far from trivial, and it can be calculated numerically with relative ease only for objects with a high degree of symmetry, as spheres or cylinders [4, 5]. In general, σ_s is larger when the refractive index contrast m between the scatterer and the surrounding medium is higher.

If the size of the scatterer is much larger than the wavelength its scattering cross section is equal to two times its geometrical cross section. This is the geometrical-optics regime, and the scattering is described by Snell's law [6].

The three scattering regimes are depicted in Fig. 1.1. In this figure the quality factor (or σ_s normalized by the geometrical cross section) is plotted as a function of the size parameter defined as $2\pi r/\lambda_o$. This example corresponds to a germanium sphere in air ($m = n/n_o = 4.1$). In the Mie scattering regime ($r \simeq \lambda_o$) the cross section presents a rich resonant structure, and it is up to 12 times larger than geometrical cross section. For $r \ll \lambda_o$, σ_s scales with λ_o^{-4}, and for $r \gg \lambda_o$, σ_s converges to $2\pi r^2$.

1.2 Multiple scattering

The scattering mean free path ℓ_s in a medium is defined as the average distance between two consecutive scattering events. If the medium is larger than ℓ_s the single-scattering approximation is not valid. Multiple scattering takes place. Depending on the arrangement of the scatterers, two limiting cases of multiple-scattering media can be discerned: crystals on one side and random or disordered media on the other. In this thesis a photonic material is defined as a medium that strongly scatters light.

A photonic crystal is a periodic structure of (usually two) different dielectric materials, with a lattice parameter of the order of the wavelength of light. Photonic crystals were first devised by E. Yablonovitch [7] and S. John in 1987 [8]. Light in such a structure is multiply scattered due to the periodic variation of the refractive index. This causes a splitting of the bands at the edges of the Brillouin zone called stop gaps. Light with energy equal to the energy of the stop gap can not propagate in the photonic crystal, and it is reflected according to Bragg's law [9]. A stop gap that exists for all directions is called a band gap. The feasibility to create a photonic

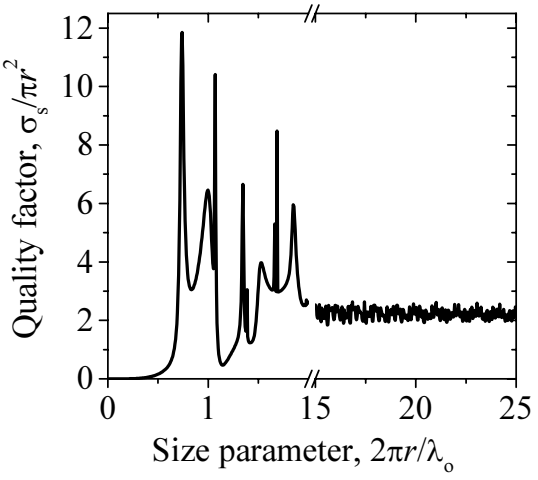

Figure 1.1:
Quality factor, defined as the scattering cross section σ_s normalized by the geometrical cross section πr^2, plotted versus the size parameter $2\pi r/\lambda_o$ of a germanium ($n = 4.1$) sphere in air $n_o = 1$. For $r \ll \lambda_o$ (Rayleigh scattering) the quality factor scales with λ_o^{-4}. If $r \simeq \lambda_o$ (Mie scattering) the scattering cross section is maximal at the resonances. If $r \gg \lambda_o$ (geometrical-optics scattering) the quality factor converges to 2.

crystal with a band gap has been demonstrated for microwave radiation [10]. A great experimental challenge is to make a crystal with a photonic band gap at optical wavelengths.

Three-dimensional photonic crystals can be formed by self-assembly of colloids.[1] Ordered colloids surrounded by air are called opals. If the air voids of an opal are filled with another material and the colloids are removed, by for instance calcination or etching, an inverse photonic crystal is formed [12, 13].

Apart from the multiple applications that photonic crystals have and are expected to have (superprisms [14], microcavities [15], waveguides [16], optical fibers [17], efficient light sources [18]), a photonic band gap will lead to exciting fundamental phenomena as the inhibition of spontaneous emission [7]. The realization of a photonic band gap material depends on the crystal structure, and on the refractive index contrast between the dielectric materials; for instance, for a face-cube-centered (fcc) inverse crystal a refractive index contrast larger than 2.8 is required [19].

A disordered medium has a random distribution of scatterers. Multiple scattering of light in random media is a phenomenon encountered daily: clouds, milk, sand, paper are some examples. The photonic or scattering strength in a disordered scattering medium is described by the inverse of the localization parameter

[1] Many other techniques to produce 3D photonic crystals have been developed. For a review see Ref. [11].

$k\ell_s$ (also known as the Ioffe-Regel parameter [20]),

$$k\ell_s = \frac{2\pi}{\lambda_o} n_e \ell_s \,, \tag{1.2}$$

where k is the wave vector in the medium, and n_e is the effective refractive index of the medium.

The scattering mean free path is, to a first approximation (independent-scattering approximation), given by

$$\ell_s = \frac{1}{\rho\sigma_s} \,, \tag{1.3}$$

where ρ is the density of scatterers and σ_s is the average scattering cross section. In a weakly-scattering medium $k\ell_s \gg 1$. The photonic strength can be increased by reducing ℓ_s, which is achieved by maximizing the scattering cross section.

In the weak-scattering limit, that is when the scatterers density is low, and/or when the scattering cross section is small, the transport of light is well described by the diffusion equation. The wave diffuses in the medium as electrons do in a disordered metal. The main approximation of the diffusion approach is to neglect any interference of the wave propagating along different paths. When the scattering becomes strong, interference plays an important role. If the scattering is strong enough light can be spatially localized, which means that it can not propagate. This occurs when $k\ell_s \simeq 1$, which is known as the Ioffe-Regel criterion of localization [20]. In sections 1.3 and 1.4 a simple picture of the role of interference and its connection to localization is given.

Similar to photonic crystals, direct and inverse random media can be realized. A direct medium or disordered opal consists of a powder of particles in air; while an inverse random media is a sponge like material in which air voids are surrounded by the material with high refractive index.

Figure 1.2 (a) shows a scanning-electron-microscope (SEM) photograph of an inverse photonic crystal of titanium dioxide TiO_2. The SEM photograph 1.2 (b) corresponds to an inverse random medium formed by electrochemical etching of gallium phosphide (GaP). The formation of porous GaP is described in chapter 5.

1.3 Weak localization

The concepts discussed in this and the next sections are general to any kind of wave. Therefore, they are applicable not only to light but also to quantum waves as electrons or to any classical wave as electromagnetic radiation or acoustic waves.

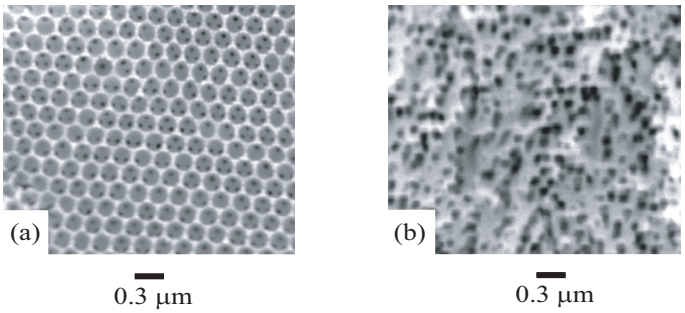

Figure 1.2: (a) SEM photograph of an inverse photonic crystal. The white regions correspond to TiO_2. The dark spots are the contact points between the colloids that formed the opal before the infiltration with TiO_2. These colloids were calcinated after the infiltration. Photo by courtesy of L. Bechger. (b) SEM photograph of an inverse random medium formed in GaP. The black regions are holes created by electrochemical etching.

The microscopic description of the wave propagation in a random medium requires the solution of the appropriate wave equation, such as the Schrödinger equation, the Maxwell's equations or the acoustic-wave equation. In order to obtain this solution the precise location of all the scatterers and their scattering properties need to be known. Of course, this is an impossible task.

By using the diffusion equation a great simplification is achieved in the macroscopic description of the wave propagation [22], i.e., on length scales larger than ℓ_s. The main approximation that the diffusion approach does is to neglect any interference effect.

The essence of the diffusion approximation can be captured by looking at the average intensity $\langle I_{AB} \rangle$ in a point B produced by a source located at A, as it is depicted in Fig. 1.3 (a). By average intensity is meant the ensemble average or the intensity averaged over all possible positions of the scatterers.

The wave can propagate along many different optical paths. For clarity, in Fig. 1.3 (a) only two of these paths are represented. It is important to realize that when a plane wave is incident on a scatterer, a spherical wave emerges from it. The lines representing the optical paths in Fig. 1.3 correspond to the wave vector of the scattered waves. The intensity at point B is calculated by multiplying the sum of the complex amplitudes E of the wave propagating along all possible optical paths by its complex conjugate

$$\langle I_{AB} \rangle = \langle \sum_i E_i \sum_j E_j^* \rangle = \langle \sum_i E_i E_i^* \rangle + \langle \sum_i \sum_{j \neq i} E_i E_j^* \rangle \simeq \langle \sum_i E_i E_i^* \rangle = \langle \sum_i I_i \rangle \, . \tag{1.4}$$

The term $\sum_i E_i E_i^*$ corresponds to amplitudes that propagate along the same path i. The term $\sum_i \sum_{j\neq i} E_i E_j^*$ accounts for the interference of the amplitudes propagating along different paths. This interference contribution depends on the difference in the length of paths i and j. For a path length difference of $n\lambda$, with $n = 0, 1, 2...$ and λ the wavelength in the medium, the two amplitudes interfere constructively; while if the path difference is $(2n+1)\lambda/2$ the interference is destructive.

In a real system there are many possible optical paths, and the interference term leads to the characteristic speckle pattern that can be observed on the transmitted or reflected light. Speckles are the bright and dark spots formed by the scattered light and they give to the transmission and reflection its granular aspect [23]. If the intensity I_{AB} is averaged over all possible realizations of the disorder, the interference term or speckle vanishes. This vanishing of the speckle occurs because on average the interference term cancels out since the contribution of constructive and destructive interference are equal. Neglecting the interference term in Eq. (1.4) the average intensity $\langle I_{AB} \rangle$ is the sum of the intensities of the waves diffusing along different paths. Therefore, the diffusion approximation does not make any distinction between diffusing particles or wave intensities. The wave diffuses in a 3D medium with a diffusion constant

$$D_B = \frac{1}{3} v_e \ell_B \,, \tag{1.5}$$

where v_e is the energy velocity or the rate at which the energy is transported [24, 25], and ℓ_B is the Boltzman mean free path or the length over which the direction of propagation of the wave is randomized by scattering *in the absence of interference*.

However, in a random medium there is always an interference contribution that survives (even for weakly-scattering media) the averaging over different configurations of the disorder. This interference originates from closed paths [26] as the one plotted in Fig. 1.3 (b). For each closed path a wave emitted at the source A can return to the same point after propagating along two reversed paths, I and II in Fig. 1.3 (b). These paths are called time-reversed paths. The returning probability or average intensity at the source after the wave has propagated in the random medium is

$$\langle I_{AA} \rangle = \langle \sum_i E_i E_i^* \rangle + \langle \sum_i \sum_{j\neq i'} E_i E_j^* \rangle + \langle \sum_{i=i'} E_i E_{i'}^* \rangle \simeq 2 \langle \sum_i E_i E_i^* \rangle = 2 \langle \sum_i I_i \rangle \,. \tag{1.6}$$

The first term is the same as in Eq. (1.4). The second term accounts for the interference of the amplitudes propagating along different paths, except for the time-reversed ones. Because of the same argument as before, the interference term is

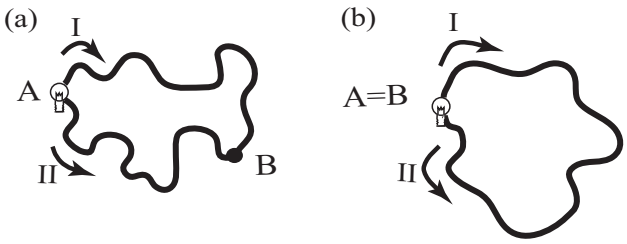

Figure 1.3:
(a) two possible paths (I and II) in a random medium between a source located at A and B. (b) a path (I) and its time reversed (II).

negligible. The $\sum_{i=i'} E_i E_{i'}^*$ term corresponds to the intensity due to waves propagating along the time-reversed paths i and i'. The difference between the lengths of time-reversed paths is zero, i.e., the interference is constructive, and the amplitudes are equal. All this makes that the intensity at the source is two times larger than expected on the basis of neglecting the interference. This effect is called weak localization, since it is believed to be the precursor of Anderson localization or strong localization (see section 1.4).

The main influence of weak localization on transport of the wave is the renormalization of the diffusion constant [28]. If the probability for the wave to return to the source is higher than the probability to diffuse away, the diffusion constant is reduced. The renormalization of the diffusion constant can be expressed as

$$D_{\mathrm{B}} > D = \frac{1}{3} \mathrm{v_e} \ell \,, \tag{1.7}$$

where ℓ is the transport mean free path or length over which the direction of propagation of the wave is randomized by scattering *in the presence of interference*. Weak localization is a stationary process, and the renormalization of the diffusion constant should be interpreted as a renormalization of the Boltzman mean free path.

1.4 Anderson localization

Localization was introduced by Philip W. Anderson in his famous article *absence of diffusion in certain random lattices* [29]. Anderson localization can be defined as $D = 0$ or equivalently $\ell = 0$. Following the discussion of the preceding section, localization occurs when the diffuse transport breaks down due to interference of waves propagating along time-reversed paths, i.e., when the wave returns to the source. When a wave is localized, its ensemble-average intensity decays exponentially with the distance to the source L and with a characteristic length given by the localization length ξ,

$$\langle I \rangle \propto \exp(-L/\xi) \,. \tag{1.8}$$

In this thesis only ensemble-average quantities are investigated. Therefore, the symbols $\langle\rangle$ will be omitted in the following.

Anderson localization is a phase transition between propagating states and localized states. As the important length scale for interference effects is the wavelength, A.F. Ioffe and A.R. Regel proposed that when the scattering mean free path is comparable to λ it should not be possible to describe classically the wave transport [20]. They established that the transition between the extended and localized states in a 3D infinite system formed by isotropic scatterers occurs when

$$k\ell_{\mathrm{s}} \simeq 1 \, . \tag{1.9}$$

Equation (1.9) is known as the Ioffe-Regel criterion for localization. The validity of the Ioffe-Regel criterion has been confirmed with more rigorous theories [30, 31].

At this point it is worthwhile to stress the difference between the scattering and the transport mean free paths. The scattering mean free path ℓ_{s} is the average distance between scattering events. The transport mean free path ℓ is the average distance necessary to randomize the direction of propagation of the wave by scattering. In the absence of interference the transport mean free path is called the Boltzman mean free path ℓ_{B}. If the scattering is anisotropic, one scattering event is not enough to randomize the direction of the propagation; in other words, one scattering event does not fully convert the ballistic propagation of the wave into diffuse propagation. The number of scattering events required for a full conversion in a non-absorbing medium is

$$\frac{\ell_{\mathrm{B}}}{\ell_{\mathrm{s}}} = \frac{1}{1-\langle\cos\vartheta\rangle} \, . \tag{1.10}$$

where $\langle\cos\vartheta\rangle$ is the average of the cosine of the scattering angle [32]. Thus $\ell_{\mathrm{s}} \leq \ell_{\mathrm{B}}$, and both mean free paths are equal only for isotropic scatterers, i.e., if $\langle\cos\vartheta\rangle = 0$.

Due to interference in strongly-scattering media, ℓ_{B} is renormalized to ℓ [28, 30]. In Fig. 1.4 the scattering and transport mean free paths of a system formed by isotropic scatterers are represented as a function of the disorder, which is defined as ℓ_{s}^{-1}. As can be appreciated, for a low degree of disorder $\ell_{\mathrm{s}} = \ell$. Close to the localization transition, indicated with an arrow in Fig. 1.4, ℓ becomes smaller than ℓ_{s}. If the Ioffe-Regel criterion is satisfied $\ell = 0$, and light is localized.

Often one can find in literature that the criterion for localization is $k\ell \simeq 1$. This is not correct since a non-zero ℓ means that transport is possible. The source of this confusion is probably due to the experimental difficulties to obtain ℓ_{s} in a strongly-scattering medium. As ℓ can be readily extracted from enhanced-backscattering

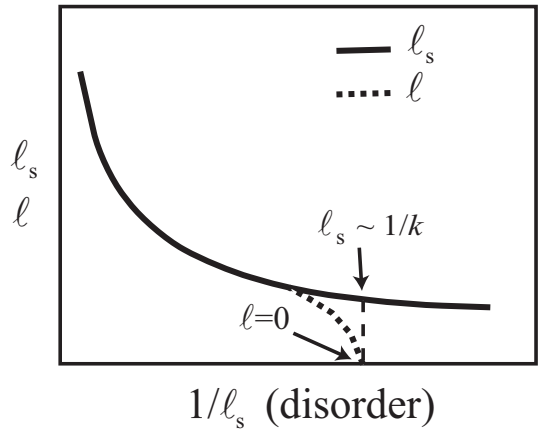

Figure 1.4: Scattering (ℓ_s) and transport (ℓ) mean free paths of light in a random medium plotted as a function of the disorder or the inverse of the scattering mean free path. The system is formed by isotropic scatterers. Close to the localization transition ($\ell_s \simeq 1/k$), ℓ becomes smaller than ℓ_s. At the transition $\ell = 0$.

measurements or from total-transmission measurements, $k\ell$ is incorrectly taken as the localization parameter.

The dimensionality plays a crucial role in localization. The following simple description of localization gives an idea of its main features and the role of the dimensionality. According to the diffusion equation, the energy density at place R and time t of a wave emitted from a point source in an infinite medium is [33]

$$U_{\rm d}(R,t) = \frac{1}{(4\pi Dt)^{d/2}} \exp\left[-R^2/(4Dt)\right] , \tag{1.11}$$

where $d = 1$, 2 or 3 is the dimensionality. The returning probability can be expressed as

$$\lim_{t\to\infty} \int_0^t U_{\rm d}(0,t) = \lim_{t\to\infty} \int_0^t \frac{{\rm d}t}{(4\pi Dt)^{d/2}} . \tag{1.12}$$

The lower integration limit of Eq. (1.12) should be replaced by the transport mean free time $\tau = \ell^2/D$. At $t < \tau$ it does not make sense to speak about diffusion since at this time scale the wave propagation is ballistic. If the returning probability is used to calculate interference contributions, the upper limit of integration of Eq. (1.12) should be replaced by the dephasing time $\tau_\rho = L_\rho^2/D$, where L_ρ is the dephasing length. Several dephasing mechanisms will be discussed later. Interference of waves propagating along time-reversed paths can not occur on time and lengths scales larger than τ_ρ and L_ρ. Integration of Eq. (1.12) gives

$$\int_\tau^{\tau_\rho} U_{\rm d}(0,t) = \begin{cases} \frac{1}{\pi^{1/2}D}(L_\rho - \ell) & ; d = 1 , \\ \frac{1}{2\pi D} \ln\left(\frac{L_\rho}{\ell}\right) & ; d = 2 , \\ \frac{1}{4\pi^{3/2}D}\left(\frac{1}{\ell} - \frac{1}{L_\rho}\right) & ; d = 3 . \end{cases} \tag{1.13}$$

If $L_\rho \to \infty$, the returning probability diverges in 1D and 2D systems, which means that the wave is always localized independently of the degree of disorder. Localization of classical waves has been observed in 1D and 2D systems [34–38].

For $d = 3$, the returning probability is finite. This probability is larger if ℓ is small, i.e., when the disorder is large. In 3D systems localization is only possible if the disorder is high enough.

There are several dephasing or phase-breaking mechanisms. For instance, the finite size of the sample will cut off long paths, preventing them to interfere. If the sample is smaller that the localization length ξ, the wave can propagate through the system. Theoretical [39] and experimental [38] studies in quasi-1D systems or waveguides, have shown the change in the wave transport as a function of the waveguide length.

An important phase-breaking mechanism in electronic systems is the electron-electron interaction, which complicates the study of the localization transition. The photon-photon interaction is negligible, making optical systems more suitable for this study.

A characteristic of classical waves is absorption. Since the number of electrons is conserved, absorption is absent in electronic systems. Absorption preserves the phase coherence of the wave. Therefore, it has been argued that absorption only introduces trivial effects and does not alter the essential behaviour of the transport [40, 41]. However, since absorption removes paths that are longer than the absorption mean free path ℓ_a (see section 2.1), preventing them to interfere, it is believed that it strongly affects the localization of classical waves and ultimately destroys it [42, 43].

It is certainly very interesting the study of the competition between localization and absorption, but special care has to be taken in absorbing systems since experiments can be misinterpreted. For instance, a transmission that decays exponentially with the sample thickness can be due to strong localization in a non-absorbing medium, or to classical diffusion in an absorbing medium, or to a combination of both effects.

The opposite effect to absorption is gain. Random lasers are disordered media with optical gain, and they were first described by Letokhov in 1968 [44]. After the work of Lawandy *et al.* in 1994 [45], random lasers have attracted great experimental and theoretical interest [46–53].

Recently, it has been claimed Anderson localization in random lasers from the observation of narrow peaks in the fluorescence spectra [54–60]. This claim has been questioned due to the weakness of the scattering in the studied samples [61]. Alternative explanations for these observations have been proposed [61, 62].

1.5 The history of localization

Localization was introduced in 1958 by Philip W. Anderson in the context of electronic propagation in disordered metals [29]. Anderson considered the solutions of the one-electron Schrödinger equation. For a perfect crystalline solid the electrons can move freely with a bandwidth B. However, Anderson contemplated the possibility of having potential wells with different heights $V = V_0 \pm \Delta V$ in a lattice; thus with ΔV as the disorder parameter. He showed that if $\Delta V/B$ is greater than a certain quantity all the states in the band become localized, and the electronic transport is inhibited.

As it has been mentioned in sections 1.2 and 1.4, A.F. Ioffe and A.R. Regel established in 1960 the criterion for the localization transition in infinite systems, i.e., $k\ell_s \simeq 1$ [20].

One of greatest advancements came in 1977 from the hand of D.J. Thouless [63], who showed that the onset of localization in a open system is determined by the sensitivity of the wave function to a change in the boundary conditions. This sensitivity is expressed by the dimensionless conductance g. The dimensionless conductance is defined as the ratio between the width of the energy levels and the level spacing. For $g < 1$ the typical level spacing is larger than the level width, and the coupling between eigenfunctions of adjacent systems is not possible. In this situation the transport is inhibited.

In 1979, E. Abrahams *et al.* developed the scaling theory of localization [64]. Based on perturbative calculations, they constructed a one-parameter scaling theory for the conductivity (or equivalently the diffusion constant). According to this theory, there is only a localization transition in 3D systems. In 1D and 2D systems all the states are localized.

One year later, D. Vollhardt and P. Wölfle went beyond the perturbation theory and, using diagrammatic techniques, they calculated the renormalized diffusion constant close to the transition [30].

It was at the beginning of the 80's when the connection between weak localization of electrons and the interference of quantum waves was made. B.L. Altshuler *et al.* used the argument of the electron-returning probability discussed in section 1.3 to study the effect of an external electrical field on weak localization [65]. The interpretation of weak localization in k-space in a 2D system of electrons was done by G. Bergmann [66], who referred to the time-reversed paths as *the echo of a scattered conduction electron*. Bergmann also studied the effect of several phase-breaking mechanisms, such as magnetic field, spin-orbit coupling and magnetic impurities. D.E. Khmel'nitskii used the simple picture of weak localization and localization in real space as it is explained in section 1.3 [26].

In the mid 80's, S. John [42] and P.W. Anderson [67] suggested that since localization is mainly a wave phenomenon, it should be possible to localize also classical waves.

In the search for Anderson localization of light many achievements in the understanding of the propagation of waves in random media have taken place. The greatest breakthrough was the observation of optical weak localization [68, 69].[2] This was the first experimental evidence of interference that survives ensemble average, and the similarities of the electronic propagation in disordered metals and light propagation in random media were demonstrated. Other important developments have been the prediction [71] and observation of long-range speckle correlations [72, 73] and universal conductance fluctuations [74], and the understanding of resonant scattering which leads to a reduced energy velocity [24, 25].

Difficulties in realizing a random medium where the scattering is efficient enough to induce localization has been the reason why only few works report 3D localization of electromagnetic waves. In 1989, J.M. Drake and A.Z. Genack [75] measured a very low diffusion constant in samples of TiO_2 scatterers. These pioneering experiments can be interpreted as the result of a low transport velocity due to resonant scattering, and, unfortunately, not to a renormalized transport mean free path [24].

In 1991, N. Garcia and A.Z. Genack reported microwave localization in a random mixture of aluminum and teflon spheres [43]. The relatively strong absorption in these samples is a complicating factor in the interpretation of the measurements. Localization of near infrared light in powders of GaAs was reported in 1997 by D.S. Wiersma *et al.* [76]. The interpretation of these measurements in terms of localization was questioned by the possibility of residual absorption introduced during the sample preparation [77]. Z.Q. Zhang *et al.* observed in 1998 localization of MHz electromagnetic radiation in a network of coaxial cables [78]. In 1999, F.J.P. Schuurmans *et al.* [79] interpreted the rounding of the enhanced-backscattered intensity versus the scattering angle, measured on porous GaP at visible wavelengths, in terms of the onset of Anderson localization. In these samples no optical absorption was detected [80].

A.A. Chabanov, M. Stoytchev and A.Z. Genack have shown recently that, even in the presence of absorption, the fluctuations of the transmitted flux reflect the extent of localization [38, 81]. As pointed out by these authors, fluctuations are of great importance in the study of localization. In this thesis only ensemble-average quantities are studied, thus fluctuations will not be treated.

[2] Weak localization was independently measured by Y. Kuga and A. Ishimaru in 1984 [70]. However, they did not explain their observations in terms of weak localization but as an anomalous retroreflectance.

1.6 How to localize light

To approach the localization transition $k\ell_s$ needs to be reduced. In contrast to electrons, to localize light it does not suffice to reduce the wave energy. For $\lambda \gg r$ the scattering is very inefficient (Rayleigh scattering), and $k\ell_s$ is large. Increasing k above a certain limit will also lead to inefficient scattering (geometrical-optics scattering). Therefore, light localization will be only possible in an energy window where σ_s is maximal, i.e., where ℓ_s is minimal. This window will correspond to wavelengths of the order of the scatterers size.

The scattering cross section σ_s is larger when the refractive index contrast m between the scatterers and the surrounding medium is high. Therefore, for localization experiments materials with high refractive index are necessary.

The relation $\ell_s = 1/\rho\sigma_s$ suggests that localization may be achieved more easily at the scattering resonances [82] (see Fig. 1.1). However, this relation is only valid in the limit of low density of scatterers, i.e., independent-scattering limit. In the situation of a high density of scatterers, dependent scattering gives rise to an increase of ℓ_s [83].

A simplified behaviour of ℓ_s on the ratio between the average scatterer radius r and the wavelength in the medium λ is plotted in Fig. 1.5. The minima of ℓ_s are achieved in the Mie scattering regime $r \simeq \lambda$. The dashed line in Fig. 1.5 represents the value of ℓ_s at which ℓ becomes zero due to interference. The transport mean free path is renormalized for values of ℓ_s in the vicinity of localization transition (dashed lines in Figs. 1.4 and 1.5). For a low refractive index contrast localization is not possible at any value of r/λ. If the refractive index contrast is high enough, there is a window (represented by the dotted line in Fig. 1.5) in which light is localized. The localization transition takes place at the so-called mobility edges. The mobility edges are marked with solid circles in Fig. 1.5.

A material in which light can be localized should be composed of scatterers of high refractive index material with a size of the order of the light wavelength in a matrix of low refractive index, i.e., a powder. An alternative to powders would be porous structures or samples formed by scatterers of low refractive index in a matrix of high refractive index material. The energy density coherent potential approximation (EDCPA) [84] predicts that it is easier to achieve light localization in porous structures than in powders [85, 86] (see appendix A).

The refractive index of some materials are plotted in Fig. 1.6 versus their energy band gap. The band gap is also displayed in terms of the wavelength λ_{gap}. As absorption must be avoided in the search for localization, λ_{gap} sets a lower limit for the wavelength. Even at sub-band gap wavelengths special care has to be taken since residual absorption introduced during the sample preparation can mislead the

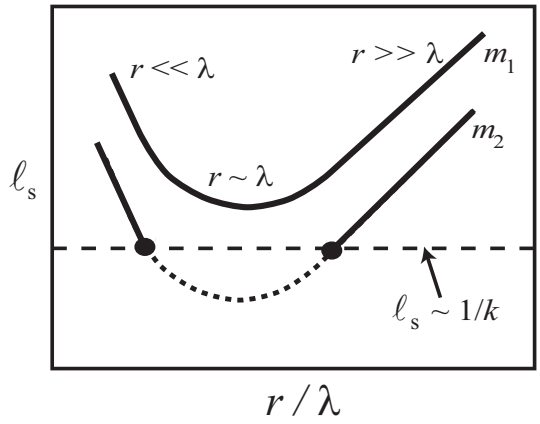

Figure 1.5: Scattering mean free path ℓ_s plotted as a function of the ratio between the average radius of the scatterers r and the wavelength (after S. John [42]). The dashed line represents the Anderson localization transition $k\ell_s \simeq 1$. Above the dashed line the transport of light is diffusive, below it light is localized. The two curved lines are ℓ_s in media with different refractive index contrast, $m_1 < m_2$, between the scatterers and the surrounding medium. A minimum in ℓ_s is achieved when the scatterers have a size of the order of the wavelength. The dotted part of the m_2 line stresses the window in which localization of light takes place.

interpretation of the optical experiments.

In the past, a lot of effort has been put into achieving localization with TiO_2 powders [24, 75]. The high refractive index of TiO_2, together with its absence of absorption in the visible, made it an attractive material for localization experiments. Although strongly-scattering samples without significant absorption can be easily made with TiO_2 powders, the lowest measured value of $k\ell_s$ is $\simeq 7$ [24], thus still far from the localization transition. Some semiconductors have higher refractive indexes than TiO_2 (see Fig. 1.6), and are good candidates to prepare a material where light can be localized.

1.7 This thesis

This thesis constitutes an experimental study of the propagation of light in disordered scattering media formed by high refractive index semiconductors. In an intensive search for Anderson localization of light in 3D systems, strongly-scattering samples of Si and Ge powders and porous GaP have been studied using several experimental techniques. Special attention has been paid to differentiate localization effects from optical absorption. This thesis is organized as follows:

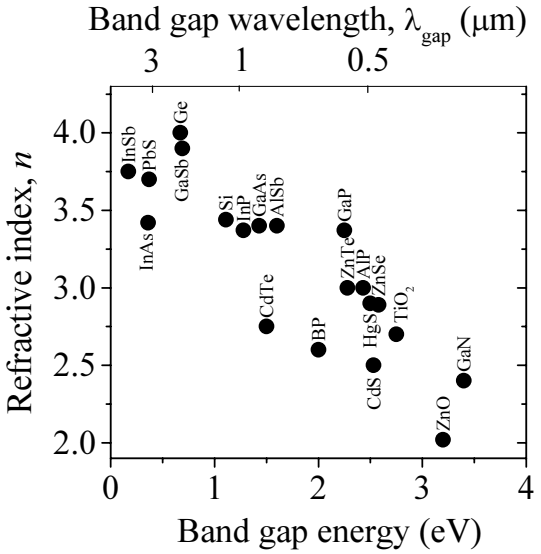

Figure 1.6:
Refractive index n, band gap energy, and the wavelength associated to this energy λ_{gap} of some materials. Figure reproduced from Ref. [87]

- Chapter 2: the theoretical framework of the propagation of light in random media is presented in this chapter. Coherent and diffuse propagation are discussed. Internal reflection at the sample interface determines the boundary conditions of the diffusion equation. The internal reflection is treated extensively. Stationary diffuse-transmission and reflection measurements allow the determination of the transport mean free path and the absorption length. From dynamic measurements the diffusion constant and absorption time can be obtained. Enhanced backscattering is discussed in detail. The effect of Anderson localization on the wave transport and its implications for the optical measurements are also explained.

- Chapter 3: total-transmission measurements through fine powders of Si and Ge particles in the near infrared are presented and discussed. At different wavelengths, the scattering properties and the effect of residual absorption are analyzed. The wavelength dependence of the transport mean free path in the Si samples is well described by the energy density coherent potential approximation EDCPA [84]. A method to study the effect of optical absorption consists in measuring the total transmission through the samples filled with a non-absorbing liquid. The Si and Ge samples are strongly-scattering media. However, the transmission measurements can be explained using diffusion theory, and significant absorption at sub-band gap wavelengths has been apparently introduced during the sample preparation.

- Chapter 4: this chapter contains the results of midinfrared experiments on

Ge powders done with a free electron laser (FELIX, Rijnhuizen, The Netherlands). From the transmission of the coherent beam the scattering mean free path is obtained in the wavelength range $5 - 8\ \mu$m. These are the first direct measurements of ℓ_s in strongly-scattering samples. The transport mean free path and the absorption coefficient are obtained from total-transmission and reflection measurements. The comparison of both mean free paths constitutes a new approach to the study of the localization transition. These measurements suggest a renormalization of ℓ due to the proximity of the localization transition. Also dynamic measurements were done with FELIX on the Ge samples. From these measurements the diffusion constant was obtained at $\lambda_o = 4.5$ and $8\ \mu$m. It is found that the diffusion constant is significantly reduced in samples thinner than $\simeq 7\ell$. Although there is not yet a theoretical explanation for this size dependence of the diffusion constant, these measurements confirm previous optical results on TiO_2 samples [88] and acoustic measurements [89]. With the diffusion constant and the transport mean free path, the energy velocity can be obtained. Due to resonant scattering [24, 25], the energy velocity in the Ge samples is 2 to 4 times lower than the phase velocity. Using the pulsed structure of the FELIX radiation, photoacoustic spectra of the Ge samples were obtained. Photoacoustic spectroscopy is a sensitive method to measure residual absorption in strongly-scattering samples.

- Chapter 5: the formation of porous GaP by electrochemical etching is discussed. Macroporous GaP is the strongest scattering material of visible light to date [79, 80], and no measurable optical absorption is introduced during the etching. The average size of the pores (scatterer radius) and inter-pore distance (scatterer density) depend on the doping concentration and on the etching potential. Therefore ℓ_s and the scattering strength can be easily tuned in a wide range. The scattering strength was investigated with enhanced-backscattering measurements. The strongest scattering samples have the biggest pores and are low-doped GaP etched at high potentials. The pore diameter can be further increased by chemical etching. With regard to the measurements presented in this thesis, porous GaP is the best candidate to localize light and to study the localization transition.

Most of the results presented in this thesis are contained in Refs. [90–97]

2

Propagation of light in disordered scattering media

The theoretical framework of the propagation of light in random media is reviewed in this chapter. Due to scattering, the amplitude of a wave that falls on a random system of scatterers decreases exponentially with the distance that the wave travels in the medium. The propagation of the incident wave, also known as the coherent beam, is discussed in section 2.1. As the intensity is removed from the coherent beam the diffuse intensity is built up. The diffusion equation is a good approximation for the description of the transport of the multiply-scattered light. This approximation will be discussed in section 2.2. Special attention must be paid to the boundary conditions, since light can be internally reflected at the sample interfaces. Stationary transmission and reflection, and dynamic transmission are also discussed in section 2.2. The enhanced backscattering (EBS) is described in section 2.3. The consequences that Anderson localization has for the wave transport are discussed in section 2.4.

2.1 Coherent beam

The coherent beam is defined as the average field amplitude. The propagation of a wave that falls on an inhomogeneous, disordered system of scatterers can be described by considering the system as homogeneous with an effective dielectric constant [98]. Due to scattering and absorption, the amplitude of the wave decreases exponentially with the distance that it propagates in the system. The extinction mean free path ℓ_{ex} is related to the imaginary part of the dielectric constant κ_e by

$$\ell_{ex} = \frac{1}{2\kappa_e} \,. \tag{2.1}$$

The coherent transmission through a sample of size L is defined as the fraction of the transmitted intensity

$$T_{\rm coh} \equiv \frac{I_{\rm coh}}{I_{\rm o}} = \exp(-L/\ell_{\rm ex}) \,, \tag{2.2}$$

where $I_{\rm o}$ is the incident intensity.

The extinction cross section $\sigma_{\rm ex}$ of a scatterer is defined as the amount of incident light removed by a scatterer due to scattering and absorption. The extinction cross section can be written as $\sigma_{\rm ex} = \sigma_{\rm s} + \sigma_{\rm a}$, where $\sigma_{\rm s}$ and $\sigma_{\rm a}$ are the scattering and absorption cross sections respectively. The relation between $\ell_{\rm ex}$ and $\sigma_{\rm ex}$ (in the independent-scattering approximation) is $\ell_{\rm ex} = 1/(\rho\sigma_{\rm ex})$, where ρ is the density of scatterers. Similarly, the scattering mean free path $\ell_{\rm s}$ and the absorption mean free path $\ell_{\rm a}$ can be related to their cross sections by $\ell_{\rm s} = 1/(\rho\sigma_{\rm s})$ and $\ell_{\rm a} = 1/(\rho\sigma_{\rm a})$.

The scattering mean free path is the average distance between two scattering events, or the distance over which the amplitude of the wave decays by a factor $1/e$ due to scattering. The absorption mean free path is the average distance over which the amplitude decays by the same factor due to absorption.

Another important quantity is the albedo a, defined as the ratio between the scattering and the extinction cross sections. An albedo equal to one means $\sigma_{\rm a} = 0$, thus no absorption. In the samples used for multiple-scattering experiments absorption must be low, which means that they are formed by scatterers with albedo close to one. Scatterers with an albedo $a = 0.99999$ can still give rise to an optical absorption strong enough to destroy localization [42], or at least to complicate the analysis of the measurements [43]. This represents a severe experimental difficulty in the search for localization.

With the definitions of $\ell_{\rm ex}$, $\ell_{\rm a}$, and $\ell_{\rm s}$ given above

$$T_{\rm coh} = \exp[-L(\ell_{\rm a} + \ell_{\rm s})/\ell_{\rm a}\ell_{\rm s}] \,. \tag{2.3}$$

In a weakly-absorbing medium, i.e., $\ell_{\rm s} \ll \ell_{\rm a}$, the decay of the coherent beam can be approximated to

$$T_{\rm coh} \simeq \exp(-L/\ell_{\rm s}) \,. \tag{2.4}$$

Equation (2.4) is known as the Lambert-Beer formula.

The coherent beam must not be identified with ballistic propagation. The coherent beam is formed by the wave scattered in the forward direction, while in the ballistic propagation no scattering is involved and the wave propagates with a speed equal to the speed of light in vacuum.

As the coherent beam is attenuated by scattering, the diffuse beam is built up. In the following section the propagation of the diffuse beam is described.

The name of coherent beam has led to call the diffuse beam as the incoherent beam. This nomenclature is confusing because the coherence of the wave is not destroyed by scattering. Multiple scattering randomizes the phase of the wave but preserves its coherence. This can be easily observed in the speckle pattern of the transmitted light through a random sample when it is illuminated by a coherent source. Speckle is the result of the interference of many partial waves with different phases randomized by scattering.

2.2 Diffusive propagation

2.2.1 The radiative-transfer equation and the diffusion approximation

The propagation of light in a multiple-scattering medium is far from trivial. The exact solution requires to solve the Maxwell's equations, for which the position, shape and size of all the scatterers needs to be known. This is obviously an impossible task. Ab-initio numerical calculations are limited to one and quasi-one[1] dimensional systems and to a small number of scatterers [99].

By obviating the phase of the wave, or in other words, by leaving behind the wave nature, the specific intensity[2] can be described by the radiative-transfer equation (RTE), equivalent to the Boltzman equation for classical particles. Neglecting the phase of the wave seems to be a severe simplification; however, the RTE has proven its validity. Of course, the RTE can not deal with speckle, since this phenomenon is due to wave interference. Therefore the applicability of the RTE is limited to ensemble-averaged quantities or quantities averaged over the different configurations of the disorder. The RTE has been mainly exploited by astrophysicists in the study of the propagation of radiation in stellar atmospheres and in interstellar clouds [100]. Unfortunately, the RTE cannot be solved analytically in most cases. Although with the advent of computers powerful numerical methods have been developed [101], it is always useful to have analytical solutions.

The next approximation to the RTE is the diffusion approximation, for which analytical solutions are easily found. The diffusion approximation, besides neglecting interference, considers an almost isotropic distribution of the direction of propagation of the diffuse intensity. This approximation is thus valid only when the gradient of the energy density is low.

A clear derivation of the diffusion equation from the RTE can be found in

[1] A quasi-1D system has a transverse size comparable to one mean free path.

[2] The specific intensity $I_{\widehat{\mathbf{k}}}(\mathbf{r},t)$ at position $\mathbf{r}$ and time t is defined as the average power flux density within an unit-frequency band centered at a frequency ν, and within an unit-solid angle in the direction given by the unit vector $\widehat{\mathbf{k}}$.

Ref. [22]. According to the diffusion approximation, the energy density U_d in a sample illuminated by a plane wave is

$$\frac{\partial U_d}{\partial t} - D_B \frac{\partial^2 U_d}{\partial z^2} = I_o \delta(z - z_p) - \frac{1}{\tau_a} U_d \,, \tag{2.5}$$

where D_B is the Boltzman diffusion constant, I_o is the incident flux and τ_a^{-1} is the absorption rate. In Eq. (2.5), the incoming energy flux at the boundary $z = 0$ is replaced by a source of diffuse radiation of strength I_o located at $z = z_p$ [102]. The Boltzman diffusion constant D_B is given in a 3D system by $D_B = v_e \ell_B / 3$, with v_e the energy velocity or the rate at which energy is transported, and ℓ_B the Boltzman mean free path. The Boltzman mean free path, or transport mean free path in the absence of interference, is the average distance necessary to randomize the direction of propagation of the wave by scattering. One scattering event may not be enough to randomize the direction of propagation. the scattering and Boltzman mean free paths are related by [22]

$$\ell_B = \frac{\ell_s}{1 - a\langle \cos\vartheta \rangle} \,, \tag{2.6}$$

where a is the albedo and $\langle \cos\vartheta \rangle$ is the average of the cosine of the scattering angle. Only for isotropic scatterers both mean free paths are equal, i.e., $\langle \cos\vartheta \rangle = 0$, and in general $\ell_B \geq \ell_s$.

Optical absorption is included in the last term of Eq. (2.5), where the absorption time is given by $\tau_a = L_a^2 / D_B$. The absorption length L_a is the average distance between the starting and ending points of random-walk paths of length ℓ_a. It can be easily proven that in a 3D system

$$L_a = \sqrt{\frac{\ell_B \ell_a}{3}} = \sqrt{\frac{\ell_B}{3\alpha}} \,. \tag{2.7}$$

where $\alpha = \ell_a^{-1}$ is the absorption coefficient.

The diffusion approximation has been conscientiously tested and it has proven its validity for the description of the transport of light [91, 103–106] as well as for sound [107, 108]. This approximation applies to weakly-absorbing systems, i.e., ℓ_s, $\ell_B \ll \ell_a$ [109], with a low gradient of the energy density [22, 110]. In the extreme case of Anderson localization the transport is inhibited and the diffusion approximation breaks down.

2.2.2 Boundary conditions: internal reflection

To solve the diffusion equation it is necessary to know the boundary conditions (BCs). Lagendijk *et al.* [111] proposed that, since there is a refractive index contrast at the interface, the BCs must include internal reflection. Zhu *et al.* [112]

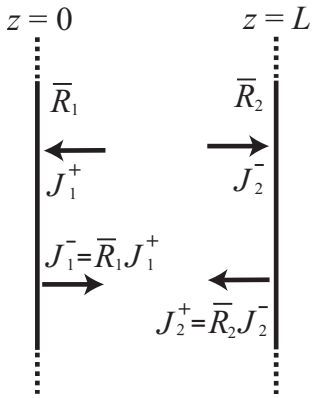

Figure 2.1: Random medium with boundaries at $z = 0$ and L. The average reflectivities at the interfaces are $\overline{R_1}$ and $\overline{R_2}$ respectively. The diffuse fluxes outwards the medium are J_1^+ at $z = 0$ and J_2^- at $z = L$. The fluxes inwards, J_1^- and J_2^+, are due to the reflectivity at the interfaces.

identified these BCs in the case of index-matched media with the BCs of the RTE solution for a semi-infinite layer of isotropic scatterers.

Most of the experiments in 3D media, and all the ones presented in this thesis, are done in samples with the geometry of a slab, i.e., samples with lateral dimensions x and y, much larger that its transverse dimension z. The boundary conditions of the diffusion equation are determined by considering that the diffuse fluxes going into the sample at $z = 0$ and $z = L$ are due to a finite reflectivity at the interfaces. This situation is depicted in Fig. 2.1, where the sample interfaces, with an average reflectivity $\overline{R_1}$ and $\overline{R_2}$, are represented. The fluxes outwards are denoted as J_1^+ at $z = 0$ and J_2^- at $z = L$, while the fluxes inwards are J_1^- and J_2^+ respectively. The BCs are

$$J_1^- = \overline{R_1} J_1^+ \ \text{ at } \ z = 0\,, \tag{2.8}$$

$$J_2^+ = \overline{R_2} J_2^- \ \text{ at } \ z = L\,. \tag{2.9}$$

To evaluate the fluxes let's consider a medium composed by isotropic and non-absorbing or weakly-absorbing scatterers, i.e., $\ell_B \ll \ell_a$. Using spherical coordinates, as represented in Fig. 2.2, the flux scattered directly from the volume dV onto the surface dS is given by

$$\mathrm{d}J^+ = U_d(r,\theta,\varphi)\mathrm{d}V\,\frac{v_e}{\ell_B}\frac{\cos\theta}{4\pi r^2}\exp(-r/\ell_B)\mathrm{d}S\,, \tag{2.10}$$

where the energy density in dV is denoted by $U_d(r,\theta,\varphi)\mathrm{d}V$ and ℓ_B/v_e is the Boltzman mean free time. The fractional solid angle sustained by dS from dV is $\mathrm{d}\Omega = (\cos\theta/r^2)\mathrm{d}S$, and the fraction of the energy density in dV that flows in the direction of dS is $\mathrm{d}\Omega/4\pi$. The loss due to scattering between dV and dS is taken into account in Eq. (2.10) by the factor $\exp(-r/\ell_B)$.

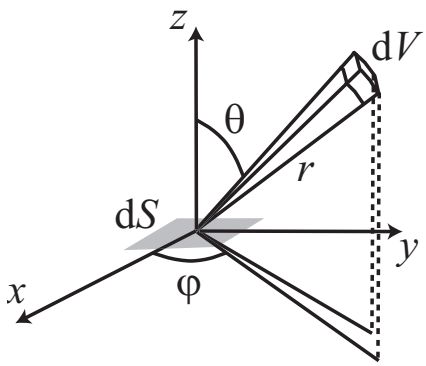

Figure 2.2:
Differential scattering volume $\mathrm{d}V$ in a random medium. The plane $z = 0$ is the interface of the medium.

Replacing $\mathrm{d}V$ by $r^2 \sin\theta \mathrm{d}r\,\mathrm{d}\theta\,\mathrm{d}\varphi$, the total flux, which is given by integration of Eq. (2.10) over the half space $z > 0$, is

$$J^+ \mathrm{d}S = \frac{\mathrm{d}S}{4\pi}\frac{\mathrm{v_e}}{\ell_\mathrm{B}} \int_0^{\pi/2} \mathrm{d}\theta \int_0^{2\pi} \mathrm{d}\varphi \int_0^{\infty} \mathrm{d}r\, U_\mathrm{d}(r,\theta,\varphi) \cos\theta \sin\theta\, \mathrm{e}^{-r/\ell_\mathrm{B}} \,. \tag{2.11}$$

This integral can be evaluated by expanding $U_\mathrm{d}(r,\theta,\varphi)$ around the origin. The diffusion approximation is only valid when the gradient of the energy density is low [22, 110], thus the expansion can be restricted to the first order

$$U_\mathrm{d}(r,\theta,\varphi) \simeq (U_\mathrm{d})_0 + \left(\frac{\partial U_\mathrm{d}}{\partial x}\right)_0 x + \left(\frac{\partial U_\mathrm{d}}{\partial y}\right)_0 y + \left(\frac{\partial U_\mathrm{d}}{\partial z}\right)_0 z \,. \tag{2.12}$$

To simplify the notation the subscript 0 will be omitted.

The terms containing x and y do not contribute to the total flux since the integration over $\mathrm{d}\varphi$ runs from 0 to 2π. Taking z in spherical coordinates $z = r\cos\theta$, Eqs. (2.11) and (2.12) give

$$J^+ = \frac{U_\mathrm{d}\mathrm{v_e}}{4} + \frac{D_\mathrm{B}}{2}\frac{\partial U_\mathrm{d}}{\partial z} \,. \tag{2.13}$$

The flux J^- is obtained by performing the integration (2.11) over the half space $z < 0$

$$J^- = \frac{U_\mathrm{d}\mathrm{v_e}}{4} - \frac{D_\mathrm{B}}{2}\frac{\partial U_\mathrm{d}}{\partial z} \,. \tag{2.14}$$

Substituting Eqs. (2.13) and (2.14) into Eqs. (2.8) and (2.9), the following BCs are found

$$U_\mathrm{d} - z_{\mathrm{e}_1}\frac{\partial U_\mathrm{d}}{\partial z} = 0 \quad \text{at } z = 0 \,, \tag{2.15}$$

$$U_{\mathrm{d}} + z_{\mathrm{e}_2} \frac{\partial U_{\mathrm{d}}}{\partial z} = 0 \quad \text{at } z = L\,, \tag{2.16}$$

where z_{e_1} and z_{e_2} are given by [112]

$$z_{\mathrm{e}_{1,2}} = \frac{2}{3}\ell_{\mathrm{B}} \frac{1+\overline{R_{1,2}}}{1-\overline{R_{1,2}}}\,. \tag{2.17}$$

Equations (2.15) and (2.16) are equivalent to extrapolate U_{d} to 0 at a distance $z_{\mathrm{e}_{1,2}}$ outside the sample surface. This is the reason why $z_{\mathrm{e}_{1,2}}$ are called the extrapolation lengths. Therefore, in the limit of weakly-absorbing samples, the solution of the diffusion equation with the mixed BCs (2.15) and (2.16) is similar to the solution with zero energy density at the extrapolation lengths

$$U_{\mathrm{d}} = 0 \quad \text{at} \begin{cases} z = -z_{\mathrm{e}_1}, \\ z = L + z_{\mathrm{e}_2}. \end{cases} \tag{2.18}$$

If $\overline{R_1} = 0$ or $\overline{R_2} = 0$, the corresponding extrapolation length is $2\ell_{\mathrm{B}}/3$, thus very close to the value of $0.7104\ell_{\mathrm{B}}$ obtained from the RTE for a semi-infinite slab of isotropic scatterers, also known as the Milne equation [113].

The average reflectivity at the boundary is calculated from the Fresnel's reflection coefficients. It is therefore assumed a flat interface that separates the random system, which has an effective refractive index n_{e}, from the outside world with a refractive index n_{o}. Obviously the surface of the sample is not flat since the scatterers give to the interface a roughness, which in our case is of the order of the optical wavelength. Nonetheless, in average, a boundary reflectivity can be defined from the Fresnel's reflection coefficients [114].

At the interface $z = 0$ the diffuse flux J_1^- entering the sample can be written as

$$J_1^- = \int_0^{\pi/2} \mathrm{d}\theta\, J_1^+(\theta) R(\theta)\,. \tag{2.19}$$

Since scattering randomizes the polarization of the wave [115], $R(\theta)$ is the average Fresnel's reflection coefficient

$$R(\theta) = \frac{R_{\parallel}(\theta) + R_{\perp}(\theta)}{2}\,, \tag{2.20}$$

where $R_{\parallel}(\theta)$ and $R_{\perp}(\theta)$ are the Fresnel's reflection coefficients for incident light polarized parallel and perpendicular to the plane of incidence. Using Eqs. (2.10) and (2.12), Eq. (2.19) can be written as

$$J_1^- = \frac{U_{\mathrm{d}} \mathrm{v}_{\mathrm{e}}}{2} R_{\mathrm{I}} + \frac{\mathrm{v}_{\mathrm{e}} \ell_{\mathrm{B}}}{2} \frac{\partial U_{\mathrm{d}}}{\partial z} R_{\mathrm{II}}\,, \tag{2.21}$$

with

$$R_{\mathrm{I}} = \int_0^{\pi/2} \mathrm{d}\theta\, R(\theta) \cos\theta \sin\theta \,, \tag{2.22}$$

and

$$R_{\mathrm{II}} = \int_0^{\pi/2} \mathrm{d}\theta\, R(\theta) \cos^2\theta \sin\theta \,. \tag{2.23}$$

Since Eqs. (2.21) and (2.14) are equal at $z = 0$, it can be found that

$$U_{\mathrm{d}} - \frac{2}{3}\ell_{\mathrm{B}} \frac{1 + 3R_{\mathrm{II}}}{1 - 2R_{\mathrm{I}}} \frac{\partial U_{\mathrm{d}}}{\partial z} = 0 \,. \tag{2.24}$$

Comparing Eqs. (2.24) and (2.15) the average reflectivity is

$$\overline{R_1} = \frac{3R_{\mathrm{II}} + 2R_{\mathrm{I}}}{3R_{\mathrm{II}} - 2R_{\mathrm{I}} + 2} \,. \tag{2.25}$$

A similar expression to Eq. (2.25) is obtained for $\overline{R_2}$, with the only substitution of $R(\theta)$ in R_{I} and R_{II} by the appropriated Fresnel's reflection coefficient at this interface.

2.2.3 Angular-resolved transmission

Usually z_{e_1} and z_{e_2} are calculated using Eq. (2.17), and assuming a value of the effective refractive index of the sample n_{e}, based, for instance, on the volume fraction of the scatterers. Unfortunately, effective-medium theories, like Maxwell-Garnet or Bruggeman [116], from which it is possible to obtain n_{e} knowing the volume fraction of scatterers, are only valid in the weak-scattering limit. Extensions of these theories into the strong-scattering regime, like the energy density coherent potential approximation EDCPA [84, 117], are only applicable to systems formed by scatterers with known scattering properties.

An enticing alternative to the theoretical estimation of n_{e}, is its experimental determination. This determination can be done from the measurement of the angular-resolved transmission [94, 97, 114].

It has been demonstrated in section 2.2.2 that, in a weakly-absorbing medium, the energy density extrapolates to zero at a distance z_{e_2} from the interface of the sample. The energy density close to the interface opposite to the one on which the sample is illuminated can be thus written as

$$U_{\mathrm{d}}(r, \theta, \varphi) \propto r\cos\theta + z_{\mathrm{e}_2} \,. \tag{2.26}$$

Introducing Eq. (2.26) into Eq. (2.10), and integrating over dr and dφ leads to

$$J(\theta) \propto (r\cos\theta + z_{e_2})\cos\theta\,\sin\theta\,\mathrm{d}\theta\,. \tag{2.27}$$

The transmitted flux is given by Eq. (2.27) multiplied by the Fresnel's transmission coefficient $[1-R(\theta)]$. Refraction at the sample interface needs also to be considered. If the angle formed by the normal to the sample surface and the direction of observation is denoted by θ_e, the relation between θ_e and θ is given by Snell's law. Defining $\mu_e = \cos\theta_e$ and $\mu = \cos\theta$, the escape function $P(\mu_e)$ or the angular distribution of the transmitted light is [114]

$$\frac{P(\mu_e)}{\mu_e} = \frac{3}{2}\left(\frac{n_e}{n_o}\right)^2 (z_{e_2}+\mu)\,[1-R(\mu)]\,. \tag{2.28}$$

The factor $(3n_e^2/2n_o^2)$ arises from the normalization of the angular-transmitted flux. The reflection coefficient and z_{e_2} depend solely on the refractive index contrast at the interface n_e/n_o. Since in an experiment the refractive index outside the sample is known, the only free parameter to fit an experimentally determined $P(\mu_e)$ is n_e.

2.2.4 Total transmission and reflection

The solution of the stationary diffusion equation

$$D_B\frac{\partial^2 U_d}{\partial z^2} = -I_o\delta(z-z_p) + \frac{1}{\tau_a}U_d\,, \tag{2.29}$$

with the boundary conditions (2.15) and (2.16), is [118]

$$U_d(z) = Q^{-1}\frac{I_o L_a}{D_B}\begin{cases} \left[\sinh\left(\frac{z}{L_a}\right) + \frac{z_{e_1}}{L_a}\cosh\left(\frac{z}{L_a}\right)\right]\times \\ \times\left[\sinh\left(\frac{L-z_p}{L_a}\right) + \frac{z_{e_2}}{L_a}\cosh\left(\frac{L-z_p}{L_a}\right)\right] & \text{for } z < z_p\,, \\ \left[\sinh\left(\frac{z_p}{L_a}\right) + \frac{z_{e_1}}{L_a}\cosh\left(\frac{z_p}{L_a}\right)\right]\times \\ \times\left[\sinh\left(\frac{L-z}{L_a}\right) + \frac{z_{e_2}}{L_a}\cosh\left(\frac{L-z}{L_a}\right)\right] & \text{for } z > z_p\,, \end{cases} \tag{2.30}$$

where

$$Q = \left(1+\frac{z_{e_1}z_{e_2}}{L_a^2}\right)\sinh\left(\frac{L}{L_a}\right) + \left(\frac{z_{e_1}+z_{e_2}}{L_a}\right)\cosh\left(\frac{L}{L_a}\right)\,. \tag{2.31}$$

In an experiment the measured quantity is the flux. The diffuse total transmission $T_{\rm d}(z_{\rm p})$, due to a source of diffuse radiation located at $z_{\rm p}$, through a sample of thickness L is defined as the transmitted flux normalized by the incident flux. This total transmission is given by

$$T_{\rm d}(z_{\rm p}) = \frac{-D_{\rm B}}{I_{\rm o}} \left(\frac{\partial U_{\rm d}}{\partial z} \right)_{\rm z=L} = Q^{-1} \left[\sinh\left(\frac{z_{\rm p}}{L_{\rm a}} \right) + \left(\frac{z_{\rm e_1}}{L_{\rm a}} \right) \cosh\left(\frac{z_{\rm p}}{L_{\rm a}} \right) \right] . \quad (2.32)$$

Similarly the total reflection is

$$R_{\rm d}(z_{\rm p}) = \frac{-D_{\rm B}}{I_{\rm o}} \left(\frac{\partial U_{\rm d}}{\partial z} \right)_{\rm z=0} = Q^{-1} \left[\sinh\left(\frac{L - z_{\rm p}}{L_{\rm a}} \right) + \left(\frac{z_{\rm e_2}}{L_{\rm a}} \right) \cosh\left(\frac{L - z_{\rm p}}{L_{\rm a}} \right) \right] . \quad (2.33)$$

In the limit of no absorption, i.e., $L_{\rm a} \to \infty$, Eq. (2.32) simplifies to

$$T_{\rm d}(z_{\rm p}) = \frac{z_{\rm p} + z_{\rm e_1}}{L + z_{\rm e_1} + z_{\rm e_2}} , \quad (2.34)$$

The diffuse total transmission scales with the inverse of the sample thickness. This is equivalent to the familiar Ohm's law for the conductance in electronic systems.

If the coherent transmission is negligible and $L_{\rm a} \to \infty$, Eq. (2.33) can be written as

$$R_{\rm d}(z_{\rm p}) = 1 - T_{\rm d}(z_{\rm p}) . \quad (2.35)$$

Since no absorption takes place, the diffuse total transmission plus the diffuse total reflection equals 1.

If $L_{\rm a} \ll L$, the diffuse total transmission decays exponentially with the sample thickness

$$T_{\rm d}(z_{\rm p}) = A(z_{\rm p}) \exp(-L/L_{\rm a}) , \quad (2.36)$$

with

$$A(z_{\rm p}) = \frac{2L_{\rm a}(z_{\rm p} + z_{\rm e_1})}{L_{\rm a}^2 + (z_{\rm e_1} + z_{\rm e_2})L_{\rm a} + z_{\rm e_1} z_{\rm e_2}} . \quad (2.37)$$

The diffuse total reflection in the limit $L_{\rm a} \ll L$ is given by

$$R_{\rm d}(z_{\rm p}) = \frac{L_{\rm a}(L_{\rm a} + z_{\rm e_2})}{L_{\rm a}^2 + (z_{\rm e_1} + z_{\rm e_2})L_{\rm a} + z_{\rm e_1} z_{\rm e_2}} \exp(-z_{\rm p}/L_{\rm a}) . \quad (2.38)$$

Energy conservation requires that

$$T_{\rm d}(z_{\rm p}) + R_{\rm d}(z_{\rm p}) + T_{\rm coh} + \Re = 1 \ , \tag{2.39}$$

where $\Re$ is the fraction of absorbed energy, and $T_{\rm coh}$ is the coherent transmission (see section 2.1) .

Since the direction of propagation of the wave is randomized after an average distance of one Boltzman mean free path $\ell_{\rm B}$, the source of diffusion radiation is usually considered to be located at $z = z_{\rm p} \sim \ell_{\rm B}$ [102]. For systems formed by (nearly) isotropic scatterers the approximation $z_{\rm p} \sim \ell_{\rm B}$ can be relaxed by weighting Eqs. (2.32) and (2.33) with an exponential-source distribution [119]

$$\begin{aligned} T_{\rm d} &= \textstyle\int_0^{L/\ell_{\rm B}} T_d(z_{\rm p}) e^{-z_{\rm p}} {\rm d}z_{\rm p} = \\ &= (2Q)^{-1} \left\{ \tfrac{L_{\rm a}}{\ell_{\rm B}-L_{\rm a}} \left[\exp\left(\tfrac{L}{L_{\rm a}} - \tfrac{L}{\ell_{\rm B}} \right) - 1 \right] \left[1 + \tfrac{z_{\rm e_1}}{L_{\rm a}} \right] + \right. \\ &\quad \left. + \tfrac{L_{\rm a}}{\ell_{\rm B}+L_{\rm a}} \left[\exp\left(-\tfrac{L}{L_{\rm a}} - \tfrac{L}{\ell_{\rm B}} \right) - 1 \right] \left[1 - \tfrac{z_{\rm e_1}}{L_{\rm a}} \right] \right\} \ , \end{aligned} \tag{2.40}$$

$$\begin{aligned} R_{\rm d} &= \textstyle\int_0^{L/\ell_{\rm B}} R_d(z_{\rm p}) e^{-z_{\rm p}} {\rm d}z_{\rm p} = \\ &= -(2Q)^{-1} \left\{ \tfrac{L_{\rm a} \exp\left(\frac{L}{L_{\rm a}}\right)}{\ell_{\rm B}+L_{\rm a}} \left[\exp\left(-\tfrac{L}{L_{\rm a}} - \tfrac{L}{\ell_{\rm B}} \right) - 1 \right] \left[1 + \tfrac{z_{\rm e_2}}{L_{\rm a}} \right] + \right. \\ &\quad \left. + \tfrac{L_{\rm a} \exp\left(-\frac{L}{L_{\rm a}}\right)}{\ell_{\rm B}-L_{\rm a}} \left[\exp\left(\tfrac{L}{L_{\rm a}} - \tfrac{L}{\ell_{\rm B}} \right) - 1 \right] \left[1 - \tfrac{z_{\rm e_2}}{L_{\rm a}} \right] \right\} \ . \end{aligned} \tag{2.41}$$

Equations (2.40) and (2.41) represent the diffuse total transmission and reflection of a disordered slab of isotropic scatterers that is illuminated by a plane wave.

The Boltzman mean free path is defined in the absence of interference. As we will see in sections 2.3 and 2.4, enhanced backscattering and the extreme case of Anderson localization renormalize $\ell_{\rm B}$ to the transport mean free path ℓ by interference. If the size of the sample is larger than the coherence length (see section 2.4), the results derived from the diffusion approach are still valid with the substitution of $\ell_{\rm B}$ by ℓ.

In Fig. 2.3 the diffuse total transmission (a) and reflection (b) of three media are plotted versus the optical thickness $L/\ell_{\rm B}$. In the three examples $z_{\rm e_1} = z_{\rm e_2} = (2/3)\ell_{\rm B}$. The solid lines correspond to a non-absorbing medium. For $L/\ell_{\rm B} \gg 1$ the diffuse total transmission decreases linearly with the inverse of the sample thickness, and $T_{\rm d} + R_{\rm d} = 1$. A medium with an absorption length of $L_{\rm a} = 25\ell_{\rm B}$

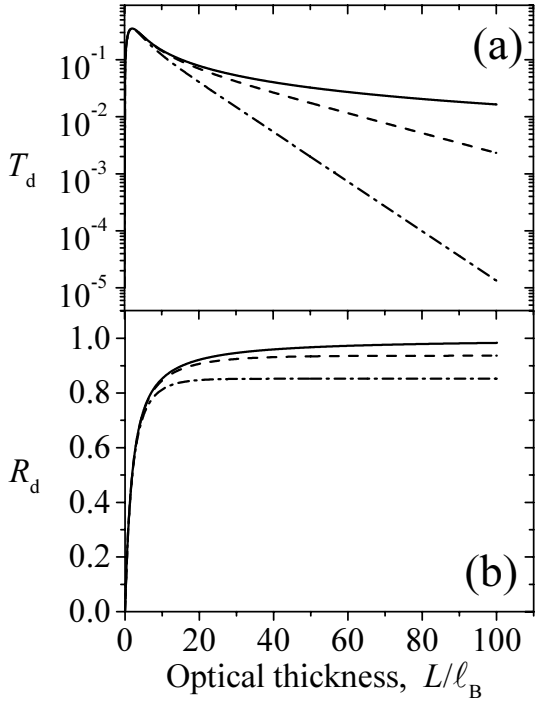

Figure 2.3:
Diffuse total transmission T_d and reflection R_d as a function of the optical thickness L/ℓ_B. The solid lines correspond to a random system in the absence of absorption. The dashed lines display T_d and R_d for a system with $L_a = 25\ell_B$. An absorption length of $L_a = 10\ell_B$ is considered in the T_d and R_d represented by dashed-dotted lines. In the three examples the extrapolation lengths are $z_{e_1} = z_{e_2} = (2/3)\ell_B$.

is represented in Fig. 2.3 with dashed lines. The dashed-dotted lines display the diffuse total transmission and reflection of a system with $L_a = 10\ell_B$. For $L \gg L_a$ the diffuse total transmission decreases exponentially with the sample thickness, Eq. (2.36), and the diffuse total reflection saturates to a value that depends on L_a, Eq. (2.38).

In a total-transmission measurement, the diffuse and coherent transmission are measured. Therefore, the total transmission is defined as

$$T = T_{coh} + T_d \, . \tag{2.42}$$

The coherent transmission is only significant in samples with a thickness of a few mean free paths.

The total reflection is formed by the specular and diffuse reflection. In the experiments presented in this thesis, the wave incidences normally to the sample interface. The specular reflection is minimum and the total reflection can be approximated to the diffuse reflection

$$R \simeq R_d \, . \tag{2.43}$$

Equations (2.42) and (2.43) are the basis for the analysis of the total-transmission and reflection measurements presented on chapters 3 and 4.

2.2.5 Dynamic transmission

The time-dependent diffusion equation (2.5) with the BCs (2.15) and (2.16) does not have a closed-form solution [107]. An analytical expression for the time-dependent energy density is obtained if the BCs (2.18) are used. As discussed in section 2.2.2, both BCs are equivalent if $\ell_a \gg \ell_B$. The time-dependent energy density in a sample illuminated by a plane wave is

$$\begin{aligned} U_d(z,z_p,t) = \; & \frac{\exp(-t/\tau_a)}{L+z_{e_1}+z_{e_2}} \sum_{n=1}^{\infty} \left\{ \exp\left(\frac{-\pi^2 n^2 D_B t}{(L+z_{e_1}+z_{e_2})^2} \right) \times \right. \\ & \left. \times \left[\sin\left(\pi n \frac{z+z_{e_1}}{L+z_{e_1}+z_{e_2}} \right) \sin\left(\pi n \frac{z_p+z_{e_2}}{L+z_{e_1}+z_{e_2}} \right) \right] \right\} . \end{aligned} \tag{2.44}$$

The time-dependent diffuse transmission is [120, 121]

$$\begin{aligned} T_d(t) = \; & -\frac{\pi D \exp(-t/\tau_a)}{(L+z_{e_1}+z_{e_2})^2} \sum_{n=1}^{\infty} \left\{ n \exp\left(\frac{-\pi^2 n^2 D_B t}{(L+z_{e_1}+z_{e_2})^2} \right) \times \right. \\ & \left. \times \left[\cos\left(\pi n \frac{L-\ell_B+z_{e_1}}{L+z_{e_1}+z_{e_2}} \right) \sin\left(\pi n \frac{\ell_B+z_{e_2}}{L+z_{e_1}+z_{e_2}} \right) \right] \right\} . \end{aligned} \tag{2.45}$$

where z_p has been replaced by ℓ_B.

Multiple scattering increases the transit time of the light through the sample. Light propagating through short optical paths leaves the sample at earlier times than light that propagates along long paths. The distribution of path lengths (Eq. (2.44)) results in a broadening of the transmitted pulse. In Fig. 2.4 it is displayed the normalized transmission through a non-absorbing sample with an optical thickness $L/\ell_B = 50$, a diffusion constant $D_B = 50$ m/s^2, and extrapolation

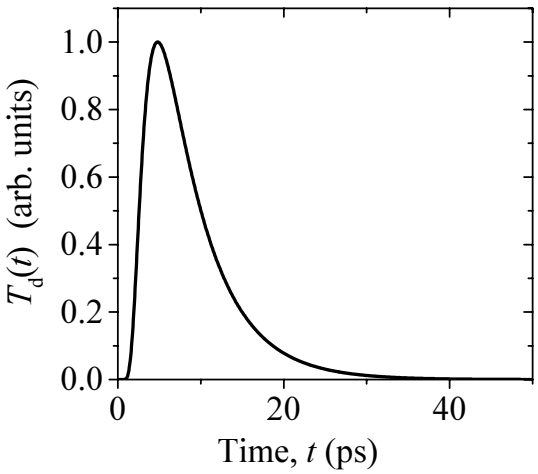

Figure 2.4: Normalized transmission of a pulse $\delta(t)$ through a non-absorbing sample with an optical thickness $L/\ell_B = 50$, diffusion constant $D_B = 50$ m/s^2, and extrapolation lengths $z_{e_1} = z_{e_2} = (2/3)\ell_B$.

lengths $z_{e_1} = z_{e_2} = (2/3)\ell_B$. The incoming pulse in the example of Fig. 2.4 is a delta function at $t = 0$.

The long-time behaviour of the pulse is given by an exponential decay [121]

$$T_d(t) \propto \exp\left(-\frac{t}{\Gamma}\right) , \tag{2.46}$$

where the decay time Γ is

$$\frac{1}{\Gamma} = \frac{\pi^2 D_B}{(L + z_{e_1} + z_{e_2})^2} + \frac{1}{\tau_a} . \tag{2.47}$$

2.3 Enhanced backscattering

Enhanced backscattering (EBS) refers to an increase of the reflected intensity from a disordered medium relative to the diffuse reflection. This increase is due to interference of waves propagating along time-reversed paths. The observation of EBS [68, 69] constituted a breakthrough in the study of wave propagation in disordered media. EBS demonstrates the survival of interference effects in the ensemble-averaged intensity and the limitations of the radiative-transfer equation. The principle of EBS has been introduced in section 1.3, these ideas are developed here.

Consider a plane wave emitted by a source located at A (see Fig. 2.5). This wave falls on a semi-infinite random medium with a wave vector $\mathbf{k}_A$. The wave propagates along optical paths as the one represented with a solid line in Fig. 2.5. The wave is scattered out of the medium. In the direction of point B the wave vector is $\mathbf{k}_B$. For each path there is a time reversed (dashed line in Fig. 2.5). The interference pattern produced at B by the wave propagating along the two paths is determined by the difference in the path length. The relative phase of the wave at B is given by [122]

$$\frac{E_B^I}{E_B^{II}} = \exp\left[i\left(\mathbf{k}_A + \mathbf{k}_B\right) \cdot \left(\mathbf{r}_1 - \mathbf{r}_n\right)\right] , \tag{2.48}$$

where E_B^I and E_B^{II} are the amplitudes of the wave after propagating along the path I and its time reversed II respectively, $\mathbf{r}_1$ is the location of the first scatterer of the optical path and $\mathbf{r}_n$ is the position of the last scatterer. Since at the exact backscattering direction both paths are equal, the phases of the wave are the same. At directions other than the backscattering the phase $\mathbf{k}_A \cdot (\mathbf{r}_1 - \mathbf{r}_n)$ is due to the extra path length at incidence, while the phase $\mathbf{k}_B \cdot (\mathbf{r}_1 - \mathbf{r}_n)$ owns to the extra path length at exit.

The intensity at B is calculated by squaring the sum of the complex amplitude of the wave E^{I} propagating along the path and the amplitude of the wave E^{II} propagating along the time-reversed path

$$| E_{\mathrm{B}}^{\mathrm{I}} + E_{\mathrm{B}}^{\mathrm{II}} |^2 = | E_{\mathrm{B}}^{\mathrm{I}} |^2 + | E_{\mathrm{B}}^{\mathrm{II}} |^2 + E_{\mathrm{B}}^{\mathrm{I}} E_{\mathrm{B}}^{\mathrm{II}^*} + E_{\mathrm{B}}^{\mathrm{I}^*} E_{\mathrm{B}}^{\mathrm{II}} \, . \tag{2.49}$$

Under the assumption that the system is invariant under time reversal, i.e, in both paths the wave sees the same scatterers, equations (2.48) and (2.49) give

$$\begin{aligned} | E_{\mathrm{B}}^{\mathrm{I}} + E_{\mathrm{B}}^{\mathrm{II}} |^2 &= | E_{\mathrm{B}}^{\mathrm{I}} |^2 | \, 1 + \exp\left[-i\left(\mathbf{k}_{\mathrm{A}} + \mathbf{k}_{\mathrm{B}}\right) \cdot \left(\mathbf{r}_1 - \mathbf{r}_n\right)\right] |^2 = \\ &= 2 \, | E_{\mathrm{B}}^{\mathrm{I}} |^2 \left\{1 + \cos\left[\left(\mathbf{k}_{\mathrm{A}} + \mathbf{k}_{\mathrm{B}}\right) \cdot \left(\mathbf{r}_1 - \mathbf{r}_n\right)\right]\right\} \, . \end{aligned} \tag{2.50}$$

The term $\cos\left[\left(\mathbf{k}_{\mathrm{A}} + \mathbf{k}_{\mathrm{B}}\right) \cdot \left(\mathbf{r}_1 - \mathbf{r}_n\right)\right]$ is due to the interference terms $E_{\mathrm{B}}^{\mathrm{I}} E_{\mathrm{B}}^{\mathrm{II}^*} + E_{\mathrm{B}}^{\mathrm{I}^*} E_{\mathrm{B}}^{\mathrm{II}}$. Since the first and the last scatterer of the optical path are approximately at the same distance from the sample interface, i.e., at one mean free path, the interference term can be estimated as $\cos\left[\,|\, \mathbf{k}_{\mathrm{A}} + \mathbf{k}_{\mathrm{B}} \,||\, \mathbf{r}_1 - \mathbf{r}_n \,|\, \cos\theta\right]$, where θ is the scattering angle formed by $\mathbf{k}_{\mathrm{A}}$ and $-\mathbf{k}_{\mathrm{B}}$. The interference term oscillates between +1 and -1 as θ is varied. The larger the distance between the first and the last scatterer is, the faster is this oscillation as θ changes. In Fig. 2.6 (a) the interference pattern is plotted for three optical paths with different $|\, \mathbf{r}_1 - \mathbf{r}_n \,|$. Note that this interference pattern is equal to the one produced by two coherent sources located at $\mathbf{r}_1$ and $\mathbf{r}_n$.

At the exact backscattering direction, $\mathbf{k}_{\mathrm{A}} = -\mathbf{k}_{\mathrm{B}}$, there is no difference in the path length of the reversed paths independently of their length or, in other words, the interference term is maximum for all optical paths (see Fig. 2.6 (a)). If all the paths are added, there is consequently an enhanced intensity at the backscattering

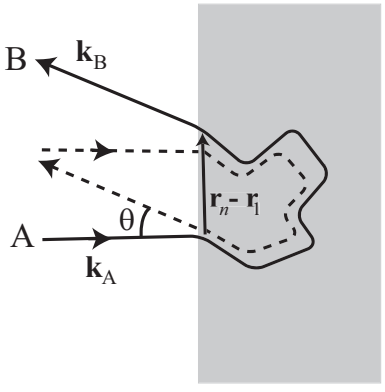

Figure 2.5:
Disordered scattering medium represented by the shadowed region. A source located at point A generates a plane wave with wave vector $\mathbf{k}_{\mathrm{A}}$ which incidences in the medium. The reflection is observed at point B. The scattering angle is θ. A possible optical path is represented with a solid line, while its time reversed is displayed with a dashed line.

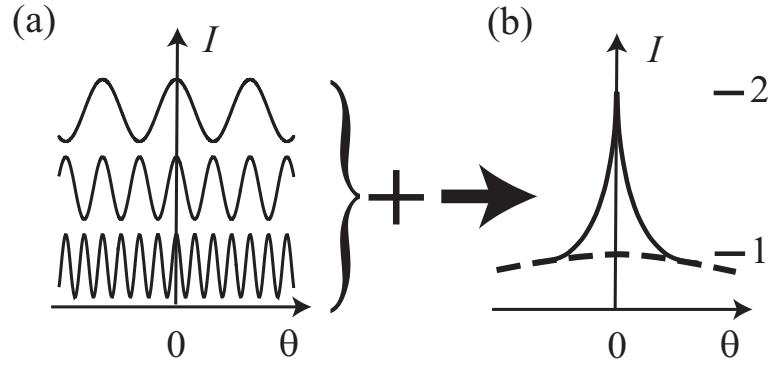

Figure 2.6: (a) Three interference patterns of waves propagating along time-reversed paths of a random system. The uppermost corresponds to a path in which the distance between the first and last scatterer is small. The lowest is of a path in which this distance is large. (b) enhanced-backscattered intensity resulting from the addition of all possible interference patterns. The dashed line represents the diffuse background. Ideally the enhancement factor equals two times the diffuse reflection at $\theta = 0$.

direction. As θ is increased the enhanced intensity decreases until it merges with the diffuse reflection background. As represented in Fig. 2.6 (b), a cone-shaped intensity, called enhanced-backscattering cone is obtained when the intensity is plotted as a function of the scattering angle. The dashed line in Fig. 2.6 (b) represents the diffuse background.

Enhanced backscattering influences the wave transport. The enhanced intensity at the backscattering direction can be interpreted as a higher probability for the wave to return to the source, which can be translated into a lower probability that the wave has to diffuse away. Enhanced backscattering leads to a renormalization of the Boltzman diffusion constant due to interference of the wave's amplitudes propagating along time-reversed paths. The renormalized diffusion constant is $D = v_e \ell/3$, where the transport mean free path ℓ is defined as the average length over which the direction of propagation of the wave is randomized by scattering *in the presence of interference*.

The shape of the EBS cone can be calculated using the diffusion approximation. The backscattered intensity is determined by the distribution of paths between $\mathbf{r}_1$ and $\mathbf{r}_n$, weighted by the interference term,

$$\frac{I(\mathbf{k}_A + \mathbf{k}_B)}{I_o} = \int d\mathbf{r}_{\parallel} P(\mathbf{r}_1, \mathbf{r}_n) \{1 + \cos[(\mathbf{k}_A + \mathbf{k}_B) \cdot (\mathbf{r}_1 - \mathbf{r}_n)]\} \ . \qquad (2.51)$$

Where $P(\mathbf{r}_1, \mathbf{r}_n)$ represents the probability that a wave entering the medium at $\mathbf{r}_1$ diffuses to $\mathbf{r}_n$, where it exits. Since the first and last scatterer are located approx-

imately at the same distance from the boundary, $\mathbf{r}_{\parallel} \approx \mathbf{r}_1 - \mathbf{r}_n$, where $\parallel$ stands for parallel with the surface of the sample. For a semi-infinite and non-absorbing sample, and in the absence of any phase-breaking mechanism [102]

$$\frac{I(\mathbf{k}_A + \mathbf{k}_B)}{I_o} = \frac{3(\ell + z_{e_1})}{4\pi\ell} \left\{ 1 + \frac{1 - \exp[-2 \mid \mathbf{k}_A + \mathbf{k}_B \mid (\ell + z_{e_1})]}{2 \mid \mathbf{k}_A + \mathbf{k}_B \mid (\ell + z_{e_1})} \right\} . \quad (2.52)$$

The factor $2 \mid \mathbf{k}_A + \mathbf{k}_B \mid (\ell + z_{e_1})$ varies from 0 at the backscattering direction to values $\gg 1$ at large scattering angles. Therefore, Eq. (2.52) predicts a sharp shape at the backscattering direction with an enhancement factor of 2 with respect to the diffuse background.

The full width at half maximum W of the EBS cone is related to the transport mean free path by [102, 123]

$$\ell \simeq \frac{\lambda_o}{2\pi} \frac{0.7}{W} (1 - \overline{R}_1) . \quad (2.53)$$

If ℓ is short there is a small probability for the wave to diffuse over a long distance before it is scattered out of the sample. In this situation the cone is wide. The effect of internal reflection in the cone width is easy to understand: due to internal reflection light is re-injected into the sample, leading to an average increase of $\mathbf{r}_{\parallel}$, and a narrowing of the EBS cone [124].

Following diffusion arguments, the EBS intensity at the scattering angle θ is due to paths with a length s [122]

$$s \leq \frac{\lambda_o^2}{4\theta^2 \ell} . \quad (2.54)$$

For large θ, or at the wings of the cone, only short paths contribute to the EBS. At the backscattering direction, i.e., $\theta = 0$, infinitely-long paths add to the cone.

Due to optical absorption and the finite thickness of the sample, long paths do not contribute to the EBS [125, 126]. In a sample of thickness L, if the wave reaches the side opposite to the one where it incidences, it will escape. Using random-walk arguments, the number of steps needed to travel a distance L is $3(L/\ell)^2$. The path length is given by the number of random steps multiplied by ℓ (step length) $s = 3L^2/\ell$. Using Eq. (2.54), for $\theta \lesssim \lambda_o/(2\sqrt{3}L)$ the number of paths contributing to the EBS is limited by L, and the shape of the EBS intensity becomes flat. The same reasoning holds if there is optical absorption, in which case paths longer than ℓ_a are absent. The net distance traveled by the random walker along the path of length ℓ_a is the absorption length L_a (Eq. 2.7). In this case, the flattening of the EBS intensity occurs for $\theta \lesssim \lambda_o/(2\sqrt{3}L_a)$.

The determination of the EBS shape for finite and absorbing samples is performed by including both effects in $P(\mathbf{r}_1, \mathbf{r}_n)$. This calculation can be found in Refs. [123, 127].

It should be stressed that the enhanced backscattering is the result of the interference of waves propagating along time-reversed paths. There is also interference of waves that propagate along independent paths. As it is explained in section 1.3, this interference leads to optical speckle. To observe the EBS intensity it is necessary to average over speckle, which is achieved by averaging the measurements over different configurations of the scatterers. This averaging is readily done in suspensions of scatterers by Brownian motion. In solid samples the averaging is usually realized by performing several measurements at different locations of the sample [128].

2.4 Anderson localization

Enhanced backscattering leads to a renormalization of the Boltzman diffusion constant or, equivalently, of the Boltzman mean free path. Although EBS occurs in any disordered system, the correction to the diffusion constant can be ignored in most of them due to the fairly-weak scattering. Only when the scattering mean free path approaches the critical value where the localization transition takes place, interference of waves propagating along closed paths plays a crucial role in the wave transport. The coherent behavior of the sample on length scales shorter than a characteristic length denoted by the coherence length ζ need to be considered in the determination of the transport mean free path ℓ. As mentioned in the preceding section, the transport mean free path is defined as the average distance required to randomize the direction of propagation in the presence of interference. The critical mean free path ℓ_c is defined as the value of the scattering mean free path at which the Anderson localization transition takes place. According to the Ioffe-Regel criterion for localization [20], for isotropic scattering the transition occurs when $\ell_c \sim k^{-1} = \lambda_o/(2\pi n_e)$. If ℓ_s is equal to ℓ_c the transport is inhibited and ℓ vanishes. The renormalization of ℓ_B due to interference can be expressed as [28, 64]

$$\ell = \ell_B - \ell_c \equiv \ell_B^2/\zeta \,. \tag{2.55}$$

The coherence length is thus defined as

$$\zeta = \frac{\ell_B^2}{\ell_B - \ell_c} \,. \tag{2.56}$$

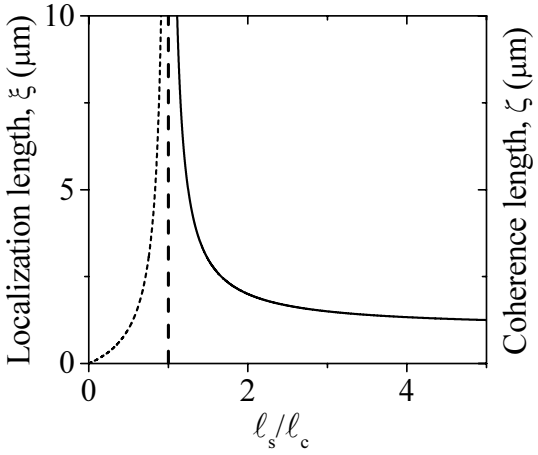

Figure 2.7:
Coherence length ζ (solid line) and localization length ξ (dotted line) as a function of ℓ_s/ℓ_c. The localization transition $\ell_s = \ell_c$ is marked with the dashed line.

If the system is formed by isotropic scatterers, i.e., $\ell_B = \ell_s$, the coherence length is

$$\zeta = \frac{\ell_s^2}{\ell_s - \ell_c} \,. \tag{2.57}$$

The coherence length in such a system is plotted in Fig. 2.7 as a function of the proximity to the localization transition.

In a weak scattering sample, i.e., $\ell_s \gg \ell_c$, Eq. (2.57) is $\zeta \simeq \ell_s$. In this limit interference is irrelevant, and $\ell = \ell_B$. Close to the transition ζ diverges, which means that in a finite sample it is the sample size L which sets the scale on which interference needs to be considered in the determination of ℓ. The transport mean free path in a finite sample at the transition is

$$\ell(L) \simeq \ell_B^2/L \,. \tag{2.58}$$

This scale dependence of ℓ can be understood with the help of Fig. 2.8, where a sample of linear size L at the localization transition is represented. If the source of radiation is at the center of the sample, waves propagating along closed paths contained within the sample volume will interfere, leading to a renormalized mean free path. However, waves propagating along longer paths will leak out of the sample. As the size of the sample is increased also the number of paths that interfere increases, giving rise to a larger renormalization. Only in an infinite sample the transport mean free path will vanish completely. Localization is thus the result of adding the interference contribution of all possible paths.

Optical absorption removes waves propagating along distances longer than L_a, preventing them to interfere. If $L \gg L_a$, the transport mean free path at the

transition is

$$\ell(L \gg L_a) \simeq \ell_B^2/L_a \, . \tag{2.59}$$

A natural interpolation of Eqs. (2.55), (2.58) and (2.59) is [28, 75]

$$\ell(L) \simeq \frac{\ell_B^2}{\zeta} + \frac{\ell_B^2}{L} + \frac{\ell_B^2}{L_a} \, . \tag{2.60}$$

It is important to note that in Eq. (2.60) the finite absorption and sample thickness are included with the same weight as cut-off lengths for ζ. This equal weight is only valid for samples with the geometry of a cube. Most of the experiments in random media of scatterers are done in layers of scatterers with x and y dimensions much larger than the thickness. For such samples the contribution of absorption in Eq. (2.60) is expected to be more important than the finite thickness. Light paths longer than L_a are removed due to absorption while paths much longer than L are still possible along the $x-y$ planes.

If the size of the sample is larger than the coherence length the wave will resume its diffuse propagation with a renormalized transport mean free path. Above the transition it is thus still valid to use the results derived from the diffusion approximation (section 2.2) with the substitution of ℓ_B by ℓ.

A more interesting situation occurs in non-absorbing samples if the coherence length is larger than the size of the sample, i.e., in the vicinity of the localization transition. The diffuse total transmission is calculated with the substitution of ℓ_B by $\ell(L)$ in Eq. (2.34). In the limit $\zeta \to \infty$ and $L_a \to \infty$ the diffuse total transmission is

$$T_d \propto \frac{\ell_B^2}{L^2}. \tag{2.61}$$

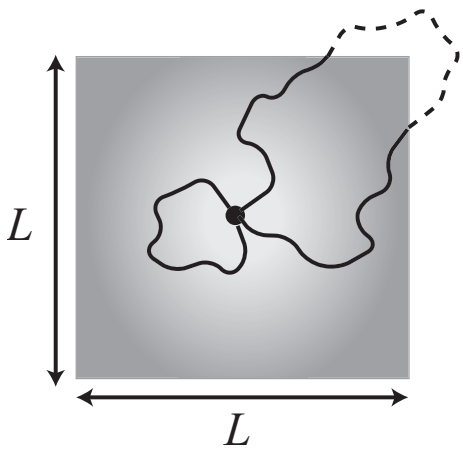

Figure 2.8:
Sample of size L at the localization transition. Waves propagating along paths contained in the volume defined by the sample will interfere. Longer paths will leave the sample.

The diffuse total transmission scales with L^{-2} in contrast with its L^{-1} dependence far from the transition. This scale dependence has been measured for microwave radiation [43] in a system of teflon and aluminum spheres, and for near-infrared radiation in samples of GaAs particles [76].

In the localized regime, i.e., $\ell_s < \ell_c$, the wave cannot propagate. The wave is localized in a length scale given by the localization length ξ. For isotropic scatterers the localization length is [67]

$$\xi = \frac{\ell_s^2}{\ell_c - \ell_s} . \tag{2.62}$$

The localization length is plotted versus ℓ_s/ℓ_c in Fig. 2.7 (dotted line). Localization means that the amplitude of the wave decreases exponentially with the distance to the source. The transmitted intensity through a sample in the localization regime is given by

$$T \propto \exp(-L/\xi) . \tag{2.63}$$

It is important to note that the scale dependence of the transmission in the case of localization in a non-absorbing medium Eq. (2.63) is the same as in an absorbing system in the classical diffusion regime Eq. (2.36). This equal dependence complicates greatly the interpretation of the total-transmission measurements [77].

The renormalization of the ℓ_B can be expressed as a renormalization of the Boltzman diffusion constant

$$D(L) \simeq D_B \left(\frac{\ell_B}{\zeta} + \frac{\ell_B}{L} + \frac{\ell_B}{L_a} \right) . \tag{2.64}$$

The time required by a wave to diffuse from one side of a sample to the opposite one is $\Gamma(L) = L^2/D(L)$. Far from the transition this time is proportional to L^2. In the vicinity of the transition, i.e., if $\zeta \gg L$, and in a non-absorbing sample the diffusion constant is $D(L) = D_B \ell_B / L$, and the transit time is $\Gamma(L) \propto L^3$. Near the transition the wave experiences a slowing down, which will show up as a long-time tail in the transmitted pulse.

Another way to study the localization transition is by measuring the coherent beam transmitted through the sample from which ℓ_s can be obtained (see section 2.1). We have seen that for dielectric scatterers and far from the transition $\ell_B = \ell \geq \ell_s$, Eq. (2.6). Close to the transition ℓ should become smaller than ℓ_s (see Fig. 1.4). The knowledge of both mean free paths provides an important tool in the study of localization.

Anderson localization affects also the enhanced backscattering. As we have seen in section 2.3, all optical paths contribute to the EBS intensity only at the

backscattering direction $\theta = 0$. The wings of the EBS cone are due to low-order scattering [123]. In the localization regime the wave is localized on a length scale given by ξ. In a EBS experiment the maximum distance between the first and the last scatterer in the medium will be of the order of ξ. This limitation on the path-length distribution gives rise to a similar effect on the EBS intensity than optical absorption and the finite size of the sample (see section 2.3), i.e., a flattening of the EBS intensity at $\theta \sim 0$. A rigorous treatment of the shape of the EBS in the localization regime can be found in Ref. [129]. The flattening of the EBS due to the onset of Anderson localization has been measured in porous GaP samples at optical wavelengths [79].

3

Near infrared transmission through powdered samples

Measurements of the total transmission in the near infrared through layers of randomly-packed Si and Ge micron-sized particles are presented in this chapter. In the wavelength range $1.4 - 2.5\ \mu$m, the scattering properties and the effect of residual absorption are analyzed. The sample-preparation method is explained in section 3.2. The measurements were done with a Fourier transform infrared spectrometer. The experimental set-up is described in section 3.3. Very strong scattering ($k\ell_s \simeq 3$ at $\lambda_o = 2.5\ \mu$m) and significant absorption at shorter wavelengths than $2\ \mu$m are measured in the Si samples [90, 94]. The energy density coherent potential approximation (EDCPA) is used to calculate the scattering mean free path and the localization parameter in the Si samples. We find good agreement between the calculations and the total-transmission experiments [85, 90]. In the Ge samples the total transmission decays exponentially with the sample thickness at all wavelengths in the studied range (section 3.5). This dependence of the total transmission can be due to strong localization or to optical absorption. By measuring the total transmission through the Ge samples filled with a non-absorbing liquid, a method which makes possible to discard or not optical absorption is introduced [91]. We find that in the Ge samples absorption has been introduced, presumably during the powder preparation.

3.1 Introduction

In spite of the great effort to localize light in systems formed by dielectric media [24, 75, 88, 120], there is no evidence of localization in such systems. Titanium dioxide TiO_2 is the dielectric with the highest refractive index in the visible $n = 2.7$ [130]. The lowest value of the localization parameter measured in TiO_2 samples is $k\ell_s \simeq 7$ [24]. These samples were close-packed powders of particles with an average radius of 110 ± 35 nm. This average radius corresponds to the

maximum scattering cross section of Mie scatterers in the visible (section 1.1). Moreover, since the surrounding medium of the scatterers in a powder is air, the refractive index contrast in the TiO_2 powders is maximum.

Although probably a lower value of $k\ell_s$ can be reached in TiO_2 samples by reducing the polydispersity; most likely a refractive index contrast of 2.7 does not suffice to localize light. The scattering mean free path in TiO_2 samples will thus depend on the particle radius and wavelength as indicated by the upper line of Fig. 1.5, i.e., the localization transition is not reached in TiO_2 samples for any value of the scatterers radius and at any wavelength.

Some semiconductors, as it is shown in Fig. 1.6, have higher refractive indexes than TiO_2. They are good candidates for preparing materials where light is localized. The absorption coefficient of intrinsic semiconductors is very low ($\alpha \gtrsim 0.1\text{cm}^{-1}$) in a spectral window limited at short wavelengths by the semiconductor band gap λ_{gap}, and at long wavelengths by free-carrier absorption and phonon bands. Since it is believed that optical absorption destroys localization [42, 43], the search for localization is limited to this wavelength window.

Silicon is a thoroughly studied semiconductor. Its high refractive index $n = 3.5$ [132], its non-toxic properties, and the ease with which it can be obtained, persuaded us to start the localization experiments with Si powders. The band gap of Si is at $\lambda_{gap} = 1.1\ \mu$m, which limits the experiments to the infrared.

Germanium has an even larger refractive index than Si, $n = 4$ [133]. Therefore, we also decided to study the propagation of light in Ge powders. The band gap of Ge is at $\lambda_{gap} = 1.85\ \mu$m.

A few months after the work presented in this thesis was initiated, localization of near-infrared radiation $\lambda_o = 1.067\ \mu$m was reported in GaAs powders [76]. GaAs particles were made by milling intrinsic semiconductor. Total-transmission and enhanced-backscattering measurements were performed in three kind of GaAs samples with different average particle radius $r \simeq 5, 0.5$ and $0.15\ \mu$m. The size of the particles was regulated by the time that the material was milled.

The measurements in the GaAs samples with $r \simeq 5\ \mu$m particles could be explained in terms of classical diffusion. The big particle size compared to the wavelength leads to a small scattering cross section and an inefficient scattering (section 1.1). In the samples with particles of average radius $r \simeq 0.5\ \mu$m, the total transmission decreased with the inverse of the square of the sample thickness. According to Eq. (2.61), these samples are close to the localization transition. The EBS measurements on these samples could not be explained with classical diffusion theory. The exponential decay of the total transmission with the size of the samples with the smallest particles, and the rounding of the EBS cone of these samples were attributed to strong localization.

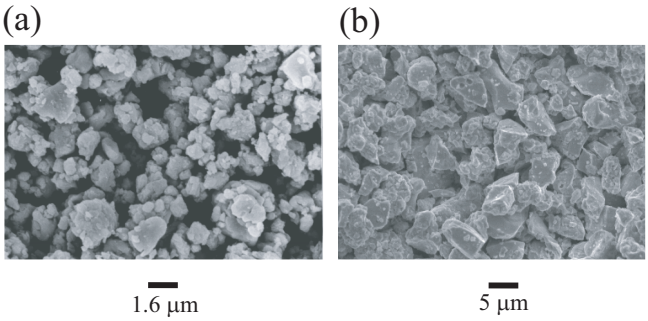

Figure 3.1: SEM photographs of Si (a) and Ge (b) powders

The interpretation of these measurements in terms of Anderson localization was questioned [77]. Since the milling time is longer for the samples with the smallest particles, Scheffold *et al.* [77] reasoned that in these samples stronger absorption introduced during the preparation might be expected. These authors claimed that the transmission and the EBS measurements could be then explained by classical diffusion with optical absorption.

This disagreement in the interpretation of the measurements in GaAs powders made clear that systematic studies of the optical scattering and absorption in semiconductor powders were necessary.

3.2 Sample preparation

The starting materials for the fabrication of the samples were commercially available Si and Ge powders.[1] The Si powder was formed by polycrystalline particles with sizes ranging from a few hundred nanometers to about 40 μm and with a purity of 99.999%. The Ge powder had a purity larger than 99.999% and the particle size was smaller than 150 μm.

To reduce the polydispersity of the Si powder, the particles were suspended in spectroscopic-grade chloroform and they were let to sediment for 300 s. Only the particles that did not sediment were used in the experiments. The Ge powder was first milled at low speed.[2] A zirconia beaker and balls were used for the milling. After 240 s, 5 ml of spectroscopic-grade methanol were added and the suspension was milled during 60 s. The resulting particles were sedimented during 150 s.

The particle size and polydispersity were evaluated from SEM photographs like the ones shown in Figs. 3.1 (a) and (b). Figure 3.1 (a) corresponds to Si particles, while in Fig. 3.1 (b) Ge particles are shown.

[1] Si: Cerac S-1049; Ge: Aldrich 32739-5

[2] The milling was done with a planetary micro mill, Pulverisette 7, Fritsch GmbH.

As can be seen in the figure, the Si particles tend to aggregate into clusters. This makes the definition of their radius difficult. The average radius of the particles was evaluated with two different methods: a) considering all the particles as entities, independently of whether or not they are part of a cluster, and b) considering the clusters as single particles. The radius of the particles (or clusters) was defined as half the Feret's diameter, which is the distance between two tangents to the particle surface, parallel to some fixed direction, and on opposite sides of the particle [134]. Figure 3.2 shows the normalized histograms of the particle radius obtained with both methods. In general, particles prepared by milling or grinding present a log-normal distribution of sizes $y = C\exp[-\ln^2(r/r_c)/2W^2]$ [134]. The fit of this function to the histogram obtained with method a) gives $C = 0.90$, $r_c = 0.19\,\mu$m, $W = 0.61$, and it is shown by the solid line in Fig. 3.2; while method b) gives $C = 0.86$, $r_c = 0.44\,\mu$m, $W = 0.55$, and it is represented by the dashed line in the same figure. These fits allow to calculate the average radius of the particles and its standard deviation: a) $r = 0.33 \pm 0.22\,\mu$m, and b) $r = 0.69 \pm 0.41\,\mu$m. The polydispersity, defined as the ratio between the standard deviation and r in percentage, is of 67% and 59% respectively. In other words, the Si samples are constituted of highly polydisperse scatterers.

For the Ge particles no aggregation was observed, making the determination of the particle radius simpler than in the case of the Si powders. From the fit of the histogram of the particle radius in the Ge powder with a log-normal distribution function the average radius was found to be $r = 2.1 \pm 0.9\,\mu$m and the polydispersity 43%.

To form layers of Si or Ge powders, a few drops of the suspensions were put on

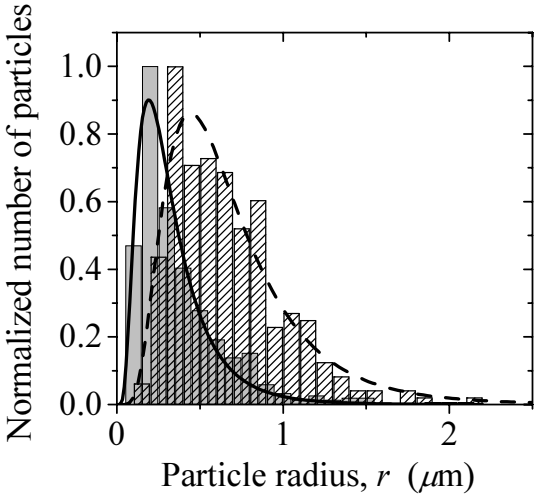

Figure 3.2: Normalized histograms of the radius of the silicon particles considering all the particles as entities, independently of whether or not they are part of a cluster (solid bars), and considering the clusters as single particles (dashed bars). The solid and dashed lines are log-normal fits, from which the average radius are calculated.

glass substrates and the chloroform or methanol was let to evaporate. The resulting samples are stiff slabs of close-packed Si or Ge particles in an air matrix.

The thickness L of the layers were measured by making scratches at the edges of the samples. With a calibrated microscope, with a resolution of 1 μm, the images of the surface of the sample and the substrate were focused. The thickness is given by the difference between the focus points. For each sample the thickness was measured at different places within its central region to be sure that the layer was homogeneous. The thickness of the layer is defined as the average value of these measurements.

The volume fraction occupied by the particles, $\phi \simeq 40\%$, was determined by weighting the samples.

3.3 Experimental set-up

The set-up used for the total-transmission measurements is depicted in Fig. 3.3. The total transmission was measured with a Fourier transform infrared spectrometer (FTIR).[3] The FTIR consists of a Michelson interferometer in which one mirror is fixed and the other is scanned over a distance of 8 cm at a velocity of 0.16 cm/s. The spectral resolution of the measurements was 8 cm^{-1}. The signal produced on three detectors by the beam of a He:Ne laser (not plotted in Fig. 3.3) is used to calculate the displacement of the moving mirror and to perform the dynamic alignment. Small misalignments of the interferometer are automatically corrected by means of piezoelectric actuators on the fixed mirror.

The high stability of the FTIR allowed to perform several scans, which were averaged to increase the signal-to-noise ratio. Typically, between 250 and 1000 scans were averaged depending on the total transmission of the sample.

A tungsten-halogen lamp has been used as light source. Short wavelengths were optically filtered. A lens with a focal distance of 15 cm and an iris with a diameter of 2 mm, placed in front of the sample, insured that the total transmission was measured only in the region where the thickness was characterized.

The light transmitted diffusively was collected with a $BaSO_4$ coated integrating sphere,[4] and detected with a PbSe photoconductive cell. The total transmission is given by the Fourier transform of the interferogram. Before and after measuring each sample, the transmission through a clean glass substrate was recorded. This measurement was used as reference to obtain the absolute value of the total transmission through the samples and to check the stability of the set-up.

[3] BioRad FTS-60A.

[4] Labsphere IS040SF

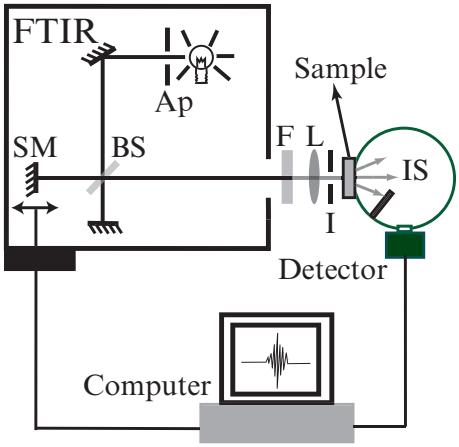

Figure 3.3: Experimental set-up used for the total-transmission measurements. FTIR: Fourier transform infrared spectrometer, BS: beam splitter, SM: scanning mirror, F: optical filter, L: lens, I: iris, IS: integrating sphere.

3.4 Total transmission through Si samples

Figure 3.4 shows a total-transmission spectrum of a sample of Si powder with a thickness of $L = 57.8 \pm 2\ \mu$m (solid line), and the transmission spectrum of a Si wafer (dashed line). For an easier comparison, both measurements have been normalized by their maximum transmissions. The sharp band gap ($\lambda_{gap} = 1.1\ \mu$m) can be clearly observed in the spectrum of the Si wafer. The total transmission of the powdered sample is very low at wavelengths close to the band gap due to strong scattering and/or optical absorption. To quantify these two contributions, a series of samples with different thickness was measured. The total-transmission measurements of Si layers are plotted in Fig. 3.5 as a function of their thickness. The squares correspond to $\lambda_o = 2.5\ \mu$m and the circles to $\lambda_o = 1.4\ \mu$m.

If the effective refractive index n_e of the sample is known, the extrapolation lengths, z_{e_1} and z_{e_2}, can be calculated using Eq. (2.17). The effective refractive index can be experimentally obtained from the measurement of the angular-resolved transmission (see section 2.2.3). This measurement is not easy to perform with a FTIR spectrometer due to the low intensity of the light source. As the volume fraction occupied by the particles is known to be $\simeq 40\%$, n_e can be estimated. Taking n_e as the Maxwell-Garnet effective refractive index [116], we find $n_e \simeq 1.5$ in the wavelength range $1.4 - 2.5\ \mu$m. With this value of n_e the extrapolation lengths of the Si-air and Si-substrate interfaces are $z_{e_1} = 2.42\ell$ and $z_{e_2} = 0.78\ell$ respectively. Note that reflections on the substrate-air interface will modify the value of z_{e_2}. If infinite reflections are considered $z_{e_2} = 2.4\ell$ [135]. However, the value of ℓ obtained from the fits of Eq. (2.42) to the total-transmission measurements is independent of z_{e_2} as long as $L \gg z_{e_2}$, which is the case in the investigated samples.

As it is shown by the solid lines of Fig. 3.5, the measurements of the total

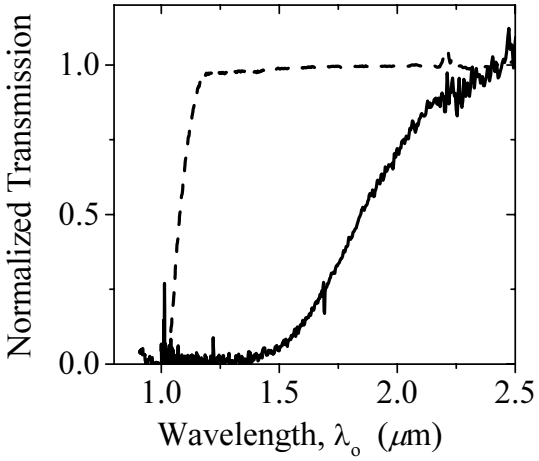

Figure 3.4:
Transmission spectra normalized to their maximum transmissions. Solid line: total-transmission spectrum of a layer of silicon powder with a thickness of 57.8 μm. Dashed line: transmission spectrum of a silicon wafer.

transmission can be fitted excellently by using classical diffusion theory. The fit of Eq. (2.42) to the $\lambda_o = 2.5\ \mu$m measurements yields $\ell = 0.83 \pm 0.08\ \mu$m. At this wavelength $L_a \gg L$, thus absorption can be neglected. From the fit to the $\lambda_o = 1.4\ \mu$m measurements $\ell = 0.56 \pm 0.06\ \mu$m and $L_a = 8.8 \pm 1\ \mu$m are obtained.

The wavelength dependence of L_a is plotted in Fig. 3.6. The increase of absorption for $\lambda_o < 2.0\ \mu$m is due to strain in the Si lattice structure. The presence of strain in the Si particles was confirmed from the width of X-ray diffraction peaks. Strain gives rise to a deformation of the potential, which smears the valence and conduction bands of the semiconductor. This deformation results in an edge of the band gap that extends into longer wavelengths than λ_{gap}. This absorption edge is known as the Urbach edge [136], and gives rise to an absorption length that

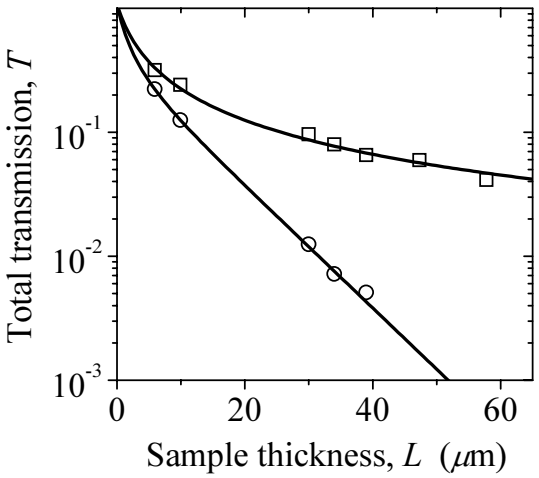

Figure 3.5:
Total transmission through Si powder versus the thickness of the sample L. The squares and the circles are the measurements at $\lambda_o = 2.5\ \mu$m and $\lambda_o = 1.4\ \mu$m respectively. The solid lines are fits using diffusion theory with $z_{e_1} = 2.42\ell$ and $z_{e_2} = 0.78\ell$. At $\lambda_o = 2.5\ \mu$m the transport mean free path is $\ell = 0.83\ \mu$m, and optical absorption is negligible. At $\lambda_o = 1.4\ \mu$m the absorption length is $L_a = 8.8\ \mu$m and $\ell = 0.56\ \mu$m.

increases exponentially with the wavelength

$$L_a \propto \exp\left(\frac{\lambda_o}{\lambda_U}\right) . \tag{3.1}$$

The fit of the measurements to Eq. (3.1) is represented by the line in Fig. 3.6, where $\lambda_U = 0.15 \pm 0.01$ μm.

The transport mean free path ℓ is plotted in Fig. 3.7 as a function of λ_o. C.M. Soukoulis from Iowa State University and K. Busch from the University of Karlsruhe have used the energy density coherent potential approximation EDCPA (see appendix A) to calculate the scattering mean free path in a random medium composed of Si spheres ($\phi = 40\%$) with a size distribution given by a log-normal function ($C = 0.86$, $r_c = 0.44$ μm, $W = 0.55$). The solid line in Fig. 3.7 is a convolution of the calculated ℓ_s for the specific sizes of the spheres with the probability density function given above.

As can be seen in Fig. 3.7, there is a good qualitative agreement between the measured ℓ and the calculated ℓ_s. The quantitative difference can be attributed to several factors: first, with the EDCPA ℓ_s is obtained, whereas the total-transmission measurements give ℓ. Second, for the EDCPA calculation the scatterers are considered perfect spheres, which clearly is not the case in the Si samples. Finally, as pointed out before, there is not an unambiguous way of measuring the particle radius due to the aggregation of Si particles. The best agreement between theory and experiments is found when the particle clusters are considered as single scatterers.

For comparison, in Fig. 3.7 we have also plotted the calculated ℓ_s in a system composed by monodisperse Si spheres of radius 0.44 μm and a volume fraction of

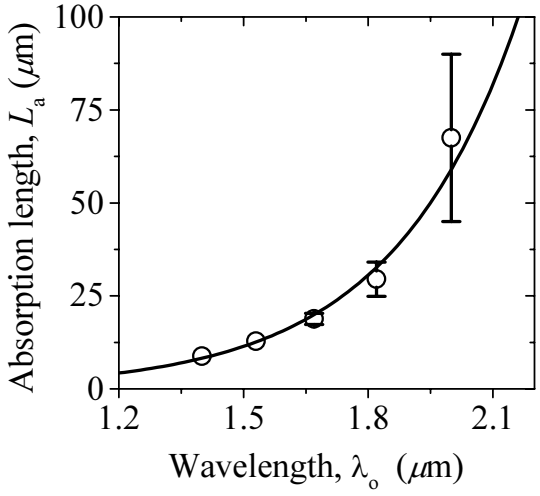

Figure 3.6: Absorption length in silicon powders versus the wavelength. The solid line is a fit to Eq. (3.1), with $\lambda_U = 0.15$ μm

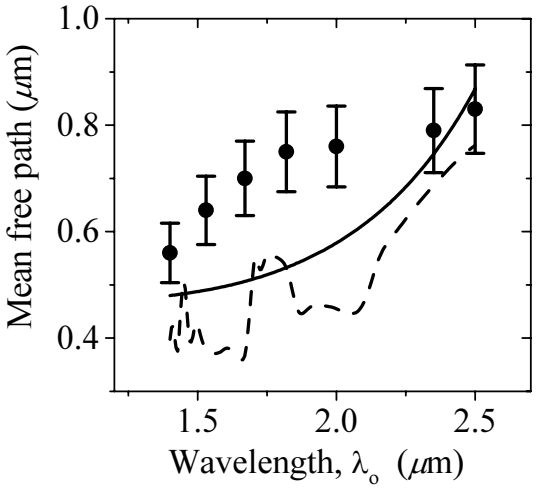

Figure 3.7:
Transport mean free path measured in Si powders versus the wavelength. The solid line is a convolution of the scattering mean free path, calculated with the EDCPA, for a distribution of sizes of the Si spheres given by the dashed line of Fig. 3.2 and with a Si volume fraction $\phi = 40\%$. The dashed line is ℓ_s calculated for a monodisperse system of Si spheres (radius=0.44 μm) and the same volume fraction [90].

40% (dashed line). As can be seen in Fig. 3.7, the scattering mean free path in a polydisperse system is in general larger than in a monodisperse one. It is more favorable to have a medium formed by scatterers with the largest possible σ_s. A polydisperse sample will contain particles which efficiently scatter light, together with inefficient scatterers. Therefore, the high polydispersity in the particle size constitutes the main limitation to the scattering strength in the Si samples.

With the transport mean free path obtained from the measurements of the total transmission, and assuming that the Si particles are isotropic scatterers $\ell = \ell_s$,[5] we can estimate the localization parameter, $k\ell_s = 2\pi n_e \ell_s/\lambda_o$. The values of $k\ell_s$ are plotted in Fig. 3.8 as a function of λ_o. The weak dependence of ℓ with λ_o, due to the high polydispersity in the samples, gives rise to a nearly constant scattering strength. The solid line in Fig. 3.8 represents the localization parameter using the values of ℓ_s that are obtained from the EDCPA calculation.

It must be stressed that, although the presented results can be explained using classical diffusion theory, the Si samples are very close to the critical value of $k\ell_s \simeq 1$. In fact, the localization parameter $k\ell_s \simeq 3$ at $\lambda_o = 2.5\ \mu$m is more than a factor of two smaller than the lowest value of $k\ell_s$ reported in TiO_2 powders [24].

3.5 Total transmission through Ge samples

The total-transmission spectrum of a sample of Ge powder with a thickness of $L = 12.4 \pm 1.2\ \mu$m is plotted in Fig. 3.5 (solid line). The band gap of intrinsic Ge

[5]Note that by setting ℓ equal to ℓ_s interference effects are obviated.

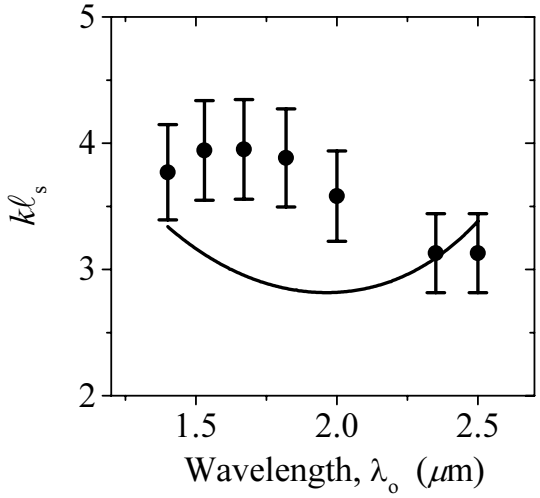

Figure 3.8:
Localization parameter $k\ell_s$ in silicon powders versus the wavelength. The solid line is the localization parameter calculated with the EDCPA in a polydisperse system of Si spheres.

is indicated in the same figure with an arrow.

Like with Si, the total transmission through Ge powder was measured in layers with different thickness. Figure 3.10 shows the total transmission versus the sample thickness at $\lambda_o = 1.7$ μm (circles) and at $\lambda_o = 2.5$ μm (squares). In the entire spectral range of the measurements the total transmission decreases exponentially with the sample thickness. The characteristic length of this exponential decay, named L_d, is plotted in the inset of Fig. 3.10 as a function of the wavelength. At $\lambda_o = 1.7$ μm it is not surprising this dependence since 1.7 μm $< \lambda_{gap}$, and strong absorption takes place.

Figure 3.9:
The solid line is the total-transmission spectrum of a layer of Ge powder with a thickness of $L = 12.4$ μm. The open circles are the total-transmission spectrum of the same sample with the air voids filled with CCl_4. The arrow indicates the band gap of intrinsic Ge.

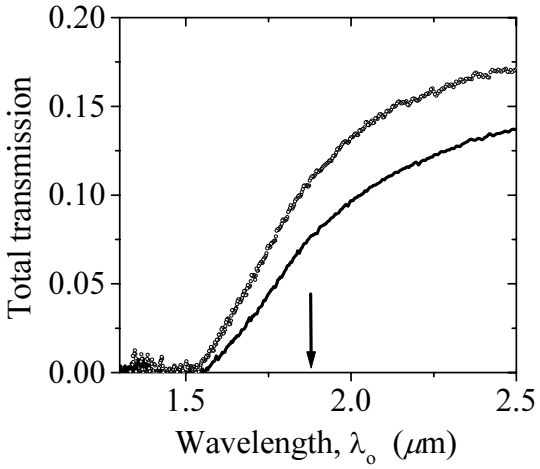

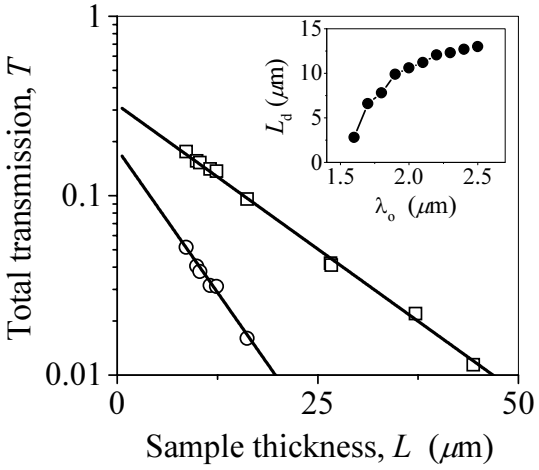

Figure 3.10: Total transmission through samples of Ge powder as a function of the sample thickness. The circles correspond to the measurements at $\lambda_o = 1.7$ μm and the squares to $\lambda_o = 2.5$ μm. As can be appreciated by the solid lines, the total transmission decays exponentially. Inset: wavelength dependence of the characteristic decay length of the total transmission L_d. The solid line is a guide to the eye.

The interpretation of the total-transmission measurements at $\lambda_o > \lambda_{gap}$ is more complicated. The absorption coefficient of intrinsic Ge at sub-band gap wavelengths is very low [133]. The exponential decay of the total transmission as a function of the sample thickness at these wavelengths could be attributed to strong localization in a non-absorbing medium. It is also possible that during the sample preparation impurities have been added to the Ge powder or defects are created at the surface of the particles, giving rise to an increase of the absorption coefficient.

To determine which of these two situations (localization or absorption) applies, the total transmission of the samples filled with carbon tetrachloride CCl_4 was measured. In the wavelength range under investigation, CCl_4 has a refractive index of $n = 1.4$ and it does not absorb [137]. By filling the samples the refractive index contrast between the scatterers and the surrounding medium is changed from 4.1 to 2.9. Therefore, the scattering cross section is reduced or equivalently the scattering and transport mean free paths are increased.

The total-transmission measurement of the sample with a thickness of $L = 12.4$ μm filled with CCl_4 is plotted in Fig. 3.5 (open circles). The higher transmission of the filled sample clearly confirms the increase of ℓ. After letting evaporate the CCl_4 the original spectrum was recovered. This means that the structure of the samples did not change and that CCl_4 only filled the voids between Ge particles.

The complete infiltration of the samples was carefully checked by measuring the change of the specular reflection of a beam from a He:Ne laser on the bottom of the samples upon the addition of CCl_4.

A refractive index contrast of 2.9 should be too low to induce localization, moreover in a system that is highly polydisperse. As the optical absorption of CCl_4 is negligible, if the exponentially-decaying total transmission at $\lambda_o > \lambda_{gap}$

is due to localization in a non-absorbing medium, the reduction of the refractive index contrast should give rise to a total transmission described by the diffusion approximation without absorption. On the other hand, if Ge absorbs significantly at these wavelengths, the filled samples should have a finite absorption length, $L'_{\rm a}$. For clarity, the parameters of the filled samples will be denoted with a prime.

Figure 3.11 shows the total-transmission measurements at $\lambda_{\rm o} = 2.5\ \mu$m of the Ge samples filled with CCl_4 as a function of the sample thickness. In the same figure a fit to the measurements using classical diffusion theory is plotted with a solid line. For the fit the extrapolation lengths are fixed to $z'_{\rm e_1} = z'_{\rm e_2} = (2/3)\ell'$ and the transport mean free path and absorption length are $\ell' = 1.53 \pm 0.1\ \mu$m and $L'_{\rm a} = 26 \pm 4\ \mu$m. For comparison, the total transmission through a non-absorbing medium with $\ell' = 1.53\ \mu$m is also plotted in Fig. 3.11 (dashed line).

As it has been mentioned in the preceding section, the value of $z'_{\rm e_2}$ does not affect the analysis of the total-transmission measurements. On the other hand, $\tau'_{\rm e_1} = z'_{\rm e_1}/\ell'$ needs to be carefully estimated to obtain a reliable value of ℓ'. Carbon tetrachloride forms a layer on top of the sample and $\tau'_{\rm e_1}$ depends on the reflections on the Ge-CCl_4 and the CCl_4-air interfaces. To estimate $\tau'_{\rm e_1}$ the number of reflections on these interfaces before the light leaks through the sample edges needs to be known. The number of reflections will depend on the exact thickness of the CCl_4 top layer [135], which is unknown. Therefore, in this experiment it is not attempted to obtain an accurate value of the transport mean free path, and by setting $z'_{\rm e_1}$ to its value in the case of refractive index matched interfaces, i.e., $(2/3)\ell'$, the transport mean free path is overestimated.

It is important to note that as $L'_{\rm a}$ is obtained from the decay of the transmission through the thickest samples, it is independent of the extrapolation lengths. As $L'_{\rm a}$

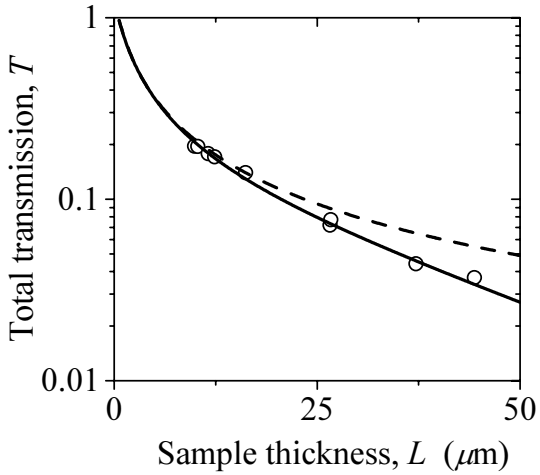

Figure 3.11: Total-transmission measurements of Ge samples filled with CCl_4 as a function of the sample thickness. The solid line is a fit using classical diffusion theory with $z'_{\rm e_1} = z'_{\rm e_2} = (2/3)\ell'$, from which the absorption length $L'_{\rm a} = 26 \pm 4\ \mu$m is found. The dashed line is the expected total transmission in a non-absorbing system with equal scattering strength.

for the filled Ge is of the order of L, we may conclude that the exponential decay of the total transmission in the non-filled Ge samples is not due to strong localization in a non-absorbing medium, but the role of absorption must be considered.

3.6 Discussion

As we have seen in section 3.4, in spite of the fact that the total-transmission measurements on Si powders can be fully described using diffusion theory, the localization parameter $k\ell_s \simeq 3$ at $\lambda_o = 2.5\ \mu$m is more than a factor of two smaller than the lowest value of $k\ell_s$ found in TiO_2 powders [24]. These results confirm that semiconductor materials are good candidates to prepare a medium where light is localized.

A problem in the search for localization in Si and Ge powders arises from the significant optical absorption that they exhibit. Improvements in the reduction of the absorption can be achieved by annealing the particles to minimize the contribution of surface defects.

A remaining open question is why strong localization of near-infrared light is apparent in GaAs powders [76], while it is absent in similar samples of Si powders. According to the EDCPA [85, 86], for a given refractive index contrast, the localization parameter is much lower in the inverse structure than in the direct structure (see appendix A). The inverse structure is formed by air scatterers in a high dielectric material. A possible explanation for a lower value of $k\ell_s$ in the GaAs samples could be a different connectivity of the particles. If the contact between neighboring particles is better in the GaAs than in the Si samples, due to a different particle shape, the GaAs samples may be represented by an inverse structure. For the Si samples a description in terms of a direct structure could be more appropriate.

It is also possible that the results of Ref. [76] have been misinterpreted in terms of localization without optical absorption [77]. More experimental work must be done in the GaAs samples. A feasible experiment, as it is clearly shown in section 3.5, consists in filling the air voids in the GaAs samples with a non-absorbing liquid and measure the total transmission or the enhanced-backscattered intensity [79]. This experiment could confirm that the deviation from diffusion theory in the measurements of Ref. [76] are due to localization or if absorption is present in the GaAs samples.

4

Midinfrared transport of light in Ge powders close to the localization transition

Midinfrared measurements in slabs of Ge powders, using a free electron laser, are presented in this chapter. To fully characterize the samples, several complementary techniques have been employed: coherent transmission (section 4.3.1), total transmission and reflection (section 4.3.2), and time-resolved speckle interferometry (section 4.4). In this way we obtained the scattering ℓ_s and transport ℓ mean free paths, the absorption coefficient α, the diffusion constant D, and the energy velocity v_e. The Ge samples are close to the localization transition ($k\ell_s \simeq 3$). As discussed in section 4.3.3, our measurements of ℓ_s and ℓ suggest that ℓ is renormalized due to interference at the proximity of the localization transition [92]. The diffusion constant is significantly reduced in samples thinner than $\simeq 7\ell$ [93]. This results are discussed in section 4.4. We have also performed photoacoustic spectroscopy in the Ge powders (section 4.5), a technique that allows to study the optical absorption.

4.1 Introduction

One of the greatest difficulties in the study of Anderson localization of light is to distinguish between optical absorption and strong localization. In many of the experiments the results in both cases look similar (see chapter 2).

In the preceding chapter we have seen that the near-infrared total transmission T through Ge powders decays exponentially with the sample thickness L. This decay at wavelengths larger than the band gap of Ge ($\lambda_{gap} = 1.85\ \mu$m) can be due to strong localization or to optical absorption. Reducing the refractive index contrast,

by filling the air voids of the Ge-powder samples with CCl_4, allowed to conclude that there is optical absorption in the unfilled samples.

An additional way to check if a total transmission that decays exponentially is due to strong localization in the absence of absorption consists in measuring the transmission at larger wavelengths. As explained in section 1.6, Anderson localization of light is only possible in a window where the scattering strength is maximal (see Fig. 1.5 on page 22). Suppose that we have a system in which light of wavelength λ is localized. Since the scattering strength depends on the wavelength, the transition is crossed at a critical wavelength. The total transmission close to the localization transition should vary with L^{-2} (Eq. (2.61)). If the scattering strength is further reduced by varying the wavelength, the diffusive dependence of the total transmission should be recovered (Eq. (2.34)).

Due to the magnitude of the band gap of Ge, the measurements need to be carried out in the infrared. For the experiments presented in this chapter, a mid-infrared free electron laser (FEL)[1] was used as tunable source of intense infrared radiation. The full capabilities of this FEL are described in Ref. [138]. The FEL is continuously tunable over the wavelength range $4.5-200\,\mu$m, and generates an intense train of picosecond pulses (micropulses). Each of the pulses has an energy of $\simeq 1\mu$J, and a fractional spectral bandwidth of about 1%. Each train of micropulses (called macropulse) contains about 100 micropulses, with an interpulse spacing of 40 ns. In the experiments showed below the signal from 25 macropulses was averaged for each measurement. The wavelength λ_o range of the experiments was $4.5-8\,\mu$m.

The measurements of the total transmission and reflection are also useful to determine if absorption is significant. As it has been explained in section 2.2.4, energy conservation requires that the total transmission plus the total reflection plus the absorption adds up to one. In the absence of absorption the total transmission plus the reflection are one. In the samples of Ge powder absorption is significant (section 4.3.2). This absorption is presumably introduced during the preparation of the samples.

Even in the presence of absorption it is interesting to search for localization effects. The measurement of the transmission of the coherent beam allows the determination of the scattering mean free path ℓ_s (section 4.3.1). From the total-transmission and reflection measurements the transport mean free path ℓ is obtained (section 4.3.2). Our measurements suggest that $\ell < \ell_s$, which evidences the renormalization of ℓ at the proximity of the localization transition. However, the large error in the determination of ℓ makes impossible to unambiguously prove localization effects in the Ge samples (section 4.3.3).

[1] FELIX, free electron laser for infrared experiments, Rijnhuizen, The Netherlands.

Last but not least, dynamic measurements are important. In the localized regime and in the absence of absorption, it is expected to find a long-time tail in a transmitted pulse (see section 2.4). Dynamic measurements were done by means of time-resolved speckle interferometry (section 4.4). The long-time behaviour of the transmitted pulse through the Ge samples is limited by optical absorption. As expected, the diffusion constant is lower at wavelengths at which the scattering is stronger. The energy velocity is strongly renormalized by resonant scattering.

4.2 Sample preparation

The Ge samples discussed in the preceding chapter were mounted on microscope glass substrates. This glass absorbs midinfrared radiation, hindering the possibility of performing transmission measurements. New samples were made on infrared-transparent CaF_2 disk-shaped substrates with a diameter of 12.7 mm and a thickness of 1 mm. The samples were prepared following the same procedure as the GaAs samples of Ref. [76]: the starting material was high-purity (99.9999%) Ge.[2] Two grams of Ge were ground with a mortar until all pieces were smaller than 1 mm. To further reduce the size of the particles and their polydispersity they were milled and sedimented as described in section 3.2.

Electron-microscope (SEM) images of the samples were taken to measure the size of the Ge particles and to check if the samples were homogeneous. Figure 4.1 (a) shows a side view of a Ge sample, along one of the scratches made to measure the sample thickness. The thickness was measured as explained in section 3.2. In Fig. 4.2 a schematic representation of a sample is presented. The dashed arrow in this figure shows the direction of observation in Fig. 4.1 (a). The sample is formed by a top layer of small particles and a bulk of much bigger Ge particles. For comparison, in Figs. 4.1 (b) and (c) photographs of the upper and lower surfaces of a sample are presented.

Energy-dispersion X-ray spectroscopy (EDX) measurements[3] on the top layer showed that it is mainly formed by Ge together with a small amount of impurities introduced during the milling. From SEM photographs of several samples, the thickness of the top layer, which we shall refer to as δ, was estimated to be $5 \pm 1\ \mu$m and constant for all the samples. Also from these photographs, it was checked that the size of the Ge particles in the bulk of the sample is the same at different depths, and that the size of the particles is the same in all the samples.

[2] Aldrich 26323-0.

[3] The EDX measurements were performed by R.L.W. Popma at the University of Groningen, The Netherlands.

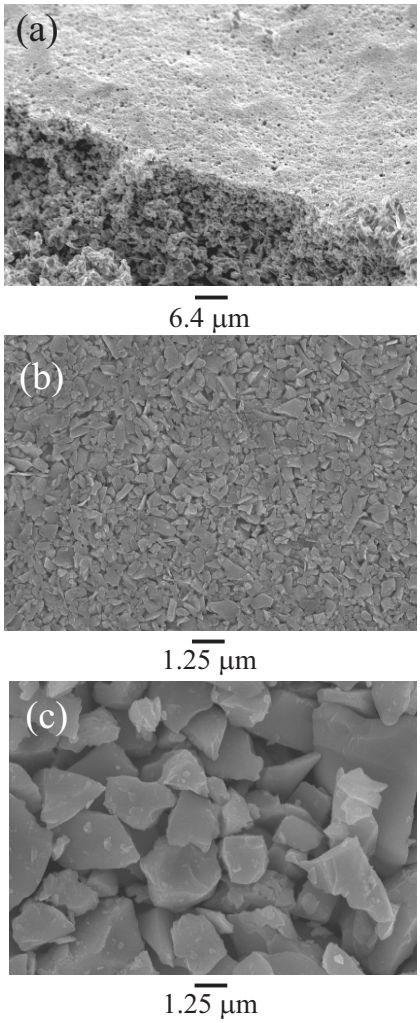

Figure 4.1:
SEM photographs of a sample of Ge powder. Photograph (a) shows a side view of the sample. The direction of observation is marked in Fig. 4.2 with a dashed arrow. Photograph (b) is the upper surface of the sample, while (c) shows the lower surface. Note that the magnification in photographs (b) and (c) is the same.

Defining the particle radius as half the Feret's diameter (see section 3.2), histograms of the particle radius in the top layer and in the sample bulk were obtained. By fitting these histograms to log-normal distribution functions, the average particle radius in the top layer is found to be 0.19 ± 0.13 μm and in the sample bulk 0.98 ± 0.68 μm.

According to Mie-scattering calculations, in the wavelength range of the experiments ($4.5 - 8$ μm) the scattering cross section σ_s of a Ge sphere of radius 0.19 μm in air is at least two orders of magnitude smaller than σ_s of a Ge sphere of radius 0.98 μm. Therefore, due to the small size of the particles of the top layer and to its thickness, the scattering in this layer is negligible. The samples may

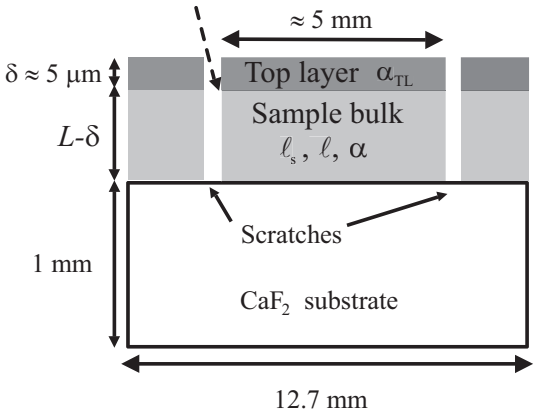

Figure 4.2:
Schematic representation of a sample of Ge powder. The thin top layer is formed by small Ge particles and impurities introduced during the preparation of the sample. The bulk of the sample is formed by bigger Ge particles. The dashed arrow shows the direction of observation in 4.1 (a). Also the scratches made on the sample to measure its thickness are represented.

be described as consisting of a homogeneous top layer of thickness $\delta = 5\ \mu$m in which only absorption takes place and a bulk of Ge particles, with a thickness $L - \delta$, where scattering and absorption occur. The absorption in the top layer is characterized by the absorption coefficient α_{TL}. Due to the irregular shape of the Ge particles and their random orientation, the scattering in the bulk of the sample will be assumed (nearly) isotropic. The absorption coefficient in the bulk is given by α. This two-layers model is needed to explain the total-transmission and reflection measurements that are presented in the next section.

4.3 Static measurements

Static measurements, i.e., coherent transmission and total transmission and reflection, are described in this section. The scattering and transport mean free paths and the absorption coefficients of the top layer and the sample bulk are obtained from these measurements (see chapter 2 for explanation).

4.3.1 Coherent beam transmission

To measure the coherent transmission the output of the FEL was sent through a beamsplitter and the reflected beam was directed to a broadband pyroelectric detector. The signal from this detector was used as power reference. An iris with a diameter of 0.1 cm was in front of the sample to insure that the FEL beam illuminated only its most homogeneous portion. Another iris with a diameter of 0.7 cm was placed at a distance of 120 cm from the sample and in the direction of the incoming beam. After this iris a BaF_2 lens focused the transmitted FEL beam onto a mercury-cadmium-telluride (MCT) detector. Due to the long distance between

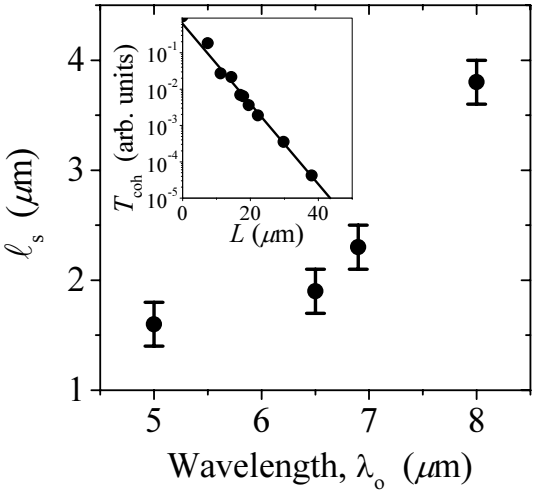

Figure 4.3:
Scattering mean free path in Ge powder as a function of the wavelength. Inset: measurements of the transmission of the coherent beam ($\lambda_o = 8\ \mu$m) as function of the sample thickness, L. The line is an exponential fit to the measurements from which ℓ_s is obtained. At this particular λ_o, $\ell_s = 3.8 \pm 0.2\ \mu$m.

the sample and the detector, the detected diffuse light was negligible. The transmission of the coherent beam was measured at four wavelengths, $\lambda_o = 5$, 6.5, 6.9 and 8 μm.

The transmission measurements of the coherent beam at $\lambda_o = 8\ \mu$m are plotted in the inset of Fig. 4.3 as a function of the sample thickness. Clearly, the transmission decreases exponentially with the sample thickness. As we have seen in section 2.1, if the absorption is weak, i.e., $\ell_s \ll \ell_a$, the characteristic length of the exponential decay is ℓ_s. In the next section is shown that the Ge samples are in the weak-absorption limit.

Figure 4.3 displays ℓ_s as a function of λ_o. The nearly constant value of ℓ_s at 5, 6.5 and 6.9 μm may be understood in terms of the high polydispersity in the size of the Ge particles. The effect of the polydispersity on the scattering properties of the medium has been discussed in section 3.4. Only at $\lambda_o = 8\ \mu$m, ℓ_s is significantly larger. It is expected that, as the wavelength becomes substantially larger than the scatterer radius, ℓ_s increases due to the reduction of the scattering cross section (see section 1.1 on page 9).

The localization parameter $k\ell_s$ is plotted as a function of λ_o in Fig. 4.4. The wave vector k is given by $\frac{2\pi}{\lambda_o} n_e$, where n_e is the effective refractive index of the sample bulk. Although it is possible to obtain n_e from the angular-resolved transmission (section 2.2.3), these measurements were not performed due to the limitation in the allotted beam time. As was done in the preceding chapter, we take for n_e the value given by the Maxwell-Garnet approximation [116]. With a Ge volume fraction of 40% [76, 90], it is found $n_e \simeq 1.6$ in the measured λ_o range.

As can be concluded from Fig. 4.4, the Ge powder samples are very close

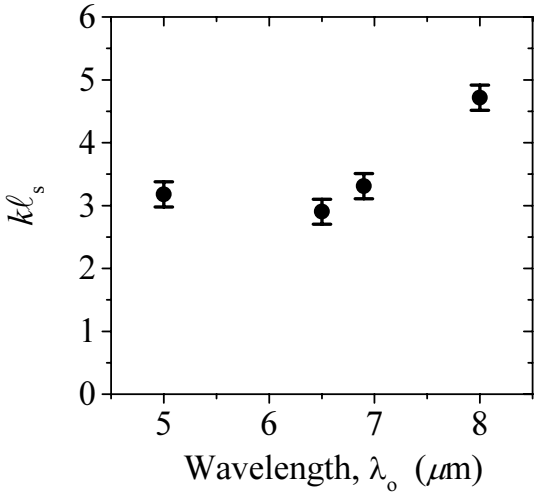

Figure 4.4: Localization parameter, $k\ell_s$, in Ge powder as a function of the wavelength.

to the localization transition ($k\ell_s$ close to 1) where localization effects, like the renormalization of the transport mean free path, are expected to occur.

4.3.2 Total transmission and reflection

To obtain the transport mean free path ℓ, total-transmission and total-reflection measurements were performed. The total transmission was measured as follows: the output of the FEL was brought to a weak focus of about 0.1 cm at the sample by using two BaF_2 lenses. The sample was mounted at the input of a infragold-coated integrating sphere (IS).[4] At the output of the IS was a MCT detector. A power reference was simultaneously measured in the same way as described for the coherent-beam experiments. The measurements were normalized by the transmission spectrum of a clean CaF_2 substrate.

For the measurement of the total reflection the FEL beam was sent into the IS through a small input port with a diameter of 0.3 cm. The sample was at the opposite side of the IS. Therefore, only the light reflected by the sample was collected by the IS. The reference for the reflection measurements was a thick infragold sample with a diffuse reflection $\simeq 96\%$ in the λ_o range $2 - 20\ \mu$m.

To measure the total transmission and reflection wavelength scans were made in the range $4.5 - 8\ \mu$m with steps of $0.1\ \mu$m. The lower limit is set by the tuning range of the FEL [138], while the higher is due to CaF_2 absorption [139] .

Figures 4.5 (a) and (b) display the spectra of the normalized total transmission and reflection of a Ge sample with a thickness $L = 73.2\ \mu$m. The spectra show

[4] Labsphere IS040IG.

two narrow absorption bands at 6.0 and 6.9 μm, which are, most likely, due to vibrational modes of hydrocarbon impurities introduced during the preparation of the sample. In section 4.5 is explained how photoacoustic spectroscopy can be used to investigate the optical absorption of the samples.

In the following it is shown how to deduce ℓ from the total-transmission and reflection measurements. In Fig. 4.6 typical measurements of the total transmission (a) and total reflection (b) are plotted as a function of the sample thickness. These measurements correspond to $\lambda_o = 8\,\mu$m. To obtain the transport mean free path, we first need to know the extrapolation factors $\tau_{e_1} = z_{e_1}/\ell$ and $\tau_{e_2} = z_{e_2}/\ell$. Given the effective refractive index of the Ge powder ($n_e \simeq 1.6$), and the refractive index of CaF_2, τ_{e_2} can be calculated. Considering the multiple reflections at the interface CaF_2-air [135] $\tau_{e_2} \simeq 2.7$. To obtain τ_{e_1}, the total-transmission measurements of the thickest samples are fitted to

$$T_d = A(\tau_{e_1}) e^{-\alpha_{TL}\delta} e^{-(L-\delta)/L_a} . \tag{4.1}$$

This equation is equivalent to Eq. (2.36) with the source attenuated by the factor $e^{-\alpha_{TL}\delta}$. This attenuation is due to absorption in the top layer of the sample. For isotropic scatterers and in the absence of interference, i.e., $\ell = \ell_s$, one finds, using

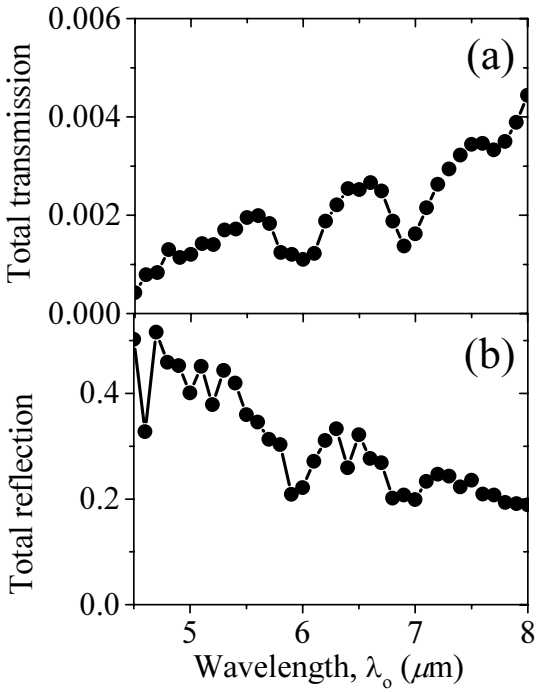

Figure 4.5:
Normalized spectra of the total transmission (a) and reflection (b) of a Ge powder sample of thickness 73.2 μm.

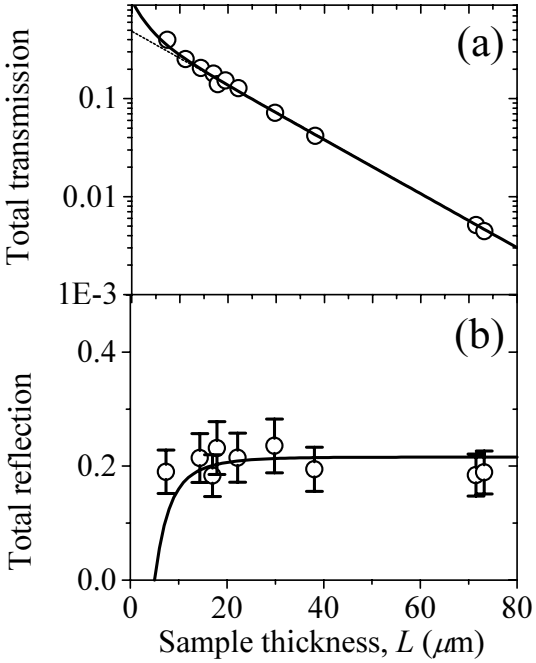

Figure 4.6:
Total-transmission (a) and reflection (b) measurements in samples of Ge powder at $\lambda_o = 8\ \mu$m as a function of the samples thickness. The solid line in (a) is a fit using classical diffusion theory. The dotted line (hidden by the solid line except at small L) is an exponential fit to the total transmission of the thickest samples. In (b) the solid line represents a fit of the total-reflection measurements using diffusion theory.

Eqs. (2.36), (2.37) and (4.1)

$$\tau_{e_1} = \frac{-2L_a\ell_s + A' L_a(L_a + \tau_{e_2}\ell_s)e^{\alpha_{TL}\delta}}{2L_a\ell_s - A'\ell_s(L_a + \tau_{e_2}\ell_s)e^{\alpha_{TL}\delta}} , \tag{4.2}$$

where A' is given by Eq. (4.1) at $L = \delta$. Note that to obtain Eq. (4.2), the location of the source of diffuse radiation z_p is assumed to be at a distance ℓ_s from the sample interface. The dotted line in Fig. 4.6 (a) represents a fit of Eq. (4.1) to the $\lambda_o = 8\ \mu$m measurements. From the fit $A' = 0.35 \pm 0.05$ and $L_a = 15.5 \pm 0.5\ \mu$m. To obtain τ_{e_1} from Eq. (4.2) we need to know α_{TL}. The total-reflection measurements are more sensitive to the absorption in the top layer because the reflected light crosses this layer twice. Therefore, the low reflection exhibited by the samples (only 20% at $\lambda_o = 8\ \mu$m) is mainly due to strong absorption in the top layer. To estimate the absorption α_{TL}, the total reflection measurements are fitted with

$$R = e^{-\alpha_{TL}\delta} R_d \int_0^1 e^{-\alpha_{TL}\delta/\mu_e} P(\mu_e)\, d\mu_e , \tag{4.3}$$

where $\mu_e = \cos\theta_e$ and θ_e is the angle with respect to the normal of the sample surface at which the diffuse reflected light exits the sample bulk. The diffuse reflected light is angularly distributed according to $P(\mu_e) \propto \mu_e \left(\frac{2}{3} + \frac{\mu_e}{1+\mu_e}\right)$ [120], where it is

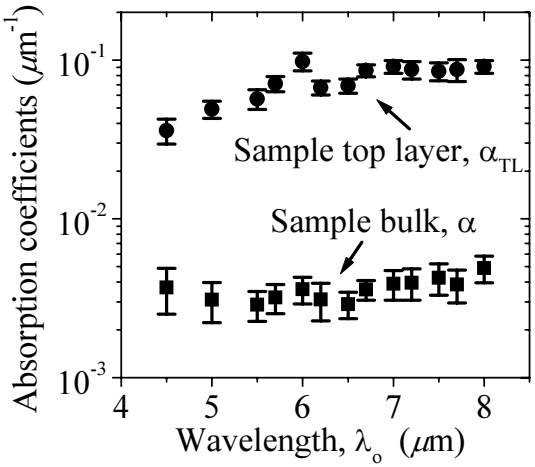

Figure 4.7:
Circles: absorption coefficient in the top layer of the samples of Ge powder as a function of the wavelength. Squares: absorption coefficient in the bulk of the samples.

assumed that the bulk of the sample and the top layer have the same index of refraction. This assumption is plausible since we know from the EDX measurements that the top layer is mainly formed by Ge and from the SEM photographs that the packing of the particles is similar in both regions. The factor $e^{-\alpha_{TL}\delta}$ in Eq. (4.3) represents the attenuation of the coherent beam due to absorption in the top layer, R_d is the diffuse total reflection of the sample bulk and the integral represents the attenuation of the diffuse reflected light due to absorption in the top layer.

In Eq. (4.3) the scattering is considered isotropic, and reflections at the interface top layer-air are neglected. By neglecting these reflections a higher value of α_{TL} is obtained from the fit than the real one. The overestimation of α_{TL} is $\simeq 15\%$. This overestimation is irrelevant for the value of the transport mean free path that will be obtained from the fit to the total transmission. The fit of Eq. (4.3) to the reflection measurements at $\lambda_o = 8\,\mu$m is shown as a solid line in Fig. 4.6 (b). From this fit $\alpha_{TL} = 0.091 \pm 0.008\,\mu\text{m}^{-1}$.

The scattering mean free path was directly measured at $\lambda_o = 5$, 6.5, 6.9 and 8 μm. To obtain α_{TL} at intermediate wavelengths, the values of ℓ_s were linearly interpolated. The circles in Fig. 4.7 represent α_{TL} as a function of λ_o. Figure 4.8 displays the wavelength dependence of τ_{e_1}, as obtained from Eq. (4.2). The lower value of τ_{e_1} at the absorption bands (6.0 and 6.9 μm) should not be attributed to a decrease of the boundary reflectivity but to an increase of the absorption at the top layer. This dependence of τ_{e_1} with α_{TL} is discussed in appendix B.

With the values of τ_{e_1}, τ_{e_2}, α_{TL} and L_a we can obtain the transport mean free path from the total-transmission measurements using the following equation

$$T = e^{-\alpha_{TL}\delta}\left(T_d + e^{-(L-\delta)/\ell_s}\right) . \tag{4.4}$$

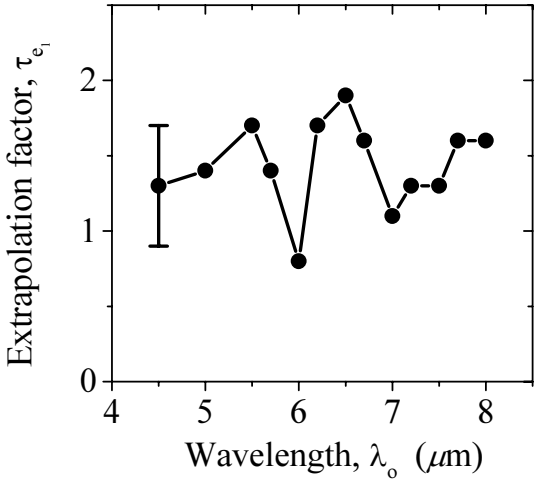

Figure 4.8:
Extrapolation factor τ_{e_1} of the Ge powder samples as a function of the wavelength. The solid line is a guide to the eye. The characteristic error is indicated only at $\lambda_o = 4.5\ \mu$m.

The solid line in Fig. 4.6 (a) is a fit of the total-transmission measurements to Eq. (4.4). The first term inside the bracket of Eq. (4.4) is the diffuse total transmission (Eq. 2.40 on page 35), while the second term is the transmission of the coherent beam. The factor $e^{-\alpha_{TL}\delta}$ represents the attenuation of the incoming beam due to absorption in the top layer. The transmission of the coherent beam rapidly decreases with L, and is negligible for thick samples. At $\lambda_o = 8\ \mu$m, with $\delta = 5\ \mu$m, $\tau_{e_1} = 1.6$, $\tau_{e_2} = 2.7$, $\alpha_{TL} = 0.091 \pm 0.008\ \mu\text{m}^{-1}$ and $L_a = 15.5 \pm 1\ \mu$m, we find from the fit $\ell = 3.5 \pm 0.5\ \mu$m. At this λ_o the incident beam is attenuated by more than 30% due to absorption in the top layer. The scattering properties of the Ge samples at $\lambda_o = 8\ \mu$m are listed in Table 4.1 on page 77.

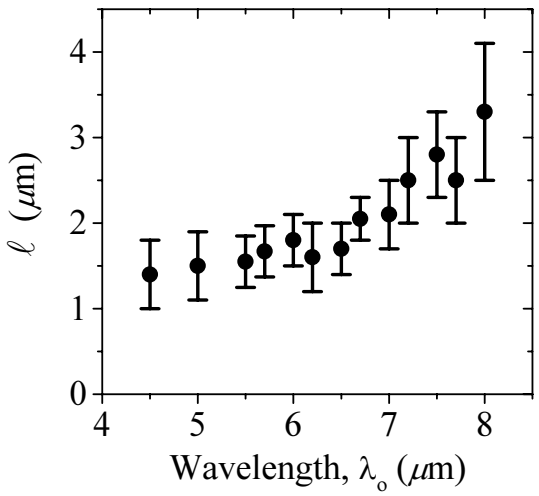

Figure 4.9:
Transport mean free path ℓ in the bulk of the Ge samples as a function of the wavelength.

The wavelength dependence of ℓ is plotted in Fig. 4.9. Consistently with the measurements of ℓ_s, the transport mean free path increases at higher λ_o due to the reduction of σ_s.

The squares in Fig. 4.7 are the absorption coefficient, $\alpha = \ell/(3L_a^2)$, in the bulk of the sample. Although the sample bulk is in the weakly-absorbing limit, i.e., $\alpha^{-1} = \ell_a \gg \ell$, absorption has been presumably introduced during preparation of the samples. Most likely surface defects in the Ge particles have been created during the milling and impurities have been introduced. The absorption is stronger in the top layer where the size of the particles is smaller. In this layer we have also detected impurities with EDX measurements.

4.3.3 Discussion

The ratio of the transport and scattering mean free paths is displayed in Fig. 4.10 (circles). The values of ℓ/ℓ_s are smaller than 1, which can be only understood by considering the renormalization of ℓ due to the proximity of the localization transition. For comparison, we also plot in Fig. 4.10 (squares) the expected renormalization of ℓ according to the scaling theory (Eq. (2.60)), assuming that the transition takes place at the critical scattering mean free path $\ell_c = \lambda_o/2\pi n_e$ and $n_e = 1.6$; and considering only the absorption as cut-off of the coherent length ζ. The large error in the determination of ℓ, related to the complicated structure of the samples and to the estimation of the extrapolation factor τ_{e_1}, makes it impossible to unambiguously prove localization effects. Besides, in the analysis to find τ_{e_1}, ℓ is fixed to ℓ_s in Eqs. (4.2) and (4.3), obviating any localization effect and assuming isotropic scattering. Nonetheless, it is demonstrated that both mean free paths can be experimentally obtained in strongly-scattering samples, and that the comparison of ℓ_s and ℓ represents a very useful tool to study the localization transition.

In the preceding chapter, the energy density coherent potential approximation was used to calculate the scattering properties of a system of polydisperse silicon spheres. The scattering mean free path is in general larger in a polydisperse medium than in a monodisperse. Therefore, a way to further approach the localization transition in Ge samples is to reduce its polydispersity.

An improvement in the reduction of the absorption could be achieved by annealing the Ge particles after the milling. To eliminate the hydrocarbon absorption bands at 6 and 6.9 μm methanol could be replaced during the sample preparation by a liquid that does not exhibit absorption in the wavelength range under study.

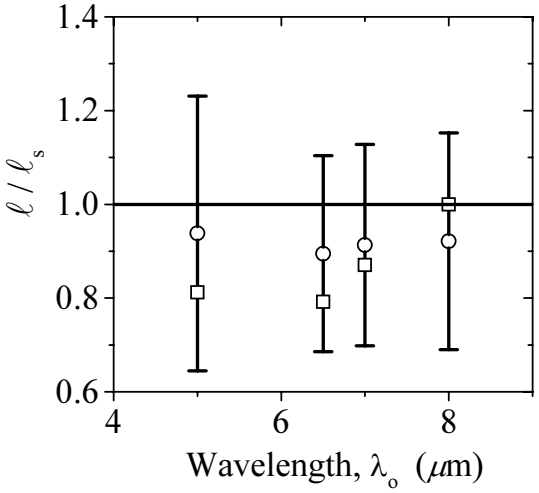

Figure 4.10:
Circles: transport mean free path in the Ge powder samples divided by the scattering mean free path, as a function of the wavelength. Squares: expected renormalization of ℓ due to interference assuming that the localization transition is at $\ell_c = \lambda_o/2\pi n_e$ and $n_e = 1.6$.

4.4 Time-resolved speckle interferometry

Time-resolved speckle interferometry was employed to study the dynamical properties of the transport of light in the Ge samples. This technique takes advantage of the picosecond pulse structure of the FEL, to map out the envelope of the transmitted pulse. As explained in section 2.2.5, multiple scattering gives rise to the broadening of a pulse transmitted through a random sample.

A schematic of the set-up used to perform this experiment is shown in Fig. 4.11. The sample was mounted in one of the arms of a Mach-Zehnder interferometer. The majority of the infrared power was focused weakly to a 1 mm spot at the sample. A small cone of the diffuse transmission far in angle ($\simeq 20^\circ$) from the coherently-transmitted beam propagated about 1 m, and was collected by a lens with a focal length of 10 mm onto a MCT detector. A variable iris was placed before this lens such that the detector collected light from a single speckle spot. A 10% reflecting beamsplitter, located before the sample, created the copy of the input pulse that was sent along the other arm of the interferometer. This reference pulse was directed down a variable optical delay line before it was combined co-linearly, on a second beamsplitter just before the iris, with the diffusively transmitted pulse. As the optical delay was scanned, the detector recorded the interferogram between the scattered pulse and the reference pulse. As in the other measurements, a reference detector was used to correct for fluctuations in the intensity of the FEL. Time-resolved measurements were made at two wavelengths, 4.5 and 8 μm.

The inset of Fig. 4.12, displays a small portion of a typical interferogram,

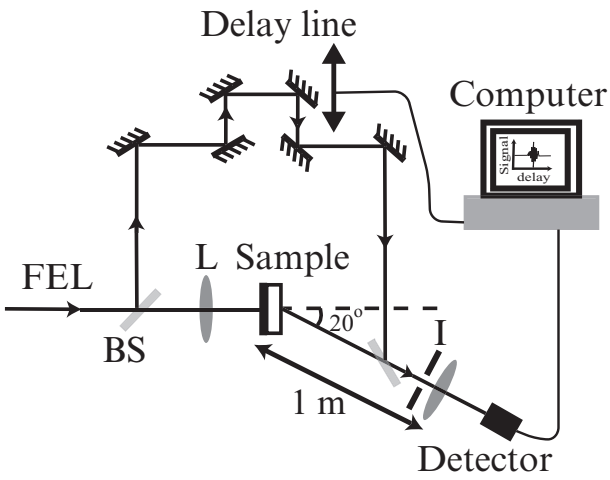

Figure 4.11: Schematic representation of the set-up used for the time-resolved measurements. The FEL light was sent into a Mach-Zender interferometer with the sample in one of its arms. The undistorted or reference pulse traveled along the other arm in which a delay line allowed the change of the optical path length. Both pulses were recombined at the exit of the interferometer. To avoid detecting the coherently-transmitted beam, the detector was placed at an angle of 20° with respect to the direction of the incident beam. BS: beam splitter, L: lens, I: iris.

taken at $\lambda_o = 4.5$ μm on a sample with a thickness of 17 μm. The oscillations at the optical frequency are clearly visible. In the analysis of these data we take advantage of the fact that oscillations in the interferogram have a well-defined carrier frequency. The data are analyzed further by taking the power spectrum of a narrow (200 fs) time slice of the interferogram, and integrating this spectrum in a narrow (5%) window in the vicinity of the carrier frequency.

Due to the coherent nature of the incoming light, the resulting interferogram of a given speckle has large amplitude and phase fluctuations as a function of optical delay. It is therefore necessary to average over several speckles for each sample thickness and at each wavelength. This process smoothes out the phase and amplitude fluctuations and leaves only the overall intensity envelope of the transmitted beam. The result of this averaging process is shown by the solid line in Fig. 4.12. As expected, the data exhibit a smooth rise time governed primarily by the incident pulse length, and a slower decay time due to multiple scattering. The dashed-dotted line in Fig. 4.12 is the shape of the incoming pulse, which was measured using the same set-up except with the sample replaced by a thin piece of weakly scattering paper. Note that this pulse is substantially shorter in duration (about 33%) than the transmitted pulse, with a sharper decay time.

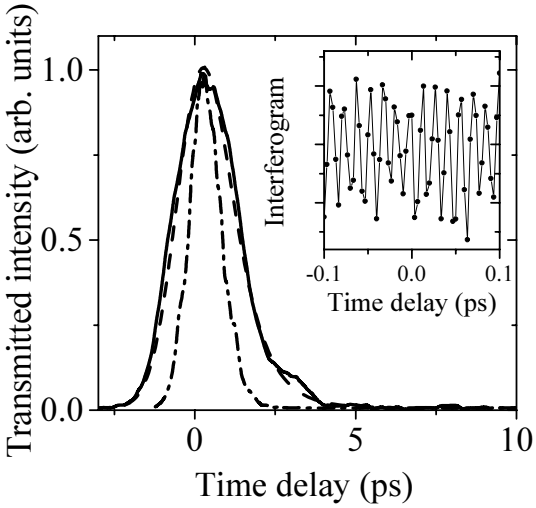

Figure 4.12: Transmitted intensity through a sample of Ge powder of thickness $L = 17\,\mu$m at $\lambda_o = 4.5\,\mu$m (solid line) as a function of the time delay introduced by the delay line of the Mach-Zender interferometer. The dashed line is a fit using classical diffusion theory convoluted with a Gaussian function, which takes into account the instrument response. The dashed-dotted line is the incident pulse. The maxima of both pulses have been normalized to the same time delay. The inset is a portion of the interferogram from which the transmitted intensity is reconstructed.

The maxima of the transmitted pulses in Fig. 4.12 have been normalized to the same time delay. Small set-up realignments between different samples, necessary to increase the signal-to-noise ratio of the interferogram, made it impossible to extract useful information from the delay time of the pulse. However, the diffusion constant can be obtained from the pulse broadening.

As we have seen in section 2.2.5, The long-time behaviour of a transmitted pulse through a multiple-scattering medium decays exponentially. Therefore, the time-resolved data are fitted with an exponential decay convoluted with a Gaussian function which takes into account the instrument response (dashed line in Fig. 4.12). The Gaussian width depends on the duration of the incoming pulse. The characteristic time constant of the decay is given by

$$\frac{1}{\Gamma} = D\left(\frac{\pi^2}{(L-\delta+z_{e_1}+z_{e_2})^2} + \frac{1}{L_a^2}\right) . \tag{4.5}$$

This expression may be used to obtain the diffusion constant D, with the values of L_a and z_{e_1} obtained from the static measurements (see section 4.3.2). The extrapolation length z_{e_2} is equal to 1.1ℓ, corresponding to the interface sample-CaF_2

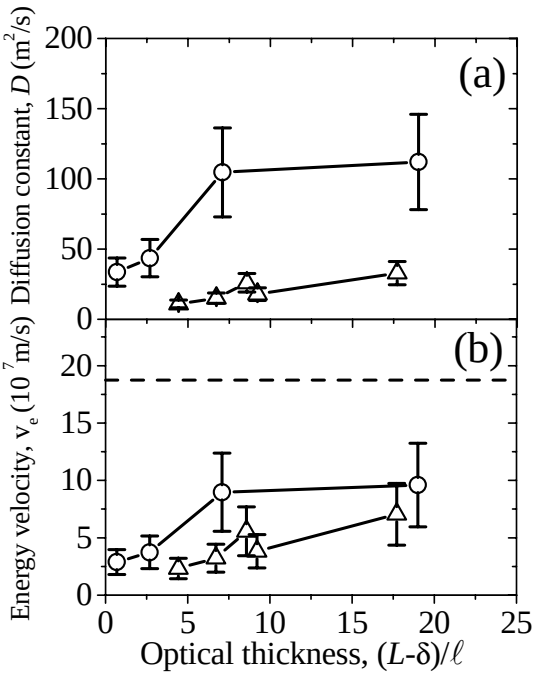

Figure 4.13:
(a) Diffusion constant of light at $\lambda_o = 4.5$ μm (triangles) and $\lambda_o = 8$ μm (circles) in samples of Ge powder as a function of the optical thickness of the sample. (b) Energy velocity in the same samples and at the same wavelengths. The dashed line is the phase velocity in an homogeneous medium with a refractive index equal to the effective refractive index of the Ge samples. The solid lines are guides to the eye.

substrate. For the time-resolved measurements the reflected light at the CaF_2-air interface does not need to be considered, since this reflected light is detected at later times. Due to the narrow spectral width of the pulse, dispersion in the sample top layer can be neglected. In Fig. 4.13 (a) the diffusion constant D is plotted as a function of the sample optical thickness $(L-\delta)/\ell$ at $\lambda_o = 4.5$ μm (triangles) and 8 μm (circles). As expected, the diffusion constant is smaller at the shorter λ_o, where, as we have seen in section 4.3, the scattering is stronger.

As can be appreciated in Fig. 4.13 (a), D is significantly reduced in samples thinner than $\simeq 7\ell$. Similar optical experiments carried out in TiO_2 powder [88] showed the same thickness dependence of D. Acoustic-frequency-correlation measurements in samples of glass beads immersed in water [89] are also consistent with a reduced D in thin samples. It is important to note that the values of D given in Fig. 4.13 (a) are obtained from the long-time behaviour of the transmitted pulse, thus when the diffusion approximation is expected to hold even for thin samples.

A possible explanation for the non-constant value of D is given in Ref. [89]. The transmitted intensity at long time in the thin samples is due to light that has mainly traveled along the x-y plane. The reduced dimensionality likely makes interference important, which is not taken into account by the diffusion equation. Therefore, the diffusion approach may underestimate D in thin samples.

λ_o (μm)	$k\ell_s$	ℓ (μm)	α ($10^{-3}\,\mu m^{-1}$)	α_{TL} ($10^{-2}\,\mu m^{-1}$)	D (m^2/s)	v_e ($10^7 m/s$)
8	4.7 ± 0.2	3.5 ± 0.5	4.9 ± 0.9	9.1 ± 0.8	$\simeq 100$	$\simeq 9$

Table 4.1: Scattering properties of Ge powder at $\lambda_o = 8\ \mu$m. Localization parameter $k\ell_s$, transport mean free path ℓ, absorption coefficient in the sample bulk α, absorption coefficient in top layer of the samples α_{TL}, diffusion constant D, and energy velocity v_e.

Using the expression $D = v_e\ell/3$ and the values of ℓ obtained from the analysis of the total transmission and reflection, the energy velocity v_e is acquired. It is well known that the energy velocity may be significantly lower than the phase and group velocities due to scattering resonances [24, 25]. The values of the energy velocity in the samples of Ge powder are displayed in Fig. 4.13 (b) versus the optical thickness. The phase velocity in a medium with $n_e = 1.6$ is plotted in the same figure with a dashed line. The large difference between the energy and phase velocities is clear: more than a factor 2 at $\lambda_o = 8$ and 3 at 4.5 μm for samples thicker than 7ℓ.

The scattering properties of the Ge samples at $\lambda_o = 8\ \mu$m, obtained from the static and dynamic measurements, are summarized in Table 4.1.

4.5 Photoacoustic spectroscopy

The photoacoustic effect was discovered more than 120 years ago [140]. Only in the last quarter of the 20th century, the use of photoacoustic spectroscopy was extended to study the optical absorption of solids [141].

Usually, in a photoacoustic experiment intensity-modulated light impinges on a sample contained in a cell. Light is absorbed by the sample and generates a photoacoustic signal (PA signal) that is detected with a transducer. From the analysis of the PA signal information about the absorption in the sample is obtained.

The PA signal is formed by two contributions: the thermal term and the pressure term [142]. The thermal term arises from the heat transferred from the sample to the buffer gas contained in the cell within a length given by the thermal diffusion length. This gas expands and contracts responding to the periodic heating of the sample, acting as piston on the rest of the gas in the cell. The pressure term is due to the expansion and contraction of the sample generated by the periodic heating.

In heterogeneous media, like powders and porous materials, the PA signal is stronger than in homogeneous media. This enhanced PA signal is due to the thermal expansion of the interstitial gas [143]. For highly-porous materials the pressure term can dominate the PA signal.

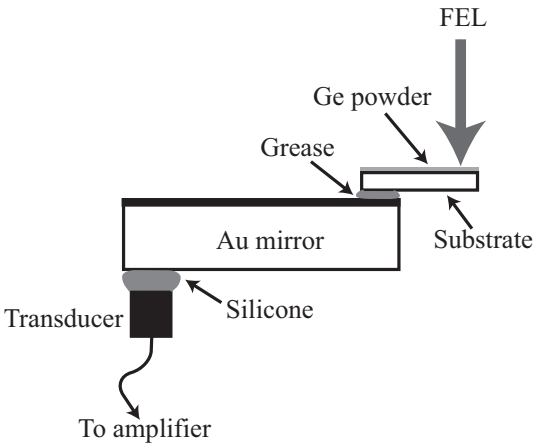

Figure 4.14:
Schematic representation of the set-up used to measure the photoacoustic signal in samples of Ge powder. See text for explanation.

In our experiments, we used the FEL macropulse to generate high-frequency PA signals. The photoacoustic set-up was not the standard one described above. A variation of the so-called solid-transducer technique [144] was used. The set-up used for these measurements is depicted in Fig. 4.14. The CaF_2 substrate on which the Ge powder lies, was overhanging the edge of a gold mirror, and it was hold with grease. The grease also insured a good acoustic coupling between the CaF_2 substrate and the mirror. At the opposite side of the mirror a piezoelectric transducer with bandwidth of 4 MHz was glued with silicone. The FEL beam was incident on the unsupported portion of the sample. In this way, the PA signal generated by the transmitted light through the sample on the mirror was minimized. Only in thick samples this non-desired contribution to the PA signal was negligible. The energy of the FEL macropulse absorbed by the Ge powder generated a waveform that was detected by the transducer, amplified and collected by a computer.

A typical photoacoustic waveform is shown in Fig. 4.15. Because of the geometry of the set-up, the waveform is very complicated. The PA signal is defined by calculating the square root of the power spectrum of the waveform and integrating the result between 0.7 and 1 MHz. This is the frequency range in which the vast majority of the acoustic energy lies. The wavelength dependence of the integrated PA signal is plotted in Fig. 4.16 with open circles. The line is a guide to the eye.

In the thermoacoustic regime, in which the laser pulse does not damage the sample, the amplitude of the PA signal should depend linearly on the absorbed energy [145]. This dependence was checked by measuring the PA signal at different FEL intensities.

The fraction of absorbed energy by the sample or the total absorption is plotted in Fig. 4.16 with solid squares. This absorption is obtained from the measurements

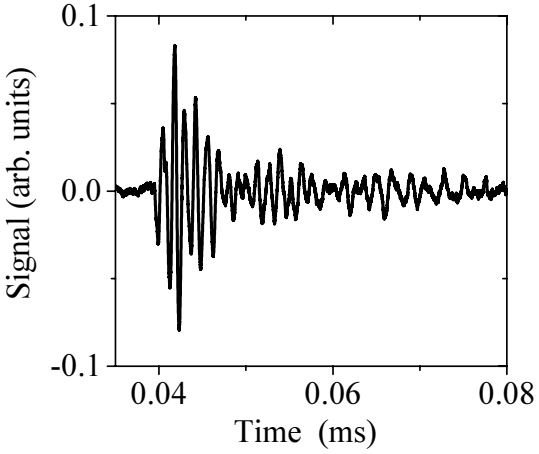

Figure 4.15:
Photoacoustic waveform generated at $\lambda_o = 7$ μm by a sample of Ge powder with a thickness of 73.2 μm.

of the total transmission and reflection (see section 4.3.2), and considering the energy conservation (Eq.(2.39)).

As can be appreciated in Fig. 4.16, the photoacoustic spectrum is similar to the total absorption of the sample. In both spectra the two absorption bands at 6 and 6.9 μm are clear. At the time the measurements were done, we did not have a good reference, i.e., 100 % absorption, for the photoacoustic measurements. Therefore, we could not obtain the absolute or total absorption of the Ge samples. Nonetheless, we have demonstrated that a simple photoacoustic set-up, as that of Fig. 4.14, can be used to study the optical absorption in strongly-scattering samples.

Figure 4.16:
Photoacoustic spectrum of Ge powder (open circles). The squares are the total absorption of the same sample obtained from the measurements of the total transmission and reflection. The lines are guides to the eye.

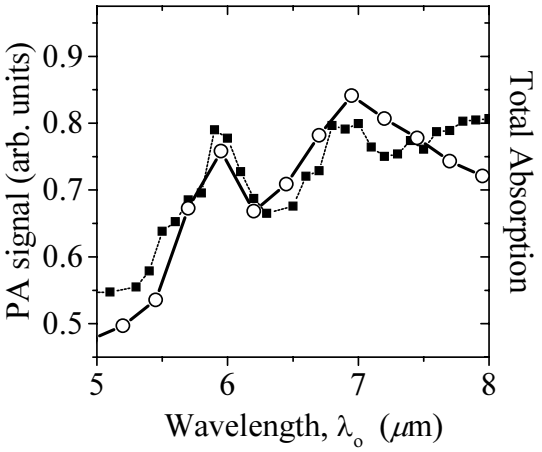

5

Porous GaP: formation and optical properties

In this chapter it is shown that anodic etching of n-type gallium phosphide (GaP) produces a random-porous structure. This structure scatters light strongly. The optical set-ups used to study porous GaP (enhanced backscattering and angular-resolved transmission) are described in section 5.2. In section 5.3 the current-potential characteristics of GaP and the formation of the porous layer are discussed. As shown in section 5.4, anodic etching does not introduce any measurable optical absorption. Anodic etching leaves a thin top layer ($\simeq$ 200 nm) of nearly bulk GaP. This layer produces strong internal reflection and complicates the analysis of the EBS measurements. As explained in section 5.5, this layer can be removed by means of photochemical etching. The pore size, inter-pore distance, and porosity depend strongly on the doping concentration and on the applied potential during etching (section 5.6). The biggest pores (with an average radius $\simeq$ 95 nm) and the strongest scattering samples ($k\ell \simeq 3.5$ at $\lambda_o = 633$ nm) are made from low-doped GaP ($N = 5 \times 10^{17}\text{cm}^{-3}$) etched at the highest possible potential. To further increase the scattering strength of porous GaP, the pore diameter was augmented by means of chemical etching. As shown in section 5.7 the optical transmission can be measured during etching. Surprisingly the width of the EBS cone of the strongest scattering samples is reduced upon chemical etching.

5.1 Introduction

In chapters 3 and 4 we have seen that powders of micron-sized particles of Si and Ge strongly scatter light. Although the results with these samples are very close to the localization transition ($k\ell_s \simeq 3$), significant absorption is introduced during the powder preparation.

An alternative to powders are porous materials. Semiconductors can be made

porous by electrochemical or anodic etching [146]. An example of a porous structure formed in gallium phosphide (GaP) is shown in Fig. 1.2 (b). The high refractive index of GaP ($n = 3.3$) and its band gap in the visible $\lambda_{gap} = 0.55$ μm [147] make this semiconductor very interesting for light-localization experiments. Moreover, anodic etching of GaP leads to a highly-isotropic porous structure, necessary for 3D localization. These isotropic structures are in contrast to most other semiconductors in which etching occurs along preferential crystallographic directions [146, 148, 149].

A first study of the scattering properties of porous GaP was done by Schuurmans *et al.* [79, 80]. Two different types of samples were studied: a) anodically-etched GaP (A-GaP) and b) photo-assisted anodically-etched GaP (PA-GaP). The GaP wafers used were (100)-oriented, n-type, with a doping concentration of $N = 2 \times 10^{17}\text{cm}^{-3}$. All samples were etched at a potential of 15 V. A disordered network of pores was formed with an average pore radius of 45 nm for A-GaP and 65 nm for PA-GaP. Strong scattering of light without optical absorption was measured in both types of porous GaP at the wavelengths of the experiments (633, 685 and 780 nm). The strongest scattering ($k\ell_s \simeq 3.5$) was found for PA-GaP at $\lambda_o = 633$ nm. The EBS measurements on PA-GaP showed a rounding close to the backscattered direction due to the onset of localization [79, 129].

The porous structure and, therefore, the optical properties of anodically-etched semiconductors depend on the etching conditions (doping concentration [150, 151], etching potential [151, 152], temperature [153], electrolyte [150, 152], magnetic field [154]). We decided to investigate routes to increase the scattering strength of porous GaP. Since the average pore (or scatterer) radius of the GaP samples in Refs. [79, 80] is small compared to the wavelength, it was expected that the scattering strength could be increased by making bigger pores.

We have investigated the pore formation and the scattering strength as a function of the doping concentration and the etching potential. The average pore radius and inter-pore distance depend strongly on both parameters. Photo-assisted electrochemical etching was not used in the present work, all samples being A-GaP.

Bigger pores can be formed in low-doped GaP etched at the highest possible potential. Although the average pore radius in these samples is $\simeq 95$ nm, the scattering strength (obtained from the width of the EBS cone) was not larger than that of PA-GaP. The pore radii were further increased by chemical etching, which in the strongest scattering samples leads to a reduction of the EBS-cone width. According to classical [123] and localization [129] theories a decrease of the width of the EBS cone is due to a reduction of the scattering strength. This reduction of the EBS-cone width upon chemical etching is a surprising result that needs further investigation.

5.2 Optical experimental techniques

The inverse of the localization parameter $k\ell_s$ characterizes the scattering strength of a random medium (section 1.2). Due to the large optical thickness of the porous GaP samples, measurements of the coherent transmission (from which ℓ_s can be derived) are difficult. Therefore, the scattering strength in this chapter will be defined as $(k\ell)^{-1}$. Enhanced-backscattering measurements were used to obtain the transport mean free path ℓ (see section 2.3 on page 38).

The effective refractive index n_e of the porous GaP samples was acquired by measuring the angular-resolved transmission [97, 155] (see section 2.2.3 on page 32). With the value of n_e it is possible to correct the EBS measurements for internal reflection (section 2.2.2), and to obtain the wave vector in the porous structure $k = 2\pi n_e/\lambda_o$.

The enhanced-backscattering cones were recorded using the off-centered technique. This technique is described in Refs. [87, 156], and will not be repeated here. Relevant for the measurements presented in this chapter is that the angular resolution of the set-up is $\simeq 0.15$ mrad. A He:Ne laser ($\lambda_o = 633$ nm) was the light source. Linearly-polarized light illuminated the sample. The detection was in the polarization-conserving channel. For linearly-polarized radiation the single-scattered light is also detected. Single scattering does not contribute to the enhanced backscattering, but increases the diffuse background. This increased background causes an enhancement factor smaller than two. Light that is specularly reflected on the sample also reduces the enhancement factor [124]. The reduction of the backscattering enhancement by single-scattered light and specular reflection is considered in the analysis of the measurements.

The set-up used to measure the angular-resolved transmission is schematically represented in Fig. 5.1. The intensity of a He:Ne laser was modulated with a chopper at a frequency of 1 Khz. This beam, with a diameter of $\simeq 4$ mm, illuminated the sample. A lens with a focal length of 10 cm, placed at 90 cm from the sample, collected the transmitted light onto a Si photodiode. The signal from the detector was amplified with a lock-in amplifier, and recorded by a computer. The detector and collection optics could be rotated around the sample by means of a stepper motor controlled by the computer, with a minimum step size of 9×10^{-2} mrad. By placing a polarizer between the sample and the detector, the parallel p- and perpendicular s- (to the plane of incidence) polarization components of the angular-resolved transmission were also measured.

To average out speckle, six measurements were done for each sample and for each polarization. The sample was moved slightly between the measurements. The results presented in section 5.5 are the average of these six measurements.

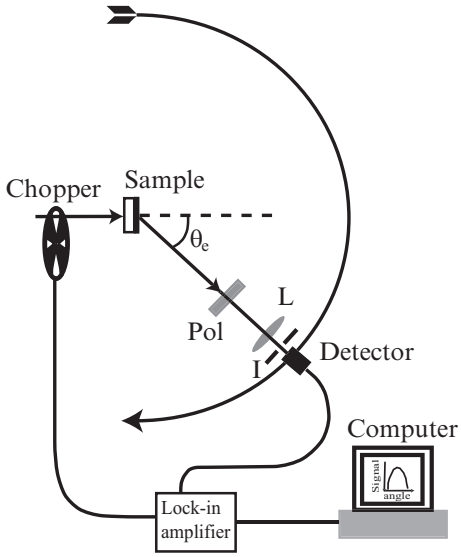

Figure 5.1:
Schematic representation of the set-up used to measure the angular-resolved transmission of porous GaP. The polarizer Pol, lens L, iris I, and detector can be rotated around the sample by means of a computer controlled stepper motor (not plotted).

5.3 Pore formation by anodic etching

For anodic etching, a piece of GaP wafer with dimensions of 1×1 cm was glued to a copper plate with silver epoxy. The copper plate was covered with a Teflon sticker to prevent it from chemically dissolving in the electrolyte. The GaP piece was also covered with Teflon, leaving a circular opening with a diameter of 5.5 mm (see Fig. 5.7 (b) on page 89). This was the only GaP surface exposed to the electrolyte, and acted as working electrode (anode). As counter electrode (cathode) a platinum wire was used. All the potentials were measured against a saturated calomel electrode (SCE). The electrochemical cell contained an aqueous 0.5M H_2SO_4 solution. All the etching experiments were done at room temperature.

Commercially-available GaP wafers,[1] doped with sulfur and with different doping concentrations $N = 5 \pm 1, 6, 7$ and $15 \pm 5 \times 10^{17}\text{cm}^{-3}$ were used. The doping concentrations were specified by the GaP suppliers. The thickness of the wafers is 300 μm and their surface (100)-oriented.

An n-type GaP electrode does not dissolve anodically in the dark at potentials below $\simeq 3\,V$. Valence-band holes are required for the dissolution reaction

$$(\text{GaP})_\text{n} + 6\text{h}^+ \rightarrow (\text{GaP})_{\text{n}-1} + \text{Ga}\,(\text{III}) + \text{P}\,(\text{III})\,. \tag{5.1}$$

When a positive potential V is applied, the electrochemical potential of the electrode decreases, which induces a bending of the valence and conduction bands

[1] Atomergic Chemetals, Ramet Ltd., and Philips.

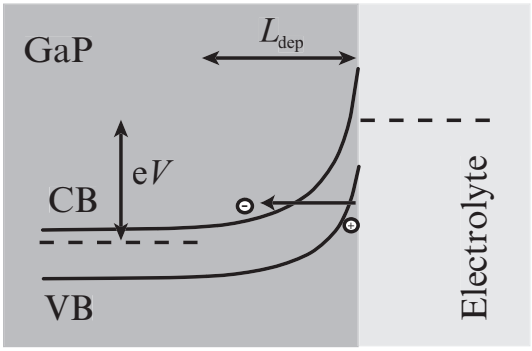

Figure 5.2:
Interface between GaP and the electrolyte at a potential V higher than the breakdown potential. Electrons in the depletion layer L_{dep} may tunnel from the valence band (VB) to the conduction band (CB). The holes are used for the dissolution of the semiconductor at the interface.

close to the semiconductor-electrolyte interface (Fig. 5.2). The region where the bending takes place is called the depletion layer and its spatial extent L_{dep} is given by [157]

$$L_{dep} = \left(\frac{2\varepsilon\varepsilon_o}{eN}(V - V_{fb}) \right)^{1/2}, \tag{5.2}$$

where $\varepsilon = 11$ is the dielectric constant of GaP [147], ε_o is the vacuum permittivity, e is the electron charge, N is the donor concentration and V_{fb} is the flat-band potential or the potential at which the bands are flat. For a given semiconductor electrode, the flat-band potential depends mainly on the nature of the electrolyte. In our experiments (aqueous 0.5M H_2SO_4 solution) the flat band potential is $\simeq -1.2$ V [158].

When the anode potential is strongly positive, electrons can tunnel from the valence to the conduction band (see Fig. 5.2), a process known as breakdown. The holes generated in this way cause etching according to reaction (5.1), and give rise to a porous structure.

5.3.1 Current-potential characteristics

The current density-potential characteristics ($I-V$ curves) were measured with an EG&G PAR 273A potentiostat at scanning rates of typically 50 mV/s. When potentials higher than 10 V (inaccessible with the potentiostat) were needed, one or more 9 V batteries were connected in series with the working electrode.

Figure 5.3 shows a typical $I-V$ curve of GaP ($N = 6 \times 10^{17}\text{cm}^{-3}$). The direction of the scan is marked with arrows. Three distinctive regions are indicated in the Fig. 5.3. At low potential (region I) the band bending is too small to allow interband tunneling. The current density I in this region is low and the semiconductor behaves as a reverse-biased diode.

Above the breakdown potential (region II in Fig. 5.3), the current density increases strongly with V due to the anodic dissolution produced by the dielectric breakdown of GaP. The current density reaches a maximum value at the potential $V_{\max}$. Since at low scanning rates reaction (5.1) occurs under steady-state conditions, $V_{\max}$ depends weakly on the scanning rate.

Besides the weak dependence of $V_{\max}$ on the scanning rate, a strong dependence on the doping concentration was found. This dependence is displayed in Fig. 5.4. The values of $V_{\max}$ in Fig. 5.4 were measured at a scanning rate low enough to allow steady-state dissolution.

After reaching the maximum, I rapidly decreases to a low value (region III in Fig. 5.3), showing only a weak dependence on the potential. This decrease of I is characteristic of electrode passivation, due to the formation of an oxide layer. Although we have not studied the characteristics of the passive layer, it presumably forms when the etching rate at the pores front reaches the critical value at which reaction (5.1) changes from being limited by breakdown charge transfer to being limited by the oxide formation.

As the voltage is reduced in the return scan, a maximum in the current density also appears but at a lower voltage than in the forward scan. The passive layer is chemically dissolved in a slow reaction and the current flows again.

The formation and dissolution of the passivation layer can be used to fabricate free-standing membranes of porous GaP and multilayer GaP structures [95]. These structures can be used as Bragg reflectors and as sieves for biomolecules.

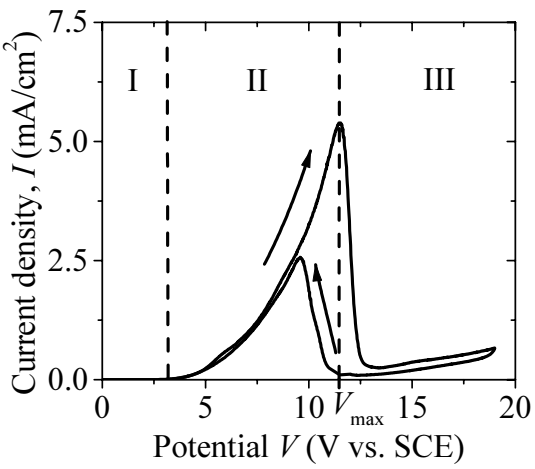

Figure 5.3:
Current density versus potential (given with respect to a saturated calomel electrode) of GaP with a doping concentration $N = 6 \times 10^{17} cm^{-3}$ measured at a scanning rate of 50 mV/s. At low potentials (region I) no current flows indicating that no etching occurs. In region II etching takes place. In region III a passive layer is formed and the current density is low. The arrows indicate the scanning direction.

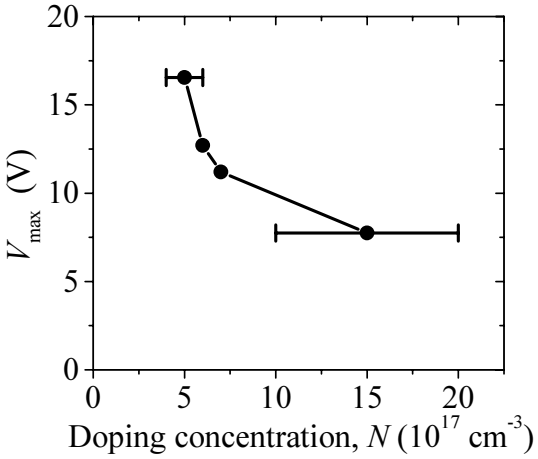

Figure 5.4:
Potential of maximum anodic current as a function of the GaP doping concentration. The solid line is a guide to the eye.

5.3.2 Formation of porous layers

Anodic etching at a fixed potential (in region II of Fig. 5.3) produces a homogeneous layer of porous GaP. In this section the formation of the porous layer is explained.

Etching starts at specific sites on the surface. Initial pits are formed where surface defects are present. Surface defects may lead to a local enhancement of the electric field helping the hole generation [159]. The pits can be clearly seen in the SEM photograph (a) of Fig. 5.5. This image is of a cleaved cross section of a porous GaP sample, in which etching was stopped at the initial stage.

From an initial pit, a pore is formed; branching of the pores occurs, with a hemispherical expansion of the porous region. The porous domains originated at different surface defects can be seen in Figs. 5.5 (a) and (b). The SEM photograph of Fig. 5.5 (b) corresponds to a side view of a porous structure. At the end of this section a possible explanation for the pore branching is given.

The etching of GaP occurs only at the pore tips (see section 5.6) where the surface curvature is higher and the electric field stronger. It is important to note that the top surface of the sample consists of a thin layer ($\simeq$ 200 nm) of GaP with only a few pits. The porous structure extends underneath this layer.

Figure 5.6 displays the current density I as a function of the etching time of a GaP sample ($N = 6 \times 10^{17}$cm^{-3}, etched at 11.5 V). The increase of I at the beginning is due to the increase of the surface area of the front of the porous region. Etching of the sample shown in Figure 5.5 (a) was stopped while the current density was increasing.

Once the porous regions initiated at different pits meet, the surface of the front of the porous structure is slightly reduced. As can be seen in Fig. 5.6, this reduction

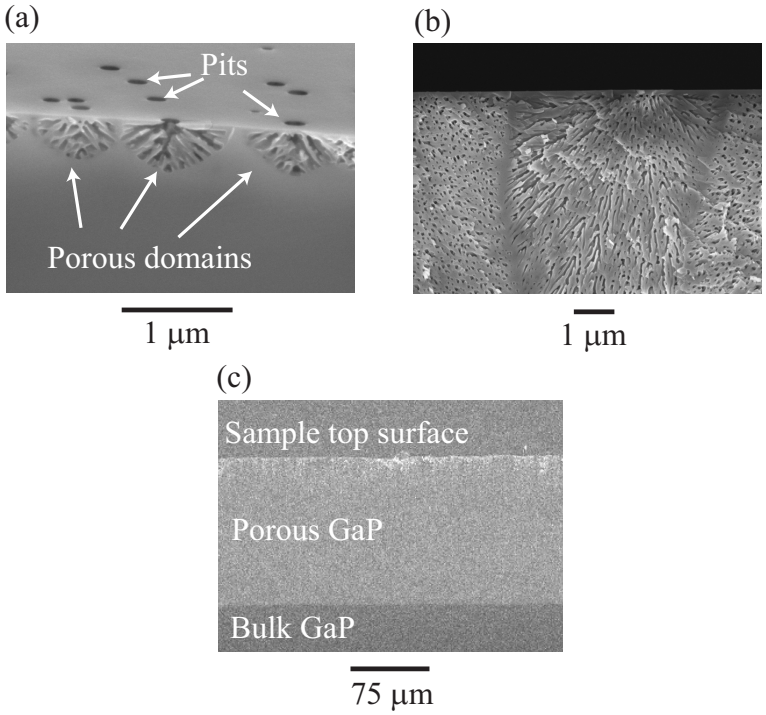

Figure 5.5: Electron-microscope (SEM) photographs of porous GaP. (a) cleaved cross section of a sample in which etching was stopped at its initial stage, i.e., when the current density was still increasing (see Fig. 5.6). (b) side view of a porous structure. (c) cleaved cross section of a layer of porous GaP with a thickness of 203 μm.

of the porous front produces a small decrease of I.

Finally, the current density becomes constant indicating that a layer of porous GaP grows downwards in an uniform way. The thickness of the layer can be easily varied from a few microns to the whole thickness of the wafer. The photograph (c) in Fig. 5.5 is a cleaved cross section of a porous-GaP layer with a thickness of 203 μm.

A sample of porous GaP is schematically represented in Fig. 5.7. Figure 5.7 (a) is a side view of the sample. The dark region represents the porous structure, and the light one the non-etched GaP wafer. Also the thin top layer of nearly homogeneous GaP with a thickness of $\simeq 200$ nm is plotted. In Fig. 5.7 (b) a top view of the sample is displayed. The non-etched region was covered with a Teflon mask.

Anodic etching of GaP differs from other semiconductors (such as Si, InP,

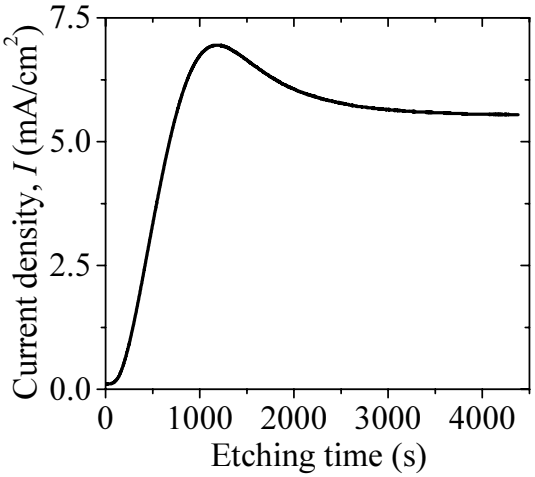

Figure 5.6:
Current density versus etching time of GaP ($N = 6 \times 10^{17}$cm^{-3}) etched at V = 11.5 V.

GaAs [146]) in that isotropic structures of macropores are formed with GaP. The pore branching that leads to isotropic etching in GaP is probably due to the formation of the passive layer. The etch rate is higher at the pore tips due to the enhanced electric field caused by the radius of curvature. Since a passive layer presumably forms when the etching rate reaches the critical value at which the reaction (5.1) is limited by oxide formation, the pore tip can be locally passivated. Etching proceeds close to the pore tip, causing the branching of the pore. This process is summarized in Fig. 5.8, where (a) represents a pore with the tip passivated (black region), and (b) is the pore after the branching.

Figure 5.7:
(a) Schematic side view of a porous GaP sample. The non-etched GaP wafer is represented by the light region. The dark region is the porous structure, which extends under a thin ($\simeq 0.2$ μm) layer of nearly homogeneous GaP. (b) is an top view of a porous GaP sample with a diameter of 5.5 mm. The non-etched region was covered with Teflon sticker during etching.

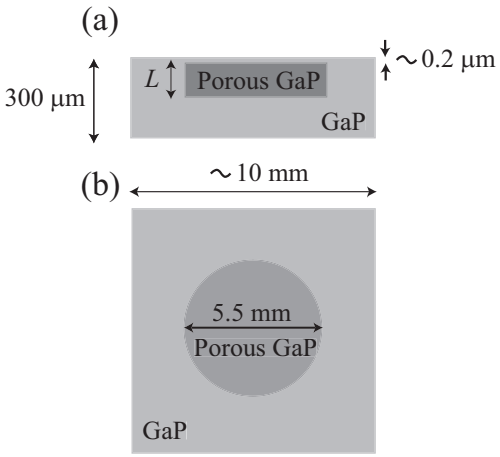

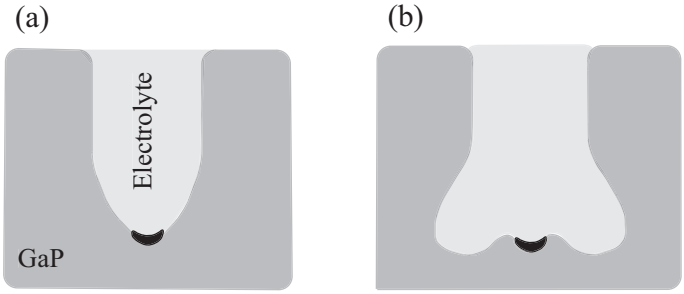

Figure 5.8: Schematic representation of the pore branching. Figure (a) represents a pore. The strongest electric field is at pore tip due to its radius of curvature. The etching rate is higher in this region and it can be passivated. This local passivation is represented by the black area. As displayed in (b), the etching proceeds in the non-passive region, producing the branching of the pore.

5.4 Optical absorption in anodically-etched GaP

In Fig. 5.9 a measurement of the EBS intensity at small angles is displayed. This is a measurement for a layer of porous GaP ($N = 6 \times 10^{17}\text{cm}^{-3}$, etched at 11.5 V) with a thickness of 203 μm.

As a result of optical absorption and the finite thickness of the sample, long paths do not contribute to the enhanced backscattering (section 2.3), which causes a rounding of the backscattered intensity [125, 126]. Localization also gives rise to a similar rounding [76, 79, 129].

For a sample with a thickness of 203 μm, the rounding in the absence of absorption or localization effects is expected to be $\Delta\theta = 0.5$ mrad [79]. The rounding

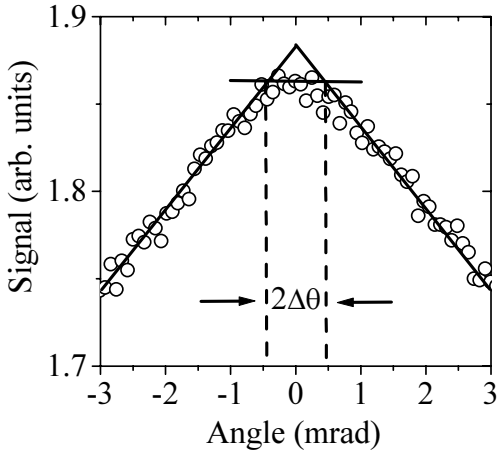

Figure 5.9: Detailed measurement of the EBS intensity at small angles of a sample of porous GaP ($N = 6 \times 10^{17}$ cm^{-3}, etched at 11.5 V) with a thickness $L =$ 203 μm. The rounding of the EBS is represented by $2\Delta\theta$.

in the measurement (Fig. 5.9) is $\Delta\theta = 0.45 \pm 0.1$ in good agreement with the value expected for a non-absorbing sample given the experimental accuracy. The absorption length in this sample is thus $L_a > 200\ \mu$m, which means that anodic etching virtually does not introduce any optical absorption. This absence of absorption is consistent with previous total-transmission measurements [80].

5.5 Removal of the top layer by photochemical etching

Anodic etching produces a porous layer. As mentioned in section 5.3.2, at the top surface of the sample there is a thin layer ($\simeq 200$ nm) of bulk GaP with only a few pits where the pore formation is initiated. The thickness of the top layer and the separation between pits depend on the surface polishing. The presence of this layer can be clearly observed with the naked eye, since it produces a strong specular reflection characteristic of a homogeneous material.

As we have seen in the preceding chapter (where the Ge samples have a top layer formed by small particles), a top layer with optical properties different from those of the sample bulk complicates the analysis of the optical experiments. Therefore, it is convenient to remove the layer on top of the porous structure.

Several methods can be used to remove this layer. Chemical polishing, using an aqueous Br_2 solution, has been successfully employed [160]. However, with this method it is difficult to control the exact amount of material that is removed. A different approach is to increase the density of surface defects before anodic etching [161]. The separation between pits will be smaller and consequently the surface of the etched GaP samples will be also porous.

We have used a different method to remove the top layer, i.e., photochemical etching. The samples were first anodically etched as described previously. They were then immersed in a aqueous solution of 15 ml of 0.5 M H_2SO_4 and 3 ml 30% H_2O_2. The samples were uniformly illuminated with the expanded beam of an argon laser ($\lambda_o = 460$ nm) incident at 45° with respect to the normal of the sample surface. The absorption length of bulk GaP at $\lambda_o = 460$ nm is $\simeq 3.5\ \mu$m [147]. Due to scattering in porous GaP, the absorption length is reduced to the order of the transport mean free path. The light of the argon laser is thus mainly absorbed by the top layer, where electron-hole pairs are created. The electrons are used to reduce H_2O_2, to give an OH^- ion and an $OH^\bullet$ radical [162]

$$H_2O_2 + e^- \rightarrow OH^- + OH^\bullet\ . \tag{5.3}$$

This radical is very strongly oxidizing and can be reduced by "hole injection" into

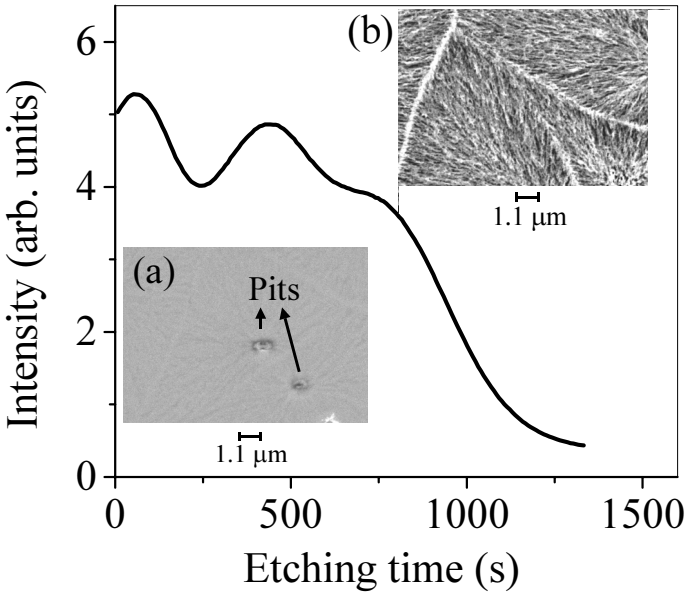

Figure 5.10: Specular reflection ($\lambda_o = 460$ nm) of a sample of porous GaP as a function of the photochemical-etching time. The SEM photographs are of the top of a sample before (a) and after (b) photochemical etching.

the valence band

$$OH^{\bullet} \rightarrow OH^{-} + h^{+} \, . \tag{5.4}$$

Both, the photogenerated and injected holes, are used for the dissolution of GaP (reaction (5.1)). No potential is applied during the photochemical etching, and the h^+ are generated (and the photochemical etching occurs) only where the light from the argon laser is absorbed.

The specular reflection was measured during photochemical etching. The specular reflection of a sample ($N = 6 \times 10^{17}\text{cm}^{-3}$, anodically etched at a 11.5 V) is plotted in Fig. 5.10 as a function of the photochemical-etching time. This reflection oscillates before it vanishes. The oscillations are due to wave interference of the light reflected at the air-top layer and at the top layer-porous GaP interfaces. As the thickness of the top layer is reduced by photochemical etching the interference changes from constructive to destructive, to constructive again. Finally the top layer is etched away and the specular reflection vanishes. The photochemical etching was at this point stopped. The low signal after 1350 s of photochemical etching in the example of Fig. 5.10 corresponds to the diffuse reflection.

The SEM photographs displayed in Fig. 5.10 are of the top surface of the sam-

ple before (a) and after (b) photochemical etching. Before photochemical etching an uniform structure with some of the initial pits can be seen. The porous structure is clearly visible after photochemical etching of the top layer. The white lines are the separation between porous domains generated at different pits.

The effect of removing the top layer on the optical experiments becomes evident in a measurement of the angular-resolved transmission. The set-up employed for these measurements is described in section 5.2. The sample was illuminated through its back side, i.e., the non-etched side of the GaP wafer (see Fig. 5.7 (a)). The angular distribution of the transmitted light through the porous-air interface was thus measured.

In Fig. 5.11 this angular distribution, normalized by the cosine of the angle at which the light leaves the sample $\mu_e = \cos\theta_e$, is plotted versus μ_e. Figure 5.11 (a) shows the measurements of a porous GaP sample with a doping concentration $N = 7 \times 10^{17}\text{cm}^{-3}$ etched at 10 V. The measurements of Fig. 5.11 (b) are of the same sample after the photochemical etching of the top layer. The squares correspond to the measurements of the unpolarized transmission, the circles to p-polarized and the triangles to s-polarized transmission.

The solid lines in Fig. 5.11 are fits to the measurements using Eq. (2.28), where the polarization of the detected intensity is included in the Fresnel's reflection co-

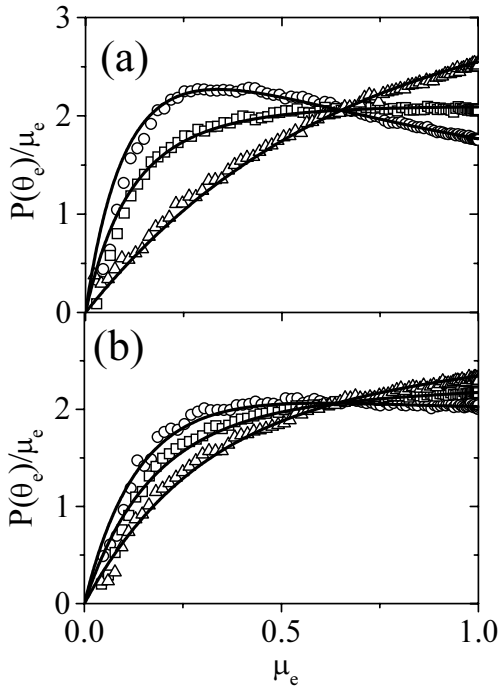

Figure 5.11: Angular distribution of the transmitted light through porous GaP, normalized by the cosine of the angle at which the light leaves the sample $\mu_e = \cos\theta_e$, plotted versus μ_e. The squares, triangles and circles correspond to unpolarized, s- and p-polarized light respectively. (a) corresponds to a $N = 7 \times 10^{17}\text{cm}^{-3}$ sample etched at 10 V. The measurements shown in (b) are of the same sample after photochemical etching of the top layer. The solid lines are fits to the measurements.

efficient. These coefficients depend solely on the refractive index contrast at the sample interface and on the angle θ_e. Therefore, the effective refractive index of the sample n_e is the only free parameter of the fits. From the fits n_e is found to be 2.8 ± 0.2 for the sample with the top layer and 1.6 ± 0.1 for the photochemically-etched sample.

The validity of Eq. (2.28) holds for a multiple-scattering medium with the same effective refractive index n_e in the bulk and at the boundary, i.e., samples with the same porous structure in the bulk and at the boundary. Therefore, the effect of the top layer has not been included in the fits of Fig. 5.11 (a), and the value of $n_e = 2.8 \pm 0.2$ does not represent the effective refractive index of the porous structure. The angular-resolved transmission of this sample is dominated by the reflection at the top layer-air interface, giving rise to an overestimation of n_e if this reflection is not properly taken into account.

Internal reflection causes a narrowing of the EBS cone (see section 2.3 on page 38). Therefore, the removal of the top layer is important for a correct interpretation of the EBS measurements presented in the next sections.

5.6 Scattering strength versus doping concentration and etching potential

In this section it is shown that the porous structure of GaP (average pore radius r, inter-pore distance d_p, and porosity ϕ) depends on the doping concentration N and on the applied potential V during etching.

The scattering mean free path in a disordered scattering medium is, to a first approximation, given by $\ell_s = 1/\rho\sigma_s$ (sections 1.2 and 2.1); where ρ is the density of scatterers and σ_s is the scattering cross section. The scattering cross section depends on the radius of the scatterers relative to the wavelength (see Fig. 1.1 on page 11). The strongest scattering is achieved when the size of the scatterers is of the order of the wavelength, i.e., in the Mie scattering regime.

Since the density of scatterers is determined by the inter-pore distance and the size of the pores, and the scattering cross section depends on the pore radius, the dependence of r and d_p on the doping concentration and the etching potential should strongly affect the scattering strength of porous GaP. This dependence of the scattering strength is demonstrated in this section with EBS measurements.

In Refs. [148, 152] it is shown that the inter-pore distance in porous n-type Si is determined by the extent of the depletion layer L_{dep}, and this distance is always smaller than $2L_{dep}$. If the depletion layers of adjacent pores overlap, the electric field is reduced and the etching stops. Dissolution can only occur in regions where the field is enhanced. These regions are the pore tips were the enhancement of

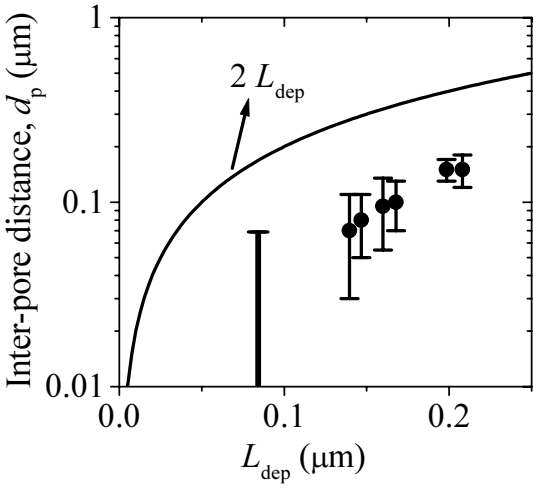

Figure 5.12:
Inter-pore distance in porous GaP versus the extent of the depletion layer L_{dep}. The solid line represents $2L_{dep}$.

the field is due to the radius of curvature. In Fig 5.12 the inter-pore distance of porous GaP is plotted as a function of L_{dep} (given by Eq. (5.2)). The inter-pore distance is defined as the average distance between adjacent pore walls and it was estimated with a marked gauge from high magnification SEM images. The solid line in Fig. 5.12 represents $2L_{dep}$. Similar to n-type Si, the inter-pore distance in porous GaP is always smaller than $2L_{dep}$, and d_p increases as L_{dep} increases.

The mechanism of the pore formation on n-type Si is discussed in Ref. [152]. The ratio of the radius of curvature at the pore tip to the width of the depletion layer determines the field strength. A thin depletion layer, i.e., a high N or a low V above the breakdown potential (see Eq. (5.2)), requires a smaller radius of curvature than the one when L_{dep} is large to produce the same field strength. It is reasonable to assume that a pore is etched when the electric field reaches a certain critical value. This value is thus reached with a small radius of curvature at the pore tip if L_{dep} is thin. If we assume that the pore tip is hemispherical, the radius of curvature at the pore tip determines the pore radius.

The average pore radius of several samples with different doping concentrations and etched at different potentials are listed in Table 5.1. The corresponding values of L_{dep} are also listed. It is clear from Table 5.1 that, as in the case of anodically-etched n-type Si, bigger pores are in general formed in GaP if the extent of the depletion layer is larger.

Note that, in contrast to GaP, a passive layer is not formed in Si. This passive layer and the pore branching may also influence the pore radii.

To summarize the results of Fig. 5.12 and Table 5.1: bigger and more widely-spaced pores are formed at large values of L_{dep}. Since L_{dep} depends on the doping

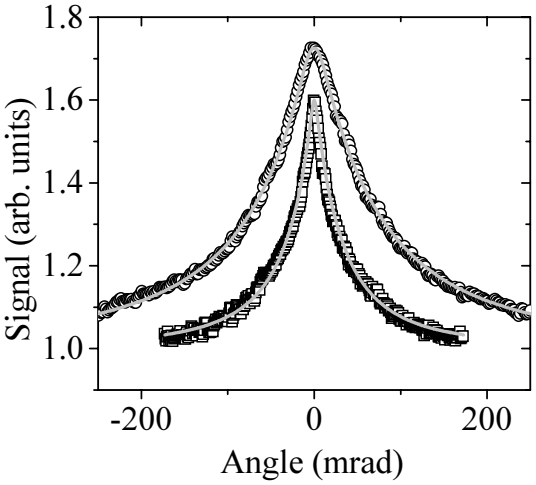

Figure 5.13:
EBS measurements of porous GaP ($N = 5 \times 10^{17}$ cm^{-3}) anodically etched at 15 V (squares) and at 16.6 V = V_{max} (circles). The solid lines through the symbols are fits using diffusion theory.

concentration N and on the etching potential V, the pore radius and the inter-pore distance can be tuned by changing either of these parameters. The biggest and most-widely spaced pores are thus obtained in low-doped GaP etched at high potential. Note that the highest possible potential V_{max} is determined by the formation of the passive layer and also depends on N (Fig. 5.4).

In the following the effect of the pore radius and of the inter-pore distance on the scattering strength of porous GaP are discussed.

Figure 5.13 shows results of EBS measurements on two porous GaP samples with $N = 5 \times 10^{17}$cm^{-3}, etched at 15 V (squares) and at 16.6 V = V_{max} (circles). The average pore radius and inter-pore distance are listed in Table 5.1. The EBS cone of the sample etched at higher potential is significantly wider, indicating stronger scattering. The transport mean free paths in these samples are

N (10^{17}cm^{-3})	V (V)	L_{dep} (μm)	ϕ (%)	r (μm)	d_p (μm)	ℓ (μm)
5	16.6	0.21	67	0.095 ± 0.02	0.15 ± 0.03	0.22 ± 0.02
6	12.7	0.17	62	0.06 ± 0.015	0.10 ± 0.03	0.46 ± 0.03
7	11.2	0.15	62	0.045 ± 0.015	0.08 ± 0.03	0.8 ± 0.04
15	7.4	0.08	65	< 0.03	< 0.06	1.24 ± 0.07
5	15	0.20	40	0.05 ± 0.015	0.15 ± 0.04	0.43 ± 0.03

Table 5.1: Extent of the depletion layer L_{dep}, porosity ϕ, average pore radius r, inter-pore distance d_p, and transport mean free path ℓ at $\lambda_o = 633$ nm of porous GaP of doping concentration N, etched at a potential V.

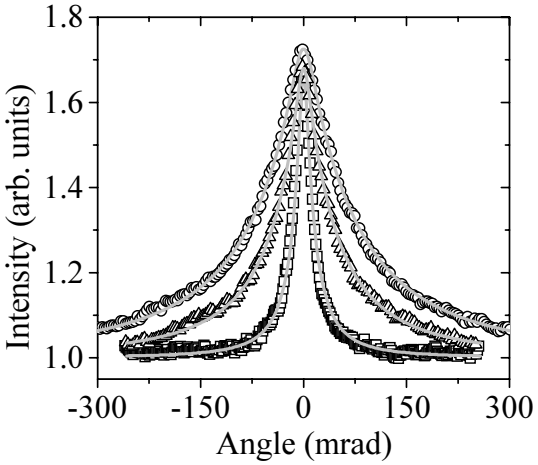

Figure 5.14:
EBS measurements of porous GaP with different doping concentrations N= 15 (squares), 6 (triangles), 5 (circles) $\times 10^{17}\text{cm}^{-3}$. All samples have a porosity of $\simeq 65\%$. The solid lines on top of the measurements are fits using diffusion theory.

$\ell = 0.22 \pm 0.02\,\mu$m (for the sample etched at 16.6 V) and $\ell = 0.43 \pm 0.03\,\mu$m (for the one etched at 15 V). These values of ℓ are obtained from the fits of the EBS measurements using diffusion theory [123]. The fits are shown as solid lines in Fig. 5.13. Internal reflection was taken into account in the fits with the values of n_e that were obtained by measuring the angular-resolved transmission.

These values of the transport mean free path are consistent with the average pore radius of the samples: the sample with bigger pores ($r = 0.95 \pm 0.02\,\mu$m) scatters light more effectively due to the larger σ_s as the pore radius becomes closer to the wavelength. Therefore, from the measurements of Fig. 5.13, we can conclude that for a certain N the maximum scattering strength can be achieved for samples etched at $V_{\max}$.

The EBS measurements of porous GaP samples of different doping concentration are plotted in Fig. 5.14. The samples were prepared with equal porosity $\phi \simeq 65\%$. The porosity is defined as the ratio of the GaP volume removed to the total volume of the porous layer. The volume of the GaP removed can be calculated from the etch charge, since the dissolution of one GaP formula unit requires six holes (reaction (5.1)). The charge is obtained by the integration of the plot of the current density versus etching time (Fig. 5.6). The porosities of different samples are listed in Table 5.1. Note that in samples with the same N etched at different potentials the porosity is larger as V increases.

For the samples with $N = 5,6,7 \times 10^{17}\text{cm}^{-3}$ of Fig. 5.14 the etching potential was $V_{\max}$, having the highest possible porosity and pore size achievable by anodic etching at room temperature. The sample with $N = 15 \times 10^{17}\text{cm}^{-3}$ was etched at 7.4 V $< V$max, so that its porosity is 65%.

In Fig. 5.15 the inverse of the scattering strength, in terms of $k\ell = \frac{2\pi}{\lambda_o} n_e \ell$, of

these samples is plotted versus the doping concentration. Angular-resolved transmission measurements showed that the effective refractive index of all the samples was in the range $n_e = 1.35 - 1.55$. The transport mean free paths ℓ were obtained from the fits to the EBS measurements of Fig. 5.14, shown as solid lines, taking $n_e = 1.45$, $\overline{R_1} = 0.5$ (obtained with Eq. (2.25) and $n_e = 1.45$). These values of ℓ are given in Table 5.1. The decrease of the transport mean free path (and therefore of $k\ell$) for lower N is due to the increase of the pore radius.

The moderately-high scattering strength of the highly-doped GaP ($k\ell \simeq 18$ for the $N = 15 \times 10^{17}\text{cm}^{-3}$ sample) can be understood by the large density of scatterers ρ. Due to the small pore size ($r < 0.03\,\mu$m) the scattering cross section of the pores in this sample is expected to be very small. However, the short separation between pores leads to a high ρ.

Due to the formation of the passive layer, the pore size and the scattering strength of porous GaP are limited by V_{max}. To further increase the scattering strength two different approaches can be used: it is expected that etching at higher temperature or using a lower viscosity electrolyte [153] will cause a shift of V_{max} to higher values, being possible to etch at higher potentials and therefore to form bigger pores. The second approach consists in increasing the pore radius by means of chemical etching. Chemical etching is discussed in the next section.

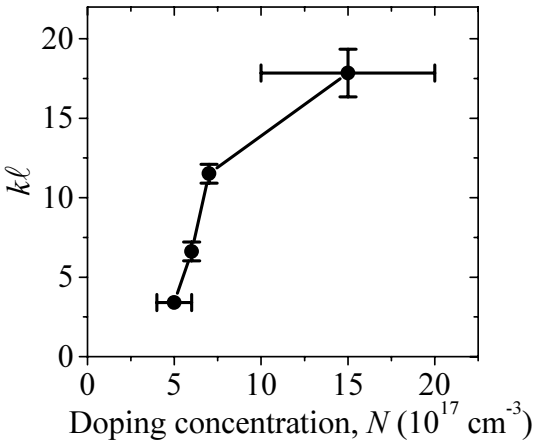

Figure 5.15:
Inverse of the scattering strength of porous GaP with a porosity of $\simeq 65\%$ as a function of the doping concentration.

5.7 Increase of the scattering strength by chemical etching

During the photochemical-etching experiments, we found that H_2O_2 chemically etches GaP at a very low rate. Since the solution of 15 ml of 0.5 M H_2SO_4 and

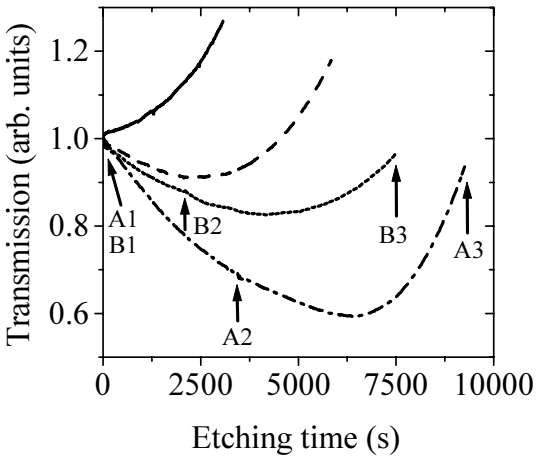

Figure 5.16:
Transmission ($\lambda_o = 633$ nm) through porous GaP during chemical etching in a solution of 15 ml of 0.5 M H_2SO_4 and 3 ml 30% H_2O_2. The solid, dashed and dotted lines correspond to samples with a doping concentration of $N = 15,7$ and $5 \times 10^{17}\text{cm}^{-3}$, respectively, etched at $V_{\max}$. The dashed-dotted line refers to a sample with $N = 7 \times 10^{17}\text{cm}^{-3}$ etched at 11 V. The arrows indicate the times at which chemical etching was stopped to measure the EBS.

3 ml 30% H_2O_2 fills the whole porous structure, the average pore radius can be uniformly increased beyond the limit imposed by $V_{\max}$.

To control the chemical etching, the transmission of a He:Ne laser beam ($\lambda_o = 633$ nm) through the samples was monitored during etching. Although GaP is transparent for $\lambda_o = 633$ nm light, strong intensities may lead to two-photon absorption via surface states. As we have seen in section 5.5, optical absorption produces photochemical etching, and will give rise to a non-uniform etching rate with the sample depth. Therefore, to avoid two-photon absorption, the He:Ne beam was attenuated.

The measurements of the transmission as a function of the chemical-etching time are plotted in Fig. 5.16. The solid, dashed and dotted lines correspond to samples with $N = 15,7$ and $5 \times 10^{17}\text{cm}^{-3}$, anodically etched at their respective $V_{\max}$. The dashed-dotted line refers to a sample with $N = 7 \times 10^{17}\text{cm}^{-3}$ etched at 11 V. The measurements of Fig. 5.16 have been normalized with respect to the transmission value before the etching was initiated.

In general, the transmission decreases to a minimum. This decrease is due to the growth of the pore radius by chemical etching. The diffuse transmission through a non-absorbing random layer is given by $T_d \propto \ell/L$ (see section 2.2.4 on page 33), where L is the thickness of the sample. As the average pore radius becomes bigger, the scattering cross section gets larger and ℓ is reduced. The scattering strength is thus increased. Since chemical etching is very slow, the change in L is negligible. The pore radius grows at the expense of the inter-pore distance. After a certain time adjacent pores start to overlap and the transmission

increases. Eventually the porous structure collapses.

For the samples with $N = 7 \times 10^{17}\text{cm}^{-3}$ etched at 11 V and the $N = 5 \times 10^{17}\text{cm}^{-3}$ etched at $V_{\max}$, the EBS was measured before chemical etching (points A1 and B1 in Figs 5.16 and 5.17). The chemical etching was stopped after 3500 s (point A2) and 2100 s (B2) respectively; the samples were dried and the EBS was measured. After these measurements were performed, the etching was continued until the transmission increased. The EBS was also measured when the chemical etching was ended (A3 and B3 in Figs 5.16 and 5.17).

The change of the transmission upon chemical etching is compared to the width of the EBS cones in Fig. 5.17. In this figure the transmission of the samples chemically etched $T_{\text{C-GaP}}$ normalized by the transmission before the chemical etching $T_{\text{A-GaP}}$ (at t=0 s or points A1 and B1 of Fig. 5.16) is plotted versus the inverse of the width of the EBS cone (normalized by the width of the cone at t=0 s). These results are discussed in the next section.

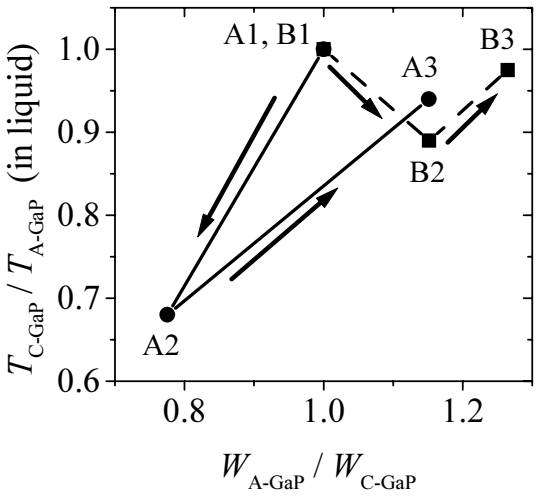

Figure 5.17: Transmission of chemically-etched GaP samples, normalized by the transmission before chemical etching, plotted versus the inverse of the normalized width of the EBS cones. The points A1, A2 and A3 correspond to a sample with a doping concentration $N = 7 \times 10^{17}\text{cm}^{-3}$ anodically etched at 11 V. The points B1, B2 and B3 are of a sample with $N = 5 \times 10^{17}\text{cm}^{-3}$ etched at 16.6 V. The arrows indicate the chronology of the chemical-etching experiments (see Fig. 5.16). The solid and dashed lines are a guides to the eye.

5.8 Discussion

In Fig. 5.17 we see that, for the sample with $N = 7 \times 10^{17}\text{cm}^{-3}$, the EBS cone gets wider while the transmission is reduced due to chemical etching (point A2). Both phenomena (reduction of the transmission and widening of the EBS cone) are consistent with an increase of the scattering strength of the sample. As mentioned in the preceding section this increase is due to the enlargement of the pore radius. When the transmission increases, due to the overlapping of adjacent pores, the EBS narrows (point A3 in Fig. 5.17).

No such consistent picture is obtained with the $N = 5 \times 10^{17}\text{cm}^{-3}$ sample. Surprisingly, the EBS cone narrows though the transmission decreases when the sample is chemically etched (point B2 in Fig. 5.17). When the transmission increases (point B3) the EBS narrows as expected.

The narrowing of the EBS cannot be explained by an increase of the absorption: if chemical etching enhances optical absorption the transmission will be reduced; however, according to diffusion theory, absorption should also widen the EBS cone [123].

A difference between the two samples of Fig. 5.17 is their scattering strength. As described in section 5.6, the scattering strengths are obtained from the fits of the EBS measurements using classical diffusion theory. In the well-behaved sample ($N = 7 \times 10^{17}\text{cm}^{-3}$) $k\ell \simeq 15$ before chemical etching. This sample was thus far from the localization transition. In the sample with $N = 5 \times 10^{17}\text{cm}^{-3}$, $k\ell \simeq 3.5$ before etching. The width of the EBS cone of this sample ($\simeq 120$ mrad) was similar to that of PA-GaP [79] (see the introduction of this chapter). These are the strongest scattering samples of visible light.

It is remarkable that although the average pore radius of the $N = 5 \times 10^{17}\text{cm}^{-3}$ sample ($r \simeq 0.095\,\mu$m) is much larger than that of PA-GaP samples ($r \simeq 0.065\,\mu$m), the width of the EBS cones are similar. This is an unexpected result, especially considering the strong influence that a change of the pore radius has on the scattering strength of porous GaP (see section 5.6).

Classical [123] and localization theories [129] predict a wider EBS cone for larger scattering strengths. Although our measurements are preliminary and a more thorough study is needed, they suggest that there is a limit for this width and that stronger scattering give rise to a narrowing of the cone.

To support this observation we have also measured the EBS of a porous GaP sample (111)-oriented, with a doping concentration of $N = 2 \times 10^{17}\text{cm}^{-3}$, anodically etched at 21.5 V. The different wafer orientation is the reason why this sample has not been further discussed in this chapter. After anodic etching, the sample was photochemically etched, and chemically etched to increase the pore size. The

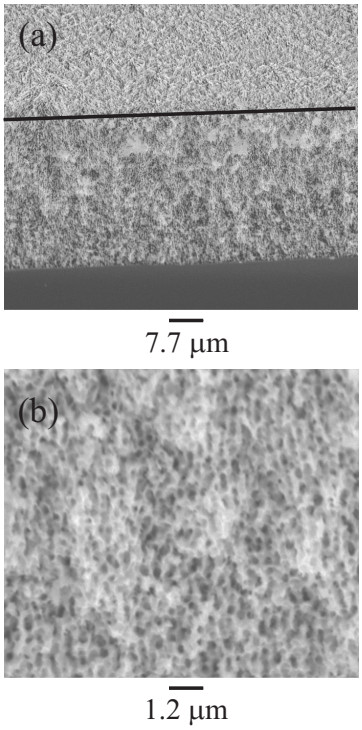

Figure 5.18:
SEM photographs of a sample of porous GaP, (111)-oriented, with a doping concentration of $N = 2 \times 10^{17}\text{cm}^{-3}$, anodically etched at 21.5 V, photochemically etched and chemically etched. (a) is a SEM photograph of cleaved cross section of the porous layer. The drawn line marks the sample edge. The region above the line is the sample surface. The dark part at the bottom of the photograph is the non-etched GaP wafer. (b) is a higher magnification photograph of the porous structure.

resulting sample can be seen in Fig. 5.18, where (a) is a SEM photograph of a cleaved cross section of the porous layer. The drawn line marks the sample edge. The region above the line is thus the sample surface. The dark part at the bottom of the photograph is the non-etched GaP wafer. A higher magnification photograph of the porous structure is displayed in Fig. 5.18 (b). The average pore radius in this sample was $r = 0.12 \pm 0.03\,\mu$m, thus larger than the pore radius of the samples discussed before. In spite of the large pore size, the EBS cone has a width of only 100 mrad, which according to diffusion theory corresponds to $k\ell \simeq 5$.

The preliminary results of the chemical etching that have been described require a more systematic study. At the time this thesis was being written, the EBS at small angles was not investigated in detail. Since Anderson localization leads to a rounding of the EBS intensity at small angles [79, 129] (see section 2.4), this investigation must be done. As we have seen in chapter 3 and 4, total transmission measurements on a series of samples with different thickness and at different wavelengths can be very enlightening.

As explained in section 5.3.2 the porous structure grows downwards once the current density reaches a constant value. The effect on the EBS of the porous

region formed in the first stage of the anodic etching, i.e., while the current density increases (see Fig. 5.6), must be investigated. The optical anisotropy that might be present in anodically-etched GaP also needs to be studied.

A

Energy density coherent potential approximation

In chapter 3 the energy density coherent potential approximation (EDCPA) is used to calculate the scattering mean free path ℓ_s and the localization parameter $k\ell_s$ in system formed by silicon scatterers. This theory has been developed by C.M. Soukoulis and coworkers and its principles are summarized in this appendix. A detailed description of the EDCPA can be found in Refs. [84, 163, 164].

Consider a random system of spheres with radius r and dielectric constant ε_1 in matrix formed by a material of dielectric constant ε_2. The scatterers volume fraction is ϕ. The EDCPA uses a coated sphere with a radius r_{cs} as the basic scattering unit. The dielectric constant of the sphere core is ε_1, while the dielectric constant of the coating is ε_2. The distribution of the spacing between adjacent spheres is approximated by a delta function at r_{cs}, which assumes that the spheres can not overlap.

The dielectric constant of the effective medium ε_e is self-consistently determined by considering that the averaged energy density is uniform over length scales larger than the coated sphere. This consideration requires that the energy of a plane wave stored in a coated sphere should be the same as the energy stored by a plane wave in a volume of the effective medium equal to that of the coated sphere. The self-consistent equation for ε_e can be thus written as

$$\int_0^{r_{cs}} U_1(\mathbf{r}, \varepsilon_1, \varepsilon_2) \mathrm{d}\mathbf{r} = \int_0^{r_{cs}} U_2(\mathbf{r}, \varepsilon_e) \mathrm{d}\mathbf{r} \,, \tag{5.5}$$

where $U_1(\mathbf{r}, \varepsilon_1, \varepsilon_2)$ and $U_2(\mathbf{r}, \varepsilon_e)$ are the energy density in the coated sphere and in the effective medium.

With ε_e the scattering properties, such as ℓ_s, $k\ell_s$, D_B and v_e, can be calculated using multiple-scattering theory [164, 165].

One of the most remarkable conclusions of the EDCPA is that localization of light can be easier achieved in an inverse structure ($\varepsilon_2 > \varepsilon_1$), rather than in a direct structure ($\varepsilon_1 > \varepsilon_2$). This result is depicted in Fig. A1, where contour plots of the localization parameter $k\ell_s$ versus the dielectric contrast and the scatterers volume fraction are represented. Figure (a) corresponds to a direct structure and (b) to an inverse structure. As can be appreciated, for each value of the dielectric contrast $k\ell_s$ is lower in the inverse structure.

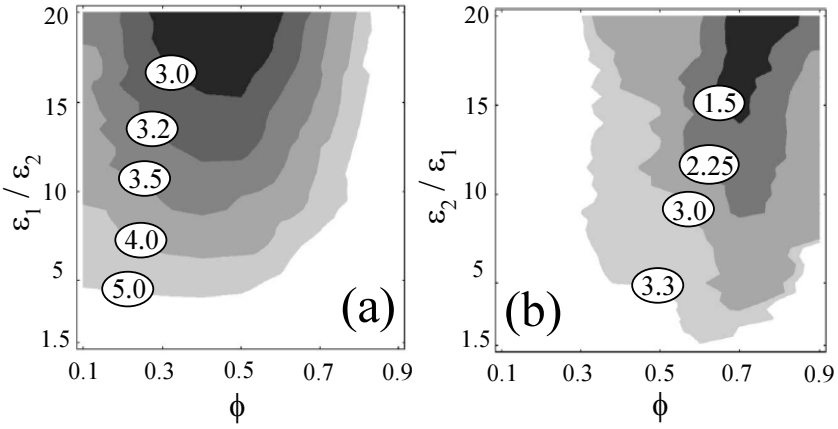

Figure A.1: Contour plots of the localization parameter $k\ell_s$ as a function of the dielectric contrast and of the scatterers volume fraction. Figure (a) corresponds to a direct structure ($\varepsilon_1 > \varepsilon_2$) and (b) corresponds to an inverse structure ($\varepsilon_2 > \varepsilon_1$). Figure reproduced from Ref. [85].

B

Extrapolation length with an absorbing layer

The top of the Ge samples in chapter 4 is a thin absorbing layer. As it is demonstrated in this appendix, the absorption in the top layer affects the extrapolation factor (here called τ_e) of the interface.

The calculation of the reflection coefficient of a double interface can be found in Ref. [135]. This calculation is here generalized for the case of an absorbing layer. With the reflection coefficient, τ_e can be evaluated as explained in section 2.2.2.

We assume a weakly or non-absorbing multiple scattering sample with an homogeneous and absorbing layer of thickness δ at one interface. The effective refractive index of the sample is given by n_e, while the absorbing layer has a complex refractive index $n_\delta^c = n_\delta + i\kappa_\delta$. If $\kappa_\delta \ll n_\delta$ the absorption coefficient of this layer is given by $\alpha_\delta = 2\pi\kappa_\delta/\lambda$. The transmitted fraction $T_{ab}(\theta_1)$ of the diffuse light incident at the interface sample-layer at angle θ_1 (see inset of Fig. B.1) is refracted according to Snell's law and undergoes a ballistic propagation along the absorbing layer at angle θ_2. Due to the absorption, the intensity of the transmitted fraction in attenuated by the factor $e^{-\alpha_\delta \delta/\cos\theta_2}$. The light reaching the layer-air interface may be reflected with a probability given by the Fresnel's reflection coefficient, $R_{bc}(\theta_2)$. The reflected fraction reaches the interface layer-sample, after being attenuated, where it may be reflected etc. Considering these multiple reflections at both interfaces the reflection coefficient of the absorbing layer is

$$R(\theta) = R_{ab}(\theta_1) + \frac{T_{ab}(\theta_1)R_{bc}(\theta_2)R_{ba}(\theta_2)e^{-2\alpha_\delta\delta/\cos\theta_2}}{1 - R_{ba}(\theta_2)R_{bc}(\theta_2)e^{-2\alpha_\delta\delta/\cos\theta_2}} \,. \tag{B.1}$$

In Eq. (B.1) the indexes a, b, c stand for medium a = sample , b = absorbing layer

and c = outside medium, as it is illustrated in the inset of Fig. B.1, and, for instance, R_{ab} is the Fresnel's reflection coefficient of the interface between medium a and b.

With the reflection coefficient, given by Eq. (B.1), the extrapolation factor can be calculated following the procedure described in section 2.2.2.

In Fig. B.1 the extrapolation factor τ_e is plotted as a function of $(\delta\alpha_\delta)^{-1}$. In this example $n_e = n_\delta = 1.6$ and , for simplicity, the Fresnel's reflection coefficients are calculated for dielectric media. As the absorption in the layer gets stronger, τ_e becomes smaller. The reason for the decrease of τ_e is the lower light intensity that leaves the sample due to absorption in the top layer.

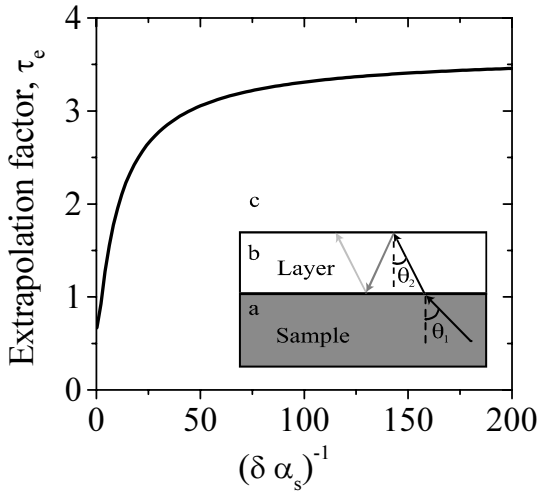

Figure B.1: Extrapolation factor of a double interface or layer as a function of $(\delta\alpha_\delta)^{-1}$, where δ is the thickness of the layer and α_δ its absorption coefficient. Inset: The light leaving the sample (medium a) at an angle θ_1 is refracted according to Snell's law. It propagates through the layer (medium b), where it is attenuated by absorption. At the interface between medium b and c the light may be reflected with a probability given by the Fresnel's reflection coefficient. The reflection coefficient of the layer is given by the multiple reflections at both interfaces.

List of symbols

Symbol	Description
α	absorption coefficient
α_{TL}	absorption coefficient in the top layer (chapter 4)
δ	thickness of the top layer (chapter 4)
θ	backscattering angle (in section 2.3 and chapter 5)
θ_e	transmission angle
λ	wavelength
λ_o	wavelength in vacuum
λ_{gap}	band-gap wavelength
λ_U	wavelength of the Urbach band edge
ξ	localization legth
ζ	coherence legth
ρ	density of scatterers
σ_a	absorption cross section
σ_{ex}	extinction cross section
σ_s	scattering cross section
ε_o	vacuum permittivity
ε	dielectric constant
ε_e	dielectric constant of an effective medium
κ_e	imaginary part of the dielectric constant
Γ	decay time of the transmitted intensity
ϕ	scatterers volume fraction (or porosity in chapter 5)
μ_e	cosine of the transmission angle θ_e
τ	transport mean free time
τ_a	absorption mean free time
τ_ρ	dephasing time
$\tau_{e_{1,2}}$	extrapolation factor at boundary 1 or 2
ϑ	scattering angle

Symbol	Description
φ	polarizability
$\Re$	fraction of absorbed energy
a	albedo
d	dimension
d_{p}	(average) inter-pore distance
D	diffusion constant
D_{B}	Boltzman diffusion constant
e	electron charge
E	complex amplitude
I	intensity
I_{o}	incident intensity
I_{coh}	coherently-transmitted intensity
J	diffuse flux
$J_{1,2}$	diffuse flux at boundary 1 or 2
$k = 2\pi n_{\mathrm{e}}/\lambda_{\mathrm{o}}$	wave vector in the medium
$k_{\mathrm{o}} = 2\pi/\lambda_{\mathrm{o}}$	wave vector in vacuum
$k\ell_{\mathrm{s}}$	localization parameter
$k\ell_{\mathrm{s}} \simeq 1$	Ioffe-Regel criterium for localization
$(k\ell_{\mathrm{s}})^{-1}$	photonic or scattering strength
ℓ	transport mean free path
ℓ_{a}	absorption mean free path
ℓ_{B}	Boltzman mean free path
ℓ_{c}	critical mean free path
ℓ_{ex}	extinction mean free path
ℓ_{s}	scattering mean free path
L	sample thickness
L_{ρ}	dephasing length
L_{a}	absorption length
L_{d}	decay length of the total transmission (chapter 3)
L_{dep}	width of the depletion layer
m	refractive index contrast
n	refractive index
n_{o}	vacuum refractive index
n_{e}	effective refractive index
N	doping concentration

Symbol	Description
$P(\mu_e)$	angular distribution of the transmitted light
r	(average) scatterer (or pore) radius
R	total reflection
$R(\theta)$	Fresnel's reflection coefficient at angle θ
R_d	diffuse total reflection
$\overline{R}_{1,2}$	average reflectivity at boundary 1 or 2
T	total transmission
T_{coh}	coherent transmission
T_d	diffuse total transmission
s	path length
v_e	energy velocity
U_d	diffuse energy density
V	potential
V_{fb}	flat band potential
V_{max}	potential of maximum anodic current
W	width of the enhanced backscattering cone
$z_{e_{1,2}}$	extrapolation length at boundary 1 or 2
z_p	location of the source of diffuse light

List of abbreviations

Abbreviation	Description
EBS	enhanced backscattering
EDCPA	energy density coherent potential approximation
EDX	energy-dispersion X-ray spectroscopy
FEL	free electron laser
FELIX	free electron laser for infrared experiments, The Netherlands
FTIR	Fourier transform infrared spectrometer
IS	integrating sphere
MCT detector	mercury-cadmium-telluride detector
RTE	radiative-transfer equation
SCE	saturated calomel electrode
SEM	scanning-electron microscope

Bibliography

[1] H.C. van de Hulst. *Light scattering by small particles* (Dover Publications Inc., New York, 1981).

[2] C.F. Bohren and D.R. Huffman. *Absorption and scattering of light by small particles* (Wiley-Interscience, New York, 1983).

[3] Ref. [1], chapter 6.

[4] Ref. [1], part II.

[5] Ref. [2], chapters 4 and 8.

[6] M. Born and E. Wolf. *Principles of optics*, pp. 38-51 (Pergamon Press, Oxford, 1986).

[7] E. Yablonovitch. *Inhibited spontaneous emission in solid-state physics and electronics*, Phys. Rev. Lett. **58**, 2059 (1987).

[8] S. John. *Strong localization of photons in certain disordered dielectric superlattices*, Phys. Rev. Lett. **58**, 2486 (1987).

[9] R.W. James. *The optical principles of the diffraction of X-rays* (Bell, London, 1954).

[10] E. Yablonovitch, T.J. Gmitter, and K.M. Leung. *Photonic band structure: The face-centered-cubic case employing nonspherical atoms*, Phys. Rev. Lett. **67**, 2295 (1991).

[11] *Photonic crystals and light localization in the* 21^{st} *century*, edited by C.M. Soukoulis (Kluwer Academic Publishers, Dordrecht, 2001).

[12] J.E.G.J. Wijnhoven and W.L. Vos. *Preparation of photonic crystals made of air spheres in titania*, Science **281**, 802 (1998).

[13] A. Blanco, E. Chomski, S. Grabtchak, M. Ibisate, S. John, S.W. Leonard, C. Lopez, F. Meseguer, H. Minguez, J.P. Mondia, G.A. Ozin, O. Toader, and H.M. van Driel. *Large-scale systhesis of a silicon photonic crystal with a complete three-dimensional bandgap near 1.5 micrometers*, Nature **405**, 437 (2000).

[14] H. Kosaka, T. Kawashima, A. Tomita, M. Notomi, T. Tamamura, T. Sato, and S. Kawakami. *Superprism phenomena in photonic crystals*, Phys. Rev. B **58**, R10096 (1998).

[15] O. Painter, R.K. Lee, A. Scherer, A. Yariv, J.D. O'Brien, P.D. Dapkus and I. Kim. *Two-dimensional photonic band-gap defect mode laser*, Science **284**, 1819 (1999).

[16] H. Benisty, D. Labilloy, C. Weisbuch, C.J.M. Smith, T.F. Krauss, D. Cassagne, A. Béraud, and C. Jouanin. *Radiation losses of waveguide-based two-dimensional photonic crystals: Positive role of the substrate*, Appl. Phys. Lett. **76**, 532 (2000); S.W.

Leonard, H.M. van Driel, A. Birner, U. Gösele, and P.R. Villeneuve. *Single-mode transmission in two-dimensional macroporous silicon photonic crystal waveguides*, Opt. Lett. **25**, 1550 (2000).

[17] J.C. Knight, J. Broeng, T.A. Birks, and P.St.J. Russell. *Photonic band gap guidance in optical fibers*, Science **282**, 1476 (1998).

[18] H. De Neve, J. Blondelle, P. van Daele, P. Demeester, R. Baets, and G. Borghs. *Recycling of guided mode light emission in planar microcavity light emitting diodes*, Appl. Phys. Lett. **70**, 799 (1997).

[19] H.S. Sözüer, J.W. Haus, and R. Inguva. *Photonic bands: Convergence problems with the plane-wave method*, Phys. Rev. B **45**, 13962 (1992).

[20] A.F. Ioffe and A.R. Regel. *Non-crystalline amorphous, and liquid electronic semiconductors*, Prog. Semicond. **4**, 237 (1960).

[21] A. Ishimaru. *Wave propagation and scattering in random media* (Academic Press, New York, 1978).

[22] Ref. [21], vol. 1, pp. 175-178.

[23] J.W. Goodman, in *laser speckle and related phenomena*, chapter 2, edited by J.C. Dainty (Springer-Verlag, Berlin, 1984).

[24] M.P. Albada, B.A. van Tiggelen, A. Lagendijk, and A. Tip. *Speed of propagation of classical waves in strongly scattering media*, Phys. Rev. Lett. **66**, 3132 (1991).

[25] B.A. van Tiggelen, A. Lagendijk, M.P. Albada, and A. Tip. *Speed of light in random media*, Phys. Rev. B **45**, 12233 (1992).

[26] D.E. Khmel'nitskii. *Localization and coherent scattering of electrons*, Physica B **126**, 235 (1984).

[27] P. Sheng. *Introduction to wave scattering, localization, and mesoscopic phenomena* (Academic Press, New York, 1995).

[28] Ref. [27], chapter 7.

[29] P.W. Anderson. *Absence of diffusion in certain random lattices*, Phys. Rev. **109**, 1492 (1958).

[30] D. Vollhardt and P. Wölfle. *Anderson localization in $d \leq 2$ dimensions: A self-consistent diagrammatic theory*, Phys. Rev. Lett. **45**, 842 (1980). *Diagrammatic, self-consistent treatment of the Anderson localization problem in $d \leq 2$ dimensions*, Phys. Rev. B **22**, 4666 (1980); *Scaling equations from a self-consistent theory of Anderson localization*, Phys. Rev. Lett. **48**, 699 (1982).

[31] E.N. Economou, C.M. Soukoulis, and A.D. Zdetsis. *Conductivity in disordered systems*, Phys. Rev. B **31**, 6483 (1985).

[32] Ref. [1], chapter 2.

[33] P.R. Wallace. *Mathematical analysis of physical problems*, pp. 360-361 (Dover Publications Inc., New York, 1984).

[34] R. Dalichaouch, J.P. Armstrong, S. Schultz, P.M. Platzman, and S.L. McCall. *Microwave localization by two dimensional random scattering*, Nature (London) **354**, 53 (1991).

[35] S. He and J.D. Maynard. *Detailed measurement of inelastic scattering in Anderson localization*, Phys. Rev. Lett. **57**, 3171 (1986).

[36] R.L. Weaver. *Anderson localization of ultrasond*, Wave motion **12**, 129 (1990).

[37] L. Ye, G. Cody, M. Zhou, P. Sheng, and A.N. Norris. *Observation of bending wave localization and quasi mobility edge in two dimensions*, Phys. Rev. Lett. **69**, 3080 (1992).

[38] M. Stoytchev and A.Z. Genack. *Observations of non-Rayleigh statistics in the approach to photon localization*, Opt. Lett. **24**, 262 (1999).

[39] García-Martín, J.A. Torres, and J.J. Sáenz. *Transition from diffusive to localized regimes in surface corrugated optical waveguides*, Appl. Phys. Lett. **71**, 1912 (1997).

[40] R.L. Weaver. *Anomalous diffusivity and localization of classical waves in disordered media: the effect of dissipation*, Phys. Rev. Lett. **53**, 2169 (1993).

[41] S. Yosefin. *Localization in absorbing media*, Europhys. Lett. **25**, 675 (1994).

[42] S. John. *Electromagnetic absorption in a disordered medium near a photon mobility edge*, Phys. Rev. B **47**, 1077 (1984).

[43] N. Garcia and A.Z. Genack. *Anomalous photon diffusion at the threshold of the Anderson localization transition*, Phys. Rev. Lett. **66**, 1850 (1991).

[44] V.S. Letokhov. *Generation of light by a scattering medium with negative resonance absorption*, Sov. Phys. JETP **26**, 835 (1968).

[45] N.M. Lawandy, R. Balachandran, A. Gomes, and E. Sauvain. *Laser action in strongly scattering media*, Nature (London) **368**, 436 (1994).

[46] W.L. Sha, C.-H. Liu, and R.R. Alfano. *Spectral and temporal measurements of laser action of Rhodamine 640 dye in strongly scattering media*, Opt. Lett. **19**, 1922 (1994).

[47] D.S. Wiersma, M.P. van Albada, and A. Lagendijk. *Coherent backscattering of light from amplifying random media*, Phys. Rev. Lett. **75**, 1739 (1995).

[48] M. Siddique, R.R. Alfano, G.A. Berger, M. Kempe, and A.Z. Genack. *Time-resolved studies of stimulated emission from colloidal dye solutions*, Opt. Lett. **21**, 450 (1996).

[49] P.C. de Oliveira, A.E. Perkins, and N.M. Lawandy. *Coherent backscattering from high-gain scattering media*, Opt. Lett. **21**, 1685 (1996).

[50] G.A. Berger, M. Kempe, and A.Z. Genack. *Dynamics of stimulated emission from random media*, Phys. Rev. E **56**, 436 (1997).

[51] G. van Soest, M. Tomita, and A. Lagendijk. *Amplifying volume in scattering media*, Opt. Lett. **24**, 306 (1999).

[52] X. Jiang and C.M. Soukoulis. *Time dependent theory for random lasers*, Phys. Rev. Lett. **85**, 70 (2000).

[53] G. van Soest, F.J. Poelwijk, R. Sprik, and A. Lagendijk. *Dynamics of a random laser above threshold*, Phys. Rev. Lett. **86**, 1522 (2001).

[54] S.V. Frolov, Z.V. Vardeny, K. Yoshino, A. Zakhidov, and R, Baughman. *Stimulated emission in high-gain organic media*, Phys. Rev. B **59**, R5284 (1999).

[55] H. Cao, Y.G. Zhao, S.T. Ho, E.W. Seeling, Q.H. Wang, and R.P.H. Chang. *Random laser action in semiconductor powder*, Phys. Rev. Lett. **82**, 2278 (1999).

[56] H. Cao, J.Y. Xu, E.W. Seeling, and R.P.H. Chang. *Microlaser made of disordered media*, Appl. Phys. Lett. **76**, 2997 (2000).

[57] H. Cao et al. *Spatial confinement of light in active random media*, Phys. Rev. Lett.

84, 5584 (2000).

[58] H. Cao, Y. Ling, J.Y. Xu, C.Q. Cao, and P. Kumar. *Photon statistics of random lasers with resonant feedback*, Phys. Rev. Lett. **86**, 4524 (2001).

[59] A. Mitra and R.K. Thareja. *Photoluminiscence and ultraviolet laser emission from nanocrystalline ZnO thin films*, J. Appl. Phys. **89**, 2025 (2001).

[60] S.V. Shkunov, M.C. Dalong, M.E. Raikh, Z.V. Vardeny, A.A. Zakhidov, and R.H. Baughman. *Photonic versus random lasing in opal photonic single crystals*, Synthetic Met. **116**, 485 (2001).

[61] G. van Soest. *Experiments on random lasers*, PhD. thesis, University of Amsterdam (2001).

[62] Y. Sun, J.B. Ketterson, and G.K.L. Wong. *Excitonic gain and stimulated ultraviolet emission in nanocrystalline zinc-oxide powder*, Appl. Phys. Lett. **77**, 2322 (2000).

[63] D.J. Thouless. *Maximum metallic resistance in thin wires*, Phys. Rev. Lett. **39**, 1167 (1977).

[64] E. Abrahams, P.W. Anderson, D.C. Licciardello, and T.V. Ramakrishnan. *Scaling theory of localization: absence of quantum diffusion in two dimensions*, Phys. Rev. Lett. **42**, 673 (1979).

[65] B.L. Altshuler, A.G. Aronov, and D.E. Khmelnitsky. *Suppression of localization effects by the high frequency field and the Nyquist noise*, Solid State Commun. **39**, 619 (1981).

[66] G. Bergmann. *Physical interpretation of weak localization: a time-of-flight experiment with conduction electrons*, Phys. Rev. B **28**, 2914 (1983).

[67] P.W. Anderson. *The question of classical localization. A theory of white paint?*, Philos. Mag. B **52**, 505 (1985).

[68] M.P. van Albada and A. Lagendijk. *Observation of weak localization of light in a random medium*, Phys. Rev. Lett. **55**, 2692 (1985).

[69] P.E. Wolf and G. Maret. *Weak localization and coherent backscattering of photons in disordered media*, Phys. Rev. Lett. **55**, 2696 (1985).

[70] Y. Kuga and A. Ishimaru. *Retroreflectance from a dense distribution of spherical particles*, J. Opt. Soc. Am. A **1**, 831 (1984).

[71] S. Feng, C. Kane, P.A. Lee, and A.D. Stone. *Correlations and fluctuations of coherent wave transmission through disordered media*, Phys. Rev. Lett. **61**, 834 (1988). S. Feng and P.A. Lee. *Mesoscopic conductors and correlations in laser speckle patterns*, Science **251**, 633 (1991).

[72] M.P. van Albada, J.F. de Boer, and A. Lagendijk. *Observation of long-range correlation in the transport of coherent light through a random medium*, Phys. Rev. Lett. **64**, 2787 (1990).

[73] A.Z. Genack, N. Garcia, and W. Polkosnik. *Long-range intensity correlation in random media*, Phys. Rev. Lett. **65**, 2129 (1990).

[74] F. Scheffold and G. Maret. *Universal conductance fluctuations of light*, Phys. Rev. Lett. **81**, 5800 (1998).

[75] J.M. Drake and A.Z. Genack. *Observation of nonclassical optical diffusion*, Phys. Rev. Lett. **63**, 259 (1989).

[76] D.S. Wiersma, P. Bartolini, A. Lagendijk, and R. Righini. *Anderson localization of*

Light, Nature (London) **390**, 671 (1997).

[77] F. Scheffold, R. Lenke, R. Tweer, and G. Maret. *Localization or classical diffusion of light?* Nature (London) **398**, 206 (1999). D.S. Wiersma, J. Gómez Rivas, P. Bartolini, A. Lagendijk, and R. Righini. Nature (London) **398**, 207 (1999).

[78] Z.Q. Zhang, C.C. Wong, K.K. Fung, Y.L. Ho, W.L. Chan, S.C. Kan, T.L. Chan, and N. Cheung. *Observation of localized electromagnetic waves in three-dimensional networks of waveguides*, Phys. Rev. Lett. **81**, 5540 (1998).

[79] F.J.P. Schuurmans, M. Megens, D. Vanmaekelbergh, and A. Lagendijk. *Light scattering near the localization transition in macroporous GaP networks*, Phys. Rev. Lett. **83**, 2183 (1999).

[80] F.J.P. Schuurmans, D. Vanmaekelbergh, J. van de Lagemaat, and A. Lagendijk. *Strongly photonic macroporous gallium phosphide networks*, Science **284**, 141 (1999).

[81] A.A. Chabanov, M. Stoytchev, and A.Z. Genack. *Statistical signatures of photon localization*, Nature (London) **404**, 850 (2000).

[82] D. Sornette and B. Souillard. *Strong localization of waves by internal resonances*, Europhys. Lett. **7**, 269 (1988).

[83] B.A. van Tiggelen, A. Lagendijk, A. Tip, and G.F. Reiter. *Effect of resonant scattering on localization of waves*, Europhys. Lett. **15**, 535 (1991).

[84] K. Busch and C.M. Soukoulis. *Transport properties of random media: a new effective medium theory*, Phys. Rev. Lett. **75**, 3442 (1995).

[85] K. Busch and C.M. Soukoulis. *Energy-density CPA: a new effective medium theory for classical waves*, Physica B **296**, 56 (2001).

[86] A. Kirchner, K. Busch and C.M. Soukoulis. *Transport properties of random arrays of dielectric cylinders*, Phys. Rev. B **57**, 277 (1998).

[87] F.J.P. Schuurmans. *Light in complex dielectrics*, PhD. thesis, University of Amsterdam (1999).

[88] R.H. Kop, P. de Vries, R. Sprik, and A. Lagendijk. *Observation of anomalous transport of strongly multiple scattered light in thin disordered slabs*, Phys. Rev. Lett. **79**, 4369 (1997).

[89] Z.Q. Zhang, I.P. Jones, H.P. Schriemer, J.H. Page, D.A. Weitz, and P. Sheng. *Wave transport in random media: the ballistic to diffusive transition*, Phys. Rev. E **60**, 4843 (1999).

[90] J. Gómez Rivas, R. Sprik, C.M. Soukoulis, K. Busch, and A. Lagendijk. *Optical transmission through very strong and polydisperse scattering media*, Europhys. Lett. **48**, 22 (1999).

[91] J. Gómez Rivas, R. Sprik, and A. Lagendijk. *Optical transmission through very strong scattering media*, Ann. Phys. (Leipzig) **8**, SI-77 (1999).

[92] J. Gómez Rivas, R. Sprik, A. Lagendijk, L.D. Noordam, and C.W. Rella. *Optical transmission and reflection in Ge powder close to the Anderson localization transition*, Phys. Rev. E **62**, R4540 (2000).

[93] J. Gómez Rivas, R. Sprik, A. Lagendijk, L.D. Noordam, and C.W. Rella. *Static and dynamic transport of light close to the Anderson localization transition*, Phys. Rev. E **63**, 046613 (2001).

[94] A. Lagendijk, J. Gómez Rivas, A. Imhof, F.J.P. Schuurmans, and R. Sprik. *Propagation of light in disordered semiconductor materials*, in Ref. [11].

[95] R.W. Tjerkstra, J. Gómez Rivas, D. Vanmaekelbergh, and J.J. Kelly. *Porous GaP multilayers formed by electrochemical etching*, accepted for publication in Electrochem. and Solid-State Lett. (2002).

[96] J. Gómez Rivas, R.W. Tjerkstra, D. Vanmaekelbergh, J.J. Kelly, and A. Lagendijk. *Tunable photonic strength in porous GaP*, submitted.

[97] J. Gómez Rivas, D.H. Dau, A. Imhof, R. Sprik, B. Bret, P.M. Johnson, T.W. Hijmans, and A. Lagendijk. *Experimental determination of the effective refractive index in strongly-scattering media*, submitted.

[98] B.A. van Tiggelen and A. Lagendijk, in *new aspects of electromagnetic and acoustic wave diffusion*, pp. 6-7, edited by POAN Research Group (Springer-Verlag, Berlin, 1998).

[99] B.A. van Tiggelen, in *diffuse waves in complex media*, pp. 17-18, edited by J.-P. Fouque (Kluwer Academic Publishers, Dordrecht, 1999).

[100] S. Chandrasekar. *Radiative transfer* (Dover, New York, 1960).

[101] R.M. Gody and Y.L. Yung. *Atmospheric radiation: Theoretical basis* (Oxford University Press, Oxford, 1989).

[102] E. Akkermans, P.E. Wolf, and R. Maynard. *Coherent backscattering of light by disordered media: analysis of the peak line shape*, Phys. Rev. Lett. **56**, 1471 (1986).

[103] Ref. [21], vol. 1, chapter 9.

[104] A.Z. Genack. *Optical transmission in disordered media*, Phys. Rev. Lett. **58**, 2043 (1987).

[105] G.H. Watson, P.A. Fleury, and S.L. McCall. *Search for photon localization in the time domain*, Phys. Rev. Lett. **58**, 945 (1987).

[106] J.H. Li, A.A. Lisyansky, T.D. Cheung, D. Livdan, and A.Z. Genack. *Transmission and surface intensity profiles in random media*, Europhys. Lett. **22**, 675 (1993).

[107] J.H. Page, H.P. Schriemer, A.E. Bailey, and D.A. Weitz. *Experimental test of the diffusion approximation for multiple scattered sound*, Phys. Rev. E **52**, 3106 (1995).

[108] A. Tourin, M. Fink, and A. Derode. *Multiple scattering of sound*, Wave Random Media **10**, R31 (2000).

[109] D.J. Durian and J. Rudnick. *Photon migration at short times and distances and in cases of strong absorption*, J. Opt. Soc. Am. A **14**, 235 (1997).

[110] S. Glasstone and M.C. Edlund. *The elements of nuclear reactor theory* (Dover, New York, 1960).

[111] A. Lagendijk, R. Vreeker, and P. de Vries. *Influence of internal reflection on diffusive transport in strongly scattering media*, Phys. Lett. A **136**, 81 (1989).

[112] J.X. Zhu, D.J. Pine, and D.A. Weitz. *Internal reflection of diffusive light in random media*, Phys. Rev. A **44**, 3948 (1991).

[113] Ref. [21], vol. 1, pp. 180.

[114] M.U. Vera and D.J. Durian. *Angular distribution of diffusely transmitted light*, Phys. Rev. E **53**, 3215 (1996).

[115] F.C. MacKintosh, J.X. Zhu, D.J. Pine, and D.A. Weitz. *Polarization memory of multiply scattered light*, Phys. Rev. B **40**, 9342 (1989).

[116] Ref. [2], pp. 213-219.
[117] S. Datta, C.T. Chan, K.M. Ho, and C.M. Soukoulis. *Effective dielectric constant of periodic composite structures*, Phys. Rev. B **48**, 14936 (1993).
[118] N. Garcia, A.Z. Genack, and A.A. Lisyansky. *Measurements of the transport mean free path of diffusing photons*, Phys. Rev. B **46**, 14475 (1992).
[119] D.J. Durian. *Penetration depth for diffusing-wave spectroscopy*, Appl. Opt. **34**, 7100 (1995).
[120] M.B. van der Mark. *Propagation of light in disordered media: a search for Anderson localization*, PhD. thesis, University of Amsterdam (1990).
[121] A.Z. Genack and J.M. Drake. *Relationship between optical intensity, fluctuations and pulse propagation in random media*, Europhys. Lett. **11**, 331 (1990).
[122] Ref. [27], chapter 5.
[123] M.B. van der Mark, M.P. van Albada, and A. Lagendijk. *Light scattering in strongly scattering media: multiple scattering and weak localization*, Phys. Rev. B. **37**, 3575 (1988).
[124] P.N. den Outer. *Multiple light scattering in random scattering media*, PhD. thesis, University of Amsterdam (1995).
[125] I. Edrei and M. Kaveh. *Weak localization of photons and backscattering from finite systems*, Phys. Rev. B **35**, 6461 (1987).
[126] S. Etemad, R. Thompson, M.J. Andrejco, S. John, and F.C. MacKintosh. *Weak localization of photons: Termination of coherent random walks by absorption and confined geometry*, Phys. Rev. Lett. **59**, 1420 (1987).
[127] P.E. Wolf, G. Maret, E. Akkermans, and R. Maynard. *Optical coherent backscattering by random media: an experimental study*, J. Phys. France **49**, 63 (1988).
[128] S. Etemad, R. Thompson, and M.J. Andrejco. *Weak localization of photons: Universal fluctuations and ensemble averaging*, Phys. Rev. Lett. **57**, 575 (1986).
[129] B.A. van Tiggelen, A. Lagendijk, and D.S. Wiersma. *Reflection and transmission of waves near the localization threshold*, Phys. Rev. Lett. **84**, 4333 (2000).
[130] J.R. DeVore. *Refractive index of Rutile and Sphalerite*, J. Opt. Soc. Am. **41**, 416 (1951).
[131] *Handbook of optical constants of solids*, edited by E.D. Palik (Princeton University Press, New York, 1952).
[132] D.F. Edwards, in Ref. [131], p. 547.
[133] R.F. Potter, in Ref. [131], p. 465.
[134] R.J. Hunter. *Foundations of colloid science*, vol. 1, chapter 3 (Clarendon Press, Oxford, 1993).
[135] P.D. Kaplan, M.H. Kao, A.G. Yodh, and D.J. Pine. *Geometric constrains for the design of diffusing-wave spectroscopy experiments*, Appl. Opt. **32**, 3828 (1993).
[136] F. Urbach. *The long-wavelength edge of photographic sensitivity and of the electronic absorption of solids*, Phys. Rev. **92**, 1324 (1953).
[137] *Handbook of spectrocopy*, p. 20, edited by J.W. Robinson (CRC Press, Cleveland, 1974).
[138] D. Oepts, A.F.G. van der Meer, and P.W. Amersfoort. *The free-electron-laser user facility felix*, Infrared Phys. Technol. **36**, 297 (1995).

[139] *Handbook of optics*, vol. 2 , p. 33.56, edited by M. Bass (McGraw-Hill, Inc., New York, 1995).
[140] A.G. Bell. Paper presented at the 29th meeting of the American Association for the Advancement of Science (Boston, 1880).
[141] A. Rosencwaig and A. Gersho. *Photoacoustic effect with solids: a theoretical treatment*, Science **190**, 556 (1975).
[142] F.A. McDonald and G.C. Wetsel. *Generalized theory of the photoacoustic effect*, J. Appl. Phys. **49**, 2313 (1978).
[143] S.J. McGovern, B.S.H. Royce, and J.B. Benziger. *The importance of interstiticial gas expansion in infrared photoacoustic spectroscopy of powders*, J. Appl. Phys. **57**, 1710 (1985).
[144] Z.A. Yasa, W.B. Jackson, and N.M. Amer. *Photothermal spectroscopy of scattering media*, Appl. Opt. **21**, 21 (1982).
[145] C.B. Scruby and L.E. Drain. *Laser ultrasonics, techniques and applications*, chapter 5 (Adam Hilger, New York, 1990).
[146] J.J. Kelly and D. Vanmaekelbergh, in *the electrochemistry of nanomaterials*, chapter 4, edited by G. Hodes (Wiley-VCH, Weinheim, 2001).
[147] A. Borghesi, in Ref. [131], p. 445.
[148] P.C. Searson, J.M. Macaulay, and F.M. Ross. *Pore morphology and the mechanism of pore formation in n-type silicon*, J. Appl. Phys. **72**, 253 (1992).
[149] M. Christophersen, J. Carstensen, S. Rönnebeck, C. Jäger, W. Jäger, and H. Föll. *Crystal orientation dependence and anisotropic properties of macropore formation of p- and n-type silicon*, J. Electrochem. Soc. **148**, E267 (2001).
[150] M.I.J. Beale, J.D. Benjamin, M.J. Urem, N.G. Chew, and A.G. Cullis. *An experimental and theoretical study of the formation and microstructure of porous silicon*, J. Cryst. Growth **73**, 622 (1985).
[151] R. Herino, G. Bomchill, K. Barla, C. Bertrand, and J.J. Ginoux. *Porosity and pore size distribution of porous silicon layers*, J. Electrochem. Soc. **143**, 1994 (1987).
[152] X.G. Zhang. *Mechanism of pore formation on n-type silicon*, J. Electrochem. Soc. **138**, 3750 (1991).
[153] V. Lehmann. *The physics of macroporous silicon formation*, Thin Solid Films **255**, 1 (1995).
[154] T. Nakagawa, H. Koyama, and N. Koshida. *Control of structure and optical anisotropy in porous Si by magnetic-field assisted anodization*, Appl. Phys. Lett. **69**, 3206 (1996).
[155] D.H. Dau. *Propagation of light in disordered systems*, undergraduate thesis, University of Amsterdam (2000).
[156] D.S. Wiersma, M.P. van Albada, and A. Lagendijk. *An accurate technique to record the angular distribution of backscattered light*, Rev. Sci. Instrum. **66**, 5473 (1995).
[157] S.M. Sze. *Physics of semiconductor devices* (Wiley-interscience, New York, 1981).
[158] B.H. Erné. *High quantum yield III-V photoanodes*, PhD. thesis, University of Utrecht (1995).
[159] B.H. Erné, D. Vanmaekelbergh, and J.J. Kelly. *Morphology and strongly enhanced photoresponse of GaP electrodes made porous by anodic etching.*, J. Electrochem.

Soc. **143**, 305 (1996).

[160] B.H. Erné, D. Vanmaekelbergh, and J.J. Kelly. *Porous etching: a means to enhance the photoresponse of indirect semiconductors*, Adv. Mater. **7**, 739 (1995).

[161] I.M. Tiginyanu, C. Schwab, J.-J. Crob, B. Prévot, H.L. Hartnagel, A. Vogt, G. Irmer, and J.Monecke. *Ion implatation as a tool for controlling the morphology of porous gallium phosphide*, Appl. Phys. Lett. **71**, 3829 (1997).

[162] D. Vanmaekelbergh, M.A. Hamstra, and L. van Pieterson. *Free carrier generation in semiconductors induced by absorption of sub-band gap light. A photochemical study with nanoporous GaP*, J. Phys. Chem. B **102**, 7997 (1998).

[163] C.M. Soukoulis, S. Datta, and E.N. Economou. *Propagation of classical waves in random media*, Phys. Rev. B **49**, 3800 (1994).

[164] K. Busch and C.M. Soukoulis. *Transport properties of random media: An energy-density CPA approach*, Phys. Rev. B **54**, 893 (1996).

[165] Ref. [27], chapter 4.

Summary

This thesis constitutes an experimental study of the propagation of light in strongly-scattering media. In an intensive search for Anderson localization of light, samples of high refractive index semiconductors have been investigated.

In this thesis, a photonic material is defined as a medium that scatters light strongly. Two limiting cases of photonic materials can be discerned:

- *Periodic three-dimensional (3D) crystals*. A periodic 3D crystal is a lattice of dielectric particles with a lattice spacing of the order of the wavelength of light. If the refractive index contrast between the particles and the surrounding medium is high enough a photonic band gap may be created. The propagation of light in such a medium is similar to the propagation of electrons in a crystalline semiconductor.
- *Random materials*. Random materials are 3D systems of dielectric particles randomly placed and separated by a length of the order of the wavelength of light. Light propagates as electrons do in amorphous semiconductors. If the strength of the disorder or scattering is high enough, light can not propagate through the system and it is localized.

In disordered systems the transport of light is diffusive. The direction of propagation of light is randomized in an average distance given by the transport mean free path ℓ. The photonic strength of the system is defined by the inverse of the localization parameter $k\ell_{\rm s}$, where k is the wave vector in the medium and $\ell_{\rm s}$ is the scattering mean free path or the average distance between two scattering events. Only in the extreme case of very strong scattering, i.e., when $k\ell_{\rm s} \lesssim 1$, the transport is inhibited and Anderson localization of light is established. Anderson localization is a phase transition between propagating states and localized states, and it is the result of wave interference.

To approach the localization transition, $k\ell_{\rm s} \simeq 1$, the scattering mean free path needs to be reduced, which is achieved by using high refractive index (n) scatterers,

with a size of the order of the wavelength, in a low refractive index matrix, i.e., powders. An alternative to powders are scatterers of low refractive index material in a matrix of high refractive material, i.e., porous structures.

In the past, most of the research in disordered scattering materials was done with dielectrics as titanium dioxide ($n = 2.7$). Even stronger photonic materials can be achieved with some semiconductors, since they have a very high refractive index and present very low optical absorption at larger wavelengths than the semiconductor band gap wavelength. We have studied the propagation of near and midinfrared light through silicon, Si ($n = 3.5$), and germaniun, Ge ($n = 4$), powder samples, and of visible light through porous gallium phosphide, GaP ($n = 3.3$). Porous GaP is the strongest photonic material of visible light to date.

The powders (Si and Ge) were prepared by decreasing the particle size by milling intrinsic material, and reducing the polydispersity by letting the particles sediment in a fluid. The optical transport in these samples was investigated in the near infrared ($1.4\ \mu\text{m} < \lambda_o < 2.5\ \mu\text{m}$). Total-transmission measurements in the samples of Si powders allowed the determination of the transport mean free path, the absorption length and (assuming isotropic scattering) the localization parameter. The transport mean free path and the localization parameter are qualitatively well described by the energy density coherent potential approximation. A novel method to investigate the residual absorption has been developed: the measurement of the transmission through the samples filled with a non-absorbing liquid makes possible to distinguish between optical absorption and light localization.

The Ge samples were also studied in the midinfrared using a free electron laser, FEL (Free electron laser for infrared experiments, FELIX, Rijnhuizen, The Netherlands). Due to the high intensity of the FEL radiation and to its picosecond pulse structure new experiments could be performed. We have demonstrated that the comparison between the total transmission and the coherent transmission can be used to investigate the localization transition. From dynamic measurements, as time-resolved speckle interferometry, the light diffusion constant could be obtained. The diffusion constant is significantly reduced in samples thinner than $\simeq 7\ell$, probably due to the reduced dimensionality in these samples. The energy velocity is significantly lower than the phase velocity due to resonant multiple scattering. Photoacoustic spectroscopy proved to be a very sensitive method to measure the residual absorption in the Ge samples.

The main result of these investigations in powders is that the scattering strength in semiconductor samples is higher than in dielectric samples, due to the higher refractive index of these materials. The polydispersity in the particle size is the main limiting factor of the scattering strength in disordered scattering samples. Significant absorption is present in the powders, constituting a complication for the

localization experiments.

Gallium phosphide is transparent for light in the yellow and red part of the visible spectrum, being a fascinating material for localization experiments at wavelengths where Si and Ge present strong absorption. Strongly-scattering samples in the visible with virtually no absorption can be fabricated from n-type GaP by means of electrochemical etching. Electrochemical etching produces a random and homogeneous porous structure in GaP. We have studied the pore formation and the scattering strength as a function of the doping concentration and the etching potential. These two parameters determine the extension of the semiconductor depletion layer during etching, and influence the pore formation. Bigger and more widely-spaced pores can be formed in low-doped GaP. At low potential the pore diameter is reduced. Since the scattering strength in a porous material depends on the pore size and on the pore spacing, it is possible to tune it in a wide range. Enhanced- backscattering measurements were used to quantify the scattering strength of porous GaP. The strongest scattering sample of visible light reported to date is low-doped porous GaP. To further increase the scattering strength, the size of the pores was augmented by means of chemical etching. To optimize the scattering, the optical transmission was measured during the chemical etching. Contrary to what it is expected, for the strongest scattering sample the width of the enhanced-backscattering cone is reduced upon chemical etching. This is a surprising result that requires further investigation.

Samenvatting

De voortplanting van licht in een homogeen medium is eenvoudig. Licht plant zich voort in rechte banen. Als het licht een obstakel (of verstrooier) op zijn baan tegenkomt, wordt het verstrooid. Dat het licht verstrooid wordt, betekent dat zijn voortplantingsrichting is veranderd. Licht kan ook geabsorbeerd worden. Een object dat verstrooit maar niet absorbeert, is wit. Wordt al het licht geabsorbeerd, dan is het object zwart. Worden slechts bepaalde kleuren (of golflengtes) geabsorbeerd, dan heeft het object een kleur; een rode appel, bijvoorbeeld, absorbeert blauw en groen licht en verstrooit het rode licht. Het is belangrijk ons te realiseren dat wij de objecten om ons heen kunnen zien doordat zij licht verstrooien. Je zou kunnen zeggen dat wij kunnen zien dankzij verstrooiing van licht.

Hoe sterk een obstakel verstrooit, wordt bepaald door zijn afmeting en andere eigenschappen. De verstrooiing is het sterkst wanneer de afmeting van het obstakel ongeveer gelijk is aan de "afmeting" van het licht. Het licht is een golfverschijnsel zoals de kringen die ontstaan wanneer er een steen in het water gegooid wordt. Met de afmeting van het licht wordt de golflengte of de afstand tussen twee golftoppen van de kringen bedoeld. Het zichtbare licht, oftewel het licht dat de mens kan zien, heeft een golflengte tussen 0.4 en 0.7 maal het miljoenste deel van een meter (0.4-0.7 micron). Blauw licht heeft een golflengte van 0.4 micron, terwijl de golflengte van rood licht 0.7 micron is. De eigenschappen van de verstrooier die het verstrooien karakteriseren, worden beschreven door de brekingsindex. De brekingsindex karakteriseert hoe sterk de interactie tussen het licht en de verstrooier is. Hoe groter het brekingsindex verschil tussen de verstrooier en het medium is, des te sterker wordt het licht verstrooid.

Bevindt zich in een medium meer dan één verstrooier, dan vindt er meervoudige verstrooiing plaats. Zijn de verstrooiers willekeurig geplaatst, dan is het medium een wanordelijk systeem. Een wolk is een voorbeeld van meervoudige verstrooiing in een wanordelijk systeem. Door de meervoudige verstrooiing aan de waterdruppels van de wolk, is de zon niet meer te zien. Het licht van de zon dif-

fundeert in de wolk. Dit betekent dat de voortplanting van het licht niet langer volgens een recht pad verloopt. Andere voorbeelden van meervoudige verstrooiende media zijn melk, tandpasta, zand en verf.

In het geval van extreem sterke verstrooiing, kan licht gelokaliseerd worden. Lokalisatie wordt veroorzaakt door interferentie van verstrooid licht en betekent een hindering van zijn voortplanting. Door de wanorde bevindt het licht zich in een val in het medium. Philip W. Anderson voorspelde in 1958 lokalisatie in wanordelijk systemen in samenhang met electronisch transport. Door dit werk won Anderson de Nobel prijs voor Natuurkunde in 1977. Pas in de jaren tachtig realiseerden wetenschappers zich dat lokalisatie wordt veroorzaakt door interferentie van electrongolven. Aangezien interferentie een eigenschap is van alle soorten golven, voorspelde men dat ook licht gelokaliseerd kon worden. Daarna begon een intensief onderzoek naar systemen waarin licht gelokaliseerd zou kunnen worden. Nog steeds is er geen beslissend bewijs van Anderson lokalisatie van licht in drie dimensionale systemen.

Dit proefschrift beschrijft een experimenteel onderzoek naar de voortplanting van licht in sterk verstrooiende en wanordelijke systemen. In vergelijking met wolken, verstrooien onze monsters het licht ongeveer één miljoen keer sterker en zijn als zodanig de sterkst-verstrooiende systemen tot op heden. De motivatie van dit onderzoek was de studie van Anderson lokalisatie van licht. Om zo'n sterke vertrooiing te kunnen bereiken, hebben wij gebruik gemaakt van halfgeleiders zoals silicium (Si), germanium (Ge), een gallium fosfide (GaP). Deze materialen hebben een hoge brekingsindex en verstrooien daardoor het licht erg efficiënt.

Zoals eerder besproken, is de verstrooiing maximaal wanneer de verstrooier de afmeting van de golflengte van het licht heeft; daarom werden stukken Si en Ge verpoederd tot deeltjes van ongeveer één micron. Foto's van de poeders van Si en Ge zijn te zien op paginas 49 en 64. Met deze deeltjes zijn lagen van verschillende dikten gemaakt.

Absorptie van licht is de grooste complicatie bij de experimenten omdat men vermoedt dat het de lokalisatie vernietigt. Bovendien produceert absorptie hetzelfde resultaat als lokalisatie in het merendeel van de experimenten, wat het analyseren moeilijk maakt.

Silicium en germanium absorberen zichtbaar licht, maar laten infrarood licht door. Daarom zijn de experimenten uitgevoerd met infrarood licht. In hoofdstuk 3 worden de totale transmissie metingen beschreven. De totale transmissie is de fractie van de lichtintensiteit die wordt doorgelaten door het monster. Kan het licht zich niet voortplanten in het monster door lokalisatie, dan zal de totale transmissie erg laag zijn. Aan de andere kant als het licht geabsorbeerd wordt, is de totale transmissie ook laag. Met de experimenten beschreven op hoofdstuk 3, laten wij

zien dat de verstrooiing van infrarood licht in Si en Ge poeders zeer sterk is, maar dat absorptie wordt geïntroduceerd tijdens de preparatie van de deeltjes (de monsters waren "verontreinigd"). De resultaten van hoofdstuk 3 kunnen zonder de hulp van het concept van Anderson lokalisatie begrepen worden.

In hoofdstuk 4 zijn nieuwe experimenten met monsters van germanium poeders beschreven. Deze experimenten zijn uitgevoerd met een laser van infrarood licht (FELIX, Rijnhuizen). Naast de totale transmissie, hebben wij ook de totale reflectie gemeten, oftewel de fractie van het licht dat gereflecteerd wordt door het monster, en de coherente transmissie, oftewel de transmissie van alleen de richting van het opvallende licht. Door vergelijking van de resultaten van deze metingen kan het niveau van lokalisatie in de monsters kwantitatief bepaald. Met FELIX hebben wij ook dynamische-transmissie metingen oftewel metingen als functie van tijd, uitgevoerd. Met deze metingen kunnen wij de lichtdiffusieconstante en de voortplantingssnelheid bepalen. Wij hebben ook de absorptie van de Ge poeders met behulp van fotoakoestische spectroscopie bestudeerd. Geabsorbeerd licht genereert warmte. Deze warmte veroorzaakt een akoestische golf die beluisterd (of gemeten) kan worden.

De monsters van GaP werden gemaakt door middel van elecktrochemisch etsen. Tijdens het etsen wordt een stuk GaP in een zwavelzuurbad onder een elektrische spanning gehouden. Dit veroorzaakt het etsen van GaP op bepaalde plekken, en de vorming van poriën die op een wanordelijke manier groeien. Er wordt een poreuze structuur gevormd die het licht sterk verstrooit. Deze structuur wordt weergegeven door een spons zoals afgebeeld op de kaft. Een foto van poreus GaP is te zien op figuur 1.2 (b). Gallium fosfide is doorzichtig voor rood licht. Daarom zijn de metingen uitgevoerd met licht van deze kleur. De verstrooiing van licht in GaP monster werd bestudeerd door middel van het meten van de terugstrooikegel. De terugstrooikegel is het resultaat van interferentie van licht dat zich in een wanordelijk systeem voortplant. Zoals wij in hoofdstuk 5 laten zien, kan de mate waarin het licht verstrooid wordt, moeiteloos door de spanning tijdens het etsen en door de dotering van GaP ingesteld worden. In tegenstelling tot Si en Ge, genereert het etsen van GaP geen absorptie. Onze monsters van poreus GaP hebben tot op heden het wereldrecord van de sterkste licht verstrooiing. Lokalisatie van licht in porous GaP zal binnenkort een feit zijn...

Resumen

La propagación de la luz en medios homogéneos es simple: la luz viaja en trajectorias rectas. Al encontrar un obstáculo en su camino la luz es dispersada, cambiando así su dirección de propagación. La luz también puede ser absorbida por el obstáculo. Un objeto es blanco cuando no absorbe; por el contrario, si absorbe toda la luz es negro. Si sólo determinados colores (o longitudes de onda de la luz) son absorbidos, el obstáculo tiene color; por ejemplo, un manzana roja absorbe luz azul y verde, y dispersa luz roja. Es importante entender que podemos ver los objetos que nos rodean gracias a que dispersan la luz que reciben. Podríamos decir que no somos ciegos gracias a la dispersión de luz.

La intensidad con la que un obstáculo dispersa luz depende de su tamaño y propiedades físicas. La dispersión es más intensa cuando el tamaño del obstáculo es aproximadamente igual al "tamaño" de la luz. La luz es una onda como lo son las oscilaciones que se producen en el agua de un lago al arrojar una piedra. El tamaño de la luz es una referencia a su longitud de onda o a la distancia entre dos crestas consecutivas de la oscilación. La luz del visible, o la luz que el ojo humano puede ver, tiene una longitud de onda comprendida entre 0.4 y 0.7 veces la millonésima parte de un metro (0.4-0.7 micras). La luz azul tiene una longitud de onda de 0.4 micras, mientras que la longitud de onda de la luz roja es de 0.7 micras. Las propiedades físicas del objeto que producen la dispersión de la luz son descritas por el índice de refracción. Este índice representa la intensidad con la que el material interacciona con la luz, y por lo tanto la intensidad de la dispersión. Cuanto mayor es la diferencia entre el índice de refracción del obstáculo y el del medio que le rodea, mas intensa es la dispersión de luz.

Si en un medio hay mas de un objeto que dispersa luz, se produce dispersión múltiple. Si la posición de los objetos es aleatoria se dice que el medio es desordenado. Las nubes son ejemplos de medios desordenados. La dispersión múltiple de la luz del sol con las pequeñas gotas de agua que forman la nube impiden ver el sol. La luz es difundida por nube, o en otras palabras, su trayectoria no es rectilínea.

En el caso extremo de dispersión muy intensa, la luz puede estar localizada. La localización es el resultado de interferencia de la luz dispersada e implica una inhibición de su propagación. Debido al desorden producido por los obstáculos, la luz se encuentra atrapada en el medio. El concepto de localización inducida por desorden fue introducido por Philip W. Anderson en 1958 en el contexto de transporte electrónico, por lo que ha sido bautizada como localización de Anderson. Por este trabajo Anderson ganó el premio Nobel de Física en 1977. En los años 80, se asoció el fenómeno de localización con la interferencia producida por el caracter ondulatorio de los electrones. Interferencia es una característica de cualquier tipo de onda, por lo que se predijo que la luz podía ser localizada de la misma forma que los electrones. Empezó entonces un intensivo trabajo experimental para localizar luz. Aun hoy en día no existen pruebas concluyentes que demuestren localización de Anderson para la luz en sistemas tridimensionales.

Esta tesis describe un estudio experimental de la propagación de la luz en medios desordenados en los que se produce dispersión múltiple. Los sistemas que hemos estudiado dispersan la luz con una intensidad aproximadamente un millón de veces mayor que las nubes. La motivación de este trabajo ha sido la obtención y el estudio de localización de Anderson para la luz. Para conseguir esta intensa dispersión hemos usado semiconductores como silicio (Si), germanio (Ge) y fosfuro de galio (GaP). Estos materiales tienen un indice de refracción muy elevado y por lo tanto dispersan luz muy eficientemente.

La dispersión es máxima cuando el objeto tiene el tamaño de la luz; por lo tanto piezas de Si y Ge fueron molidas hasta crear partículas con unas dimesiones de aproximadamente una micra. Estas partículas están representadas por las piedras de la portada de esta tesis. Fotografías hechas con un microscopio electrónico figuran en las páginas 49 y 64.

La absorción de luz es la principal complicación en los experimentos, ya que se piensa que esta destruye la localización de Anderson. Además, absorción produce el mismo resultado que localización en la mayoría de los experimentos ópticos, lo cual complica enormente su análisis.

Silicio y germanio absorben intensamente la luz del visible. Sin embargo, estos materiales no absorben luz infrarroja (de mayor longitud de onda que la luz roja). Por lo tanto, los experimentos fueron realizados con este tipo de luz. En el capítulo 3 se describen medidas de transmisión total. La transmisión total representa la fracción de la intensidad de luz que es transmitida por el medio. Si debido a localización la luz no se puede propagar, la transmisión total es fuertemente reducida. Igualmente si la luz es absorbida la transmisión es muy pequeña. Con los experimentos descritos en el capítulo 3 demostramos que la dispersión de luz infrarroja en las muestras de Si and Ge es muy intensa. Sin embargo ab-

sorción es introducida durante la preparación de las partículas (las muestras son "ensuciadas") y los resultados pueden ser explicados sin invocar localización de Anderson.

En el capítulo 4 se describen nuevos experimentos con muestras de partículas de Ge. Estas medidas fueron realizadas con un laser de luz infrarroja (FELIX, Rijnhuizen, Países Bajos). Además de medir la transmisión total también obtuvimos la reflexión total, o la fracción de la intensidad de luz que es reflejada por la muestra y la transmisión coherente o la transmisión en la dirección en la que incide el laser en la muestra. De la comparación de estas medidas se deriva el grado de localización de la luz en la muestras. También realizamos medidas de transmisión dinámicas o en función del tiempo. De estas medidas se deduce la constante de diffusion de la luz y su velocidad de propagación en las muestras. Por último también estudiamos la absorción de luz mediante medidas fotoacústicas. Cuando la luz es absorbida genera calor, el cual produce una onda acústica que puede ser "escuchada" o medida.

Las muestras de GaP fueron preparadas por medio de corrosión electroquímica. Durante este proceso, se introduce una pieza de GaP en un baño de ácido sulfúrico y se aplica un potencial eléctrico. Esto produce la corrosión de GaP en ciertos lugares, generando poros que crecen de forma desordenada. Se forma una estructura porosa que dispersa la luz intensamente. Esta estructura esta representada por la esponja de la portada. En la figura 1.2 (b) puede observarse una fotografía de una muestra de GaP poroso realizada con un microscopio electrónico. Fosfuro de galio no absorbe la luz roja y por lo tanto las medidas fueron realizadas con luz de este color. La dispersión de luz en muestras de GaP fue estudiada mediante la medida de cono de retroflexión. El cono de retroflexión es el resultado de la interferencia de la luz propagando en un medio desordenado y proporciona importante información sobre el transporte de esta. Como demostramos en el capítulo 5, la intensidad con la que la luz es dispersada en GaP poroso puede ser facilmente regulada por el potential eléctrico usado durante el proceso de corrosión electroquímica y por la concentración de dopante (o impurezas) del material. Al contrario que con la fabricación de las partículas de Si y Ge, el proceso de corrosión no introduce absorpción. Además, las mejores muestras de GaP poroso que hemos preparado constituyen el material que más intensamente dispersa luz visible. Localización de luz será dentro de poco un hecho en fosfuro de galio poroso...

Dankwoord

Gelukkig maar dat het werk voor een promotie niet alleen door één persoon gedaan wordt. Veel mensen hebben, direct of indirect, een positieve invloed gehad op mijn werk van de afgelopen jaren. Ik wil deze mensen hartelijk bedanken.

Ten eerste wil ik mijn promotor Ad Lagendijk bedanken. Ad kon altijd tijd voor discussies in zijn drukke agenda vinden. Ad, ik heb veel door en van jou geleerd. Rudolf was altijd bereikbaar en had een antwoord klaar voor mijn vragen. Dank je voor de vele discussies en suggesties. Willem Zorro, dankzij jou en het fantastische voorstel "Propagation of light in photonic crystals" kwam ik in de groep. Ook bedankt voor alle goede gesprekken, leuke momenten, en voor jouw enthousiasme. En wie weet... mischien word ik ooit een echte fotonisch krystallen man. Gerard, dank je voor de infraroodadviezen, erg handig in een meestal "zichtbare" groep.

Zonder de hulp van Wim zou het erg moeilijk zijn te promoveren. Wim was altijd bereikbaar om alle technische problemen snel te oplossen. Wim, dank je ook voor de schaatslessen en je goede humor.

Willem (Rint), wij hebben veel goede dagen voor de wetenschap samen doorgebracht. Het was een echt plezier samen met jou te etsen. John en Daniel, jullie interesse was een waarlijke motivatie. Ik heb veel geleerd van jullie. Stephan, dank je voor de technische hulp met de potentiostaten en Xinghua thank you for the SEM photos.

Chris, working with you at FELIX helped me a lot. After having worked with you, I know that the most difficult measurements are possible in two "shifts". Bart, je enthousiasme, interesse en suggesties waren erg belangrijk, onze werkzaamheden waren erg productief, dank je. To the FELIX staff I am indebted for all the support during our measurements.

Dau, your measurements of the escape function are beautiful. Thank you for all the time that you dedicated to working with us. I hope that all what you learnt in the group is now useful for you.

Costas, thank you for all the discussions about localization and random lasers. Also thanks a lot to you and to Kurt for the EDCPA calculations of chapter 3.

Ik wil Ronald Popma van het Materiaalkunde Instituut van de Rijksuniversiteit Groningen bedanken voor de EDX metingen aan de toplaag van de germanium monsters; en ook Ron Heeren en Muriel Geldof voor FTIR reflectie metingen aan deze laag.

Wijnand Takkenberg, dank je dat je me bijna alle geheimen van de SEM geleerd hebt; en ik zeg bijna omdat ik nog niet zulke mooie foto's als jij kan maken.

Michiel Groenenveld, hartelijk bedankt voor alle goede glas adviezen en voor het polijsten van de substraten. Eddy en Bert dank jullie wel voor alle ampullen die jullie hebben afgepompt en dichtgesmolten en voor jullie hulp met cuvetten en alle soorten glaswerk.

De vele adviezen over de optische microscopen, het polijsten van wafers en de ovens heb ik te danken aan Ton Riemersma en Hugo Schlatter. Willem Moolhuijzen en Bert Moleman zijn een echte hulp geweest bij het opstellen van de de röntgenstralen-diffractie opstelling.

Zonder de werkplaats van de WZI zou het niet mogelijk zijn te kunnen promoveren. Daarom iedereen bedankt voor het fantastische werk. Ik wil speciaal bedanken: Flip de Leeuw, Joost Overtoom en Johan van de Ridder. Flip, je deed me zien: dank je voor de detectoren die je voor me hebt in elkaar hebt gezet, en voor alle elektronica-klusjes. Joost en Johan, dank jullie wel voor de geweldige rotatietafel die jullie voor ons hebben gemaakt. Dankzij jullie kunnen we de beste ontsnap-functies van de wereld meten.

Door de EU beurs, de UVA en FOM contracten wist ik nooit wat ik precies was, maar gelukkig was Mariet Bos daar om alles te regelen. Ik wil Ina Zwart, Ineke Baaij en Roos Visser bedanken voor de secretariële ondersteuning. Ook bedank ik Dick Jensen voor het zorgdragen van de financiën. Dat de computers werken was te danken aan de ondersteuning van Derk Bouhuijs en Marc Brugman. Met de hulp van Ronald Winter was het altijd eenvoudig boeken in de bibliotheek te vinden.

Tom Gregorkiewicz, dank je voor de discussies over halfgeleiders. Bartek, thank you for your milling enthusiasm.

Diederik Wiersma en Bart van Tiggelen, ik heb veel plezier gehad tijdens onze discussies in Amsterdam, Veldhoven, Les Houches en in Kreta.

Aan de Amsterdam etsgenoten: Boris, Tom en Patrick wil ik onder andere bedanken voor de ontzettend leuke discussies, ideeën en de leuke experimenten.

Aan alle jongens en meisjes van de groep spectroscopie van der verdichte materie (later de golvers in complexe media en nu de COPS), en de waterstofboys, dank jullie wel voor de fantastische sfeer. Ik heb veel van jullie genoten

de afgelopen jaren. Rik, dank je voor de leuke praatjes in de ouderokers hoek en voor jouw hulp aan het begin. Pedro, Mark, Makoto, Denis, Anouk, Pepijn, Allard, Michiel, Judith Wijnrozen, Frank de GaP voortrekker, Mischa, Dirk, Dennis, kleine Frank, Henry, Henk, Arnout, Yuri, Manu, Juan, Gijs wanordelijke partner, geweldige discussiant en de koning van Latex, Martijn, (electrontrans)Femius, en Lydia... ik ga de vrijmibo's missen.

Ik heb bij deze groep gesolliciteerd op advies van Jom Luiten. Jom, dank je voor het goede advies.

Ik heb mijn eerste Spaanse woorden in Amsterdam gesproken met Felix Ritort. Felix, gracias por los buenos ratos, las risas y por animarme a escribir mi primer artículo en Catalán.

La panda de impresentables españoles en Amsterdam también me ha sido de gran ayuda. Gracias por todos los momentos divertidos, tan necesarios para compensar el estrés.

Edith, dank je voor al deze jaren en voor jouw geduld. Mijn excuses voor de diners die je in je eentje had omdat ik iets moest afmaken... big kisses.

Wanda, Albert, Oma en Edgar dank je voor jullie goede zorgen van de afgelopen jaren. Dat is erg belangrijk voor me geweest.

También tengo que agradecer a mis padres (a los que he dedicado esta tesis), por el apoyo que me han ofrecido durante toda mi vida... os quiero.

Jaime